Microfluidic and Electrokinetic Manipulation of Single Cells

THÈSE N^O 7403 (2017)

PRÉSENTÉE LE 17 MARS 2017
À LA FACULTÉ DES SCIENCES ET TECHNIQUES DE L'INGÉNIEUR
CHAIRE SWISS-UP EN INGÉNIERIE - LABORATOIRE D'ÉLECTRONIQUE POUR LES SCIENCES DU VIVANT
PROGRAMME DOCTORAL EN BIOTECHNOLOGIE ET GÉNIE BIOLOGIQUE

ÉCOLE POLYTECHNIQUE FÉDÉRALE DE LAUSANNE

POUR L'OBTENTION DU GRADE DE DOCTEUR ÈS SCIENCES

PAR

Samuel KILCHENMANN

acceptée sur proposition du jury:

Prof. L. Forró, président du jury
Prof. C. Guiducci, directrice de thèse
Prof. M. Hughes, rapporteur
Dr C. Duschl, rapporteur
Prof. D. Psaltis, rapporteur

If you always do what you always did,
you will always get what you always got.
— Albert Einstein

To my family and friends…

Acknowledgements

It was a great pleasure to conduct my work here at EPFL and during my thesis I got to know many new collegues, that became good friends over the years.

First of all, I would like to express my gratitude to my thesis director Carlotta Guiducci, for accepting me in her laboratory and giving me such a great opportunity to lead my own research. It was a pleasure to be part of her laboratory and I'm very thankful for the chance she gave me and the trust she put in me and my work.

I also thank sincerely all the members of the Life Sciences Electronics group, namely: Anna Feretti, Enrico Accastelli, Giulia Cappi, Elena Bianchi, Fabio Spiga, Enrica Rollo, Marco Letizia, Pietro Maoddi, Miyuki Matsuda, and Kevin Keim. I got a lot of support from my collegues and learnt many of the essential techniques that were required to successfully complete this work. Furthermore, we spent many great moments together and had a lot of fun in and outside the laboratory.

A special thank goes to Yuksel Temiz, that was not only a great lab member and collegue, but he also supervised me in the beginning, when I arrived in the laboratory and he thought me a lot of microfabrication tips and tricks that I could profit from over the years.

Furthermore, I would like to thank the CMi, for all their support and help with microfabrication issues. Without them it would not have been possible to conduct all the work that was performed during this thesis. They helped me to understand many problems and find solutions to them. Especially I would like to thank Dr. Cyrille Hibert, that was always a great source of inspiration in times a process didn't work.

I would also like to express my gratitude to Dr. Sébastien Jiguet on one hand he was a great help to troubleshoot all my SU-8 processes, on the other hand, we spent so many hours climbing and talking about photography, hours that were essential to get new ideas to advance the project. Furthermore, it was thanks to him that we had a group of more than 10 people that regularly committed to climbing, with a good scientific exchange.

Furthermore, I would like to thank all the master and semester students, namely: Saurabh Khemka, Marco Spinsanti, Ketki Chawla, Andrea Sottini, Idrees Samim, Thimotée Bronner, Baptiste Giraud-Heraud, Jerome Wagner, Thimotée Bronner, Marta Comino, Myriam Lyardon,

laughter and joy. And I have a deep admiration for her work as a caregiver for handicapped people.

Finally, I would like to thank my beautiful girlfriend Ines Benmessaoud for all her help and support during this thesis. We met during our thesis and although it beeing two scholars that conduct a thesis in parallel is not always the easiest, it was always a great joy to go this way together and to conduct some of our research together.

Lausanne, 12th December 2016   S. K.

Abstract

Traditional cell assays report on the average results of a cell population. However, a wide range of new tools are being developed for a fundamental understanding of single cell's functionality. Nonetheless, the current tools are either limited in their throughput or the accuracy of the analysis. One such technology is electrorotation. Although it is known to be unique in its capability for single-cell characterization, it is commonly a slow technique with a processing time of about 30 minutes per cell. For this reason, this thesis focuses on the development of a 3D electrode based electrorotation setup for fast and automatic extraction of a single cell's spectrum. For this purpose, new fabrication processes for 3D electrodes were developed to achieve high-resolution patterning of 3D metal electrodes. The first process we developed was a subtractive one based on passivated silicon structures and the second process was an additive one based on SU-8 photolithography. The additive nature of the second process enables high patterning resolution of electrodes and connection layers, while providing high conductivity thanks to the use of standard metal films. The electrodes have been characterized by different electrical measurements to ensure a proper connection and side-wall exposure. Furthermore, we characterized and compared the sheet resistance of planar and vertical layers. A further microfabrication process was developed for integrating the electrodes into microfluidic channels. The process was designed to enable the use of high numerical aperture lenses; for that purpose, a PDMS-mediated bonding process was engineered to seal the channels with a thin glass coverslip. Moreover, the development of a process to realize microfluidic access holes on the back of the wafer reduces the footprint of the chips and facilitates access for the microscope optics. Finally, a pressure-driven system was used together with the chips to achieve high control of liquid injections and to enable fast and precise flow stop. The combination of such a system, together with the dielectrophoretic forces that can be applied by the 3D electrodes, allows accurate positioning of single cells inside the 3D electrode quadrupole. The particles can then be analyzed by electrorotation. For this purpose, a custom Labview interface was built to coordinate the full setup and to acquire a full electrorotation spectrum in less than 3 minutes.

Key words: Electrorotation, Dielectrophoresis, Electrokinetics, 3D electrodes, Lab-on-a-chip, μ-TAS, dielectric spectroscopy

Résumé

Les tests cellulaires classiques rendent compte en général de l'état d'une population de cellules. Récemment, un éventail d'outils a été développé pour comprendre la fonctionnalité des cellules isolées. Cependant, ceux-ci exposent à une limitation en terme de débit de données et de précision d'analyses. Parmi ces outils, on trouve l'électrorotation. Bien que cette dernière soit unique dans la caractérisation de cellules isolées, elle rejoint les autres outils par sa lente vitesse d'acquisition et de traitement de données, moyennant 30 minutes par cellule. La présente dissertation de thèse met au point le développement d'une installation d'électrorotation à base d'électrodes en 3D permettant une extraction rapide et automatique de spectre d'une cellule isolée. Avant d'atteindre un tel avancement, l'objectif premier a été de mettre en place un nouveau procédé de fabrication d'électrodes en 3D qui permette l'obtention d'un motif d'électrodes en métal en 3D et à haute-résolution. Ainsi, nous avons d'une part, développé un procédé soustractif basé sur la passivation de structures en silicone et, nous avons, d'autre part ; mis en place un procédé additif basé sur la photolithographie de résines SU-8. Grâce à la nature additive du second procédé, nous avons réussi à atteindre une grande résolution de motifs au niveau des électrodes et à obtenir une haute conductivité à l'aide de films métalliques standards. De plus, par différentes mesures électriques, nous avons caractérisé les électrodes fabriquées pour s'assurer de leur capacité à véhiculer une bonne connexion électrique et une bonne exposition verticale. De même, nous avons caractérisé et comparé la pellicule de résistance des couches planaires et verticales. Par ailleurs, un dispositif de microfabrication avancé a été conçu pour intégrer les électrodes aux canaux de microfluidique. Ce processus a été développé pour faciliter l'accès du produit final à la platine de microscope et surtout à l'utilisation de grands objectifs pour acquérir des images à grande résolution. Ceci a été accompli en concevant le sertissage des canaux avec une fine lamelle en verre à l'aide d'un mécanisme de reliure en PDMS. D'autre part, la réalisation d'ouvertures d'accès aux canaux de microfluidiques derrière les plaques en silicone a été conçue pour des puces de petite taille afin de permettre le positionnement de toute la plateforme sur la platine du microscope. Enfin, un système de microfluidique par application de pression a été utilisé dans le but de réguler l'injection de fluides et d'assurer avec précision l'arrêt de celui-ci. Un tel système combiné aux forces de diélectrophorèse offre la possibilité de positionner une cellule isolée avec grande précision à l'intérieur de quadripôle d'électrodes 3D. De sorte que les particules microscopiques soient analysées par électrorotation, une interface logicielle customisée a été mise en place en utilisant Labview. Cette dernière permet non seulement la coordination de toutes les parties de l'outil développé mais aussi l'acquisition de spectres à une vitesse de moins de 3 minutes par cellule.

Acknowledgements

Contents

Contents

List of Figures

List of Tables

"Do not go where the path may lead, go instead where there is no path and leave a trail."

—Ralph Waldo Emerson

Introduction

Some decades ago, the fabrication of devices at the microscale was expensive and only sparsely available. However, recent advances in microfabrication technology have favored the development of new and affordable technologies. The rapid growth of the microelectronic industry made microfabrication technologies available to other fields, such as sensor. At the same time, pioneers such as Andreas Manz saw the potential that such technology can offer for micro total analysis systems (μTAS)[1]. Although most of such devices were originally designed for chemical sensing methods, they soon became popular for biological and cellular applications. However, the real breakthrough in this field came with the development of soft-lithography [2], which enabled fast and inexpensive fabrication of microfluidic devices. One of the main advantages of such systems is that they offer the possibility to pattern μm-sized features comparable with single cells and thus enable new ways to investigate and understand cellular mechanisms and disease-related modifications. While we only start to understand the unique information that is provided by observing single cells, we only mention two indicative examples. First, each living organism results from one single cell that develops over a certain time to a full organism. Thus, one single cell contains all the information that is required to form a living being. Another example is cancer. In cancer, different cells accumulate mutations, until at one point the cells hit a certain threshold and become cancerous. While there are generally multiple cells that have mutations, the cancer itself mostly develops from a single cell that turns into a cancer cell. While there are many other examples to motivate work on single cells, these two give the sense of the relevance of such understanding.

The wide interest in single cell research and the rapid development of microfluidic devices lead to numerous developments of new devices and technologies. In general, the techniques for single cell characterization are classified into two groups: label-based and label-free. The advantage of using labels is that the platform can be developed for a wide range of applications and the labels provide specificity for the applications. However, the labels come at the price of potential toxicity, background noise, or even failure. Furthermore, additional sample preparation is needed for the labeling procedure, which increases assay complexity and cost. For this reason, label-free technologies are generally preferred over label-based ones. In what follows, we provide an overview of different techniques that are commonly used for single-cell analysis.

FACS and MACS

In fluorescence-activated cell sorting (FACS) a laser beam is targeted at a capillary where single cells pass and the scattered light is analyzed to detect passing events. Modern tools have the ability to work with different light spectra and can provide 12 or more dimensions (fluorophores), allowing to screen thousands of cells per second [3]. One of the main challenges with the fluorescent labels was to develop a tool that is fast enough to precisely analyze the passing events and to deflect the particles accordingly. For this reason, magnetic-activated cell sorting (MACS) was developed, in which antibodies are coupled with magnetic beads. The beads allow the sorting of the cells by magnetic interactions [4]. Nonetheless, the use of labels in both cases makes them expensive, as they not only require markers, but also many steps for sample preparation. Furthermore, in general, such instruments are quite bulky, expensive and require trained people to operate them. Finally, a critical drawback is that the cells might be damaged due to shear stress.

Impedance Flow Cytometry (IFC)

Modern IFCs are generally miniaturized versions of Coulter counters [5] that are applied towards cell counting. In the first versions of these counters, cells were flown through a restriction with a diameter comparable to that of the cells. At low frequencies the cell membrane acts as an insulator; therefore, the passage of the cells causes the current to drop, which makes it possible to monitor the passage of single cells. While these devices were based on DC measurements, they were mostly restricted to counting the cells and giving an indication on cell size [6]; since then, the principle has been transferred to RF analysis. Such measurements make it possible not only to measure the size, but also to perform dielectric spectroscopy, enabling the quantification of dielectric properties of the cell membrane and the cytoplasm. Such devices have been applied to detecting and distinguishing different types of erythrocytes [7, 8], algae populations [9] and other cell lines [10, 11, 12].

However, a comprehensive understanding of the system in combination with a good model is essential to extract cellular characteristics. Such models are generally composed of electrical elements to model the electrode interfaces, the suspending medium and the cellular compartments (Fig. 1.a1 and a2). This modeling procedure also shows that, in the lower frequency range, the dielectric spectrum is dominated by the double layer that forms on the electrode surface and screens the cellular response (Fig. 1.b1).

Another important issue to be considered is the electric field distribution created by the electrodes. Differential measurements can be performed to account for the field distribution and other variability in the system (Fig. 1.a and b); however, this approach has its limitations. For example, planar electrodes generate a curved electric field which makes the sensitivity to a cell's passage dependent on its height in the channel (Fig. 1.a). For this reason, electrodes with uniform field distribution are preferable, as their detection capability does not depend on the
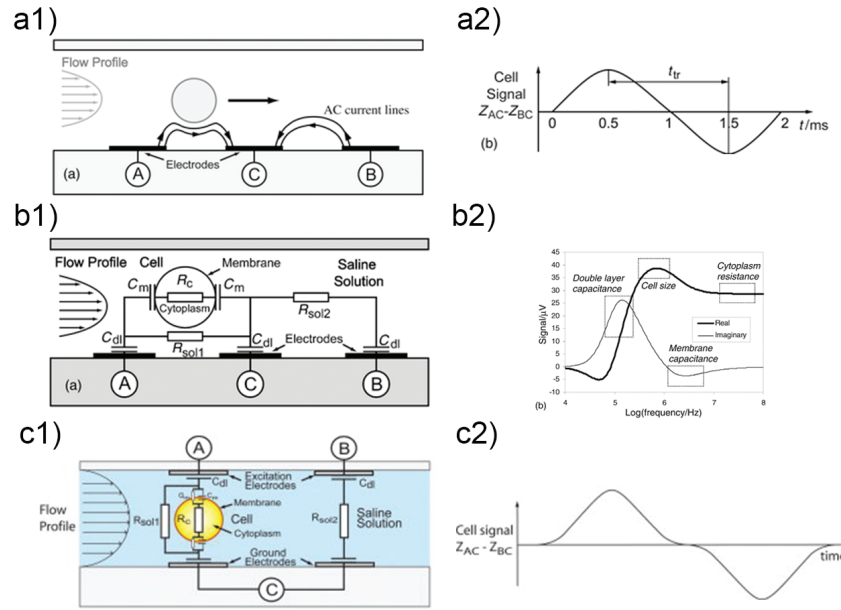
Figure 1 – Different IFC devices for cell characterization. (a1) Illustration of a single cell flowing through the microfluidic channels with bottom electrodes, illustrating the effect of a cell passing through the electric field distribution. (a2) Illustration of a differential measurement of a cell passing through the channel. (b1) modeling of the cell inside the microfluidic chamber with discrete electric elements. (b2) Simulation of a dielectric spectrum of a cell with a diameter of $10\,\mu m$. Reproduced from Ref. [14] with permission from The Royal Society of Chemistry. (c1) Illustration of an IFC device with top and bottom electrodes and the equivalent electric circuit used for modelling. (c2) Impedance signature of a cell passing through the device. Reproduced from Ref. [15] with permission from John Wiley and Sons.

cell position. One possibility to achieve a uniform electric field is to pattern the electrodes on the top and the bottom of the microfluidic channel, such that no fringing field effects will result (Fig. 1.c1 and c2). Another possibility are vertical electrodes, where the particles pass in between the electrodes [13].

Micro Electrical Impedance Spectroscopy (μ-EIS)

An impedance spectrum is the recording of the current response to an applied signal over a certain frequency range. This current depends on the different polarization interfaces and the modeling of such interfaces, which makes it possible to extract particle and cellular properties. Such devices have been demonstrated on a wide range of cell types, such as Hela [16, 17, 18] and other cancerous cell lines [19, 20] as well as many other cell lines, both human [21, 22, 23] and non-human [24, 25]. However, one of the problems with μ-EIS is that the measurement is sensitive to the cell position, which means that the cells have to be stably trapped making the design of this function particularly critical. Therefore, many different trapping principles have

3
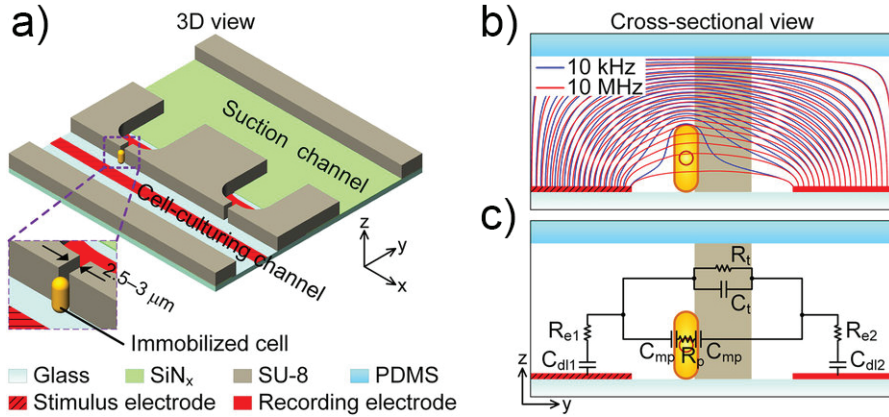
Figure 2 – An EIS device for single cell impedance spectroscopy. (a) illustration of the device with a cell trapped for analysis; (b) Electric field distribution for different frequencies; (c) The equivalent electric model of the device together with the trapped cell. Reproduced from [26] under CC BY4.0

been developed for μ-EIS, including the use of hydrodynamic traps [16, 17], negative pressure systems [22, 26], microholes [25], micropillars [16], and dielectrophoresis [18].

An advantage of using hydrodynamic traps or negative pressure systems is that the trapping structures can also be used to shape the electric field. In this case, even with planar electrodes, it is possible to achieve an electric field that has high linearity in the horizontal plane (Fig. 2.b). On the other hand, such traps can also be used to reduce the current passing around the cells, as the cells will be in close contact with the traps [27]. However, one of the drawbacks of such devices is that the traps can only be controlled on an all-or-nothing basis and it is hard to release single cells. One way to overcome this problem is through the use of DEP traps [18], which can be easily controlled by the application of an electrical signal. However, a major problem is ensuring that the DEP signals and the impedance signals do not interfere for instance, by alternating their application.

Although μ-EIS is a label-free, real-time and non-invasive technique, it is time consuming [19] and requires theoretical modeling for the data analysis [28]. One additional possible issue lies in the extraction of information in the lower frequency range that might be impaired by presence of the electrical double layer.

Patch clamp

Patch clamp measurements are commonly performed with sharp glass tips to target the cell membrane and record ionic currents flowing through it (Fig. 3.a1). Such measurements are unique in their resolution of the current recordings and enable even the recording of single ion-channels. In order to avoid current leakage, after positioning the pipette the membrane is sucked in to form a so-called giga-seal resistance [29]. Apart from the two major measuring
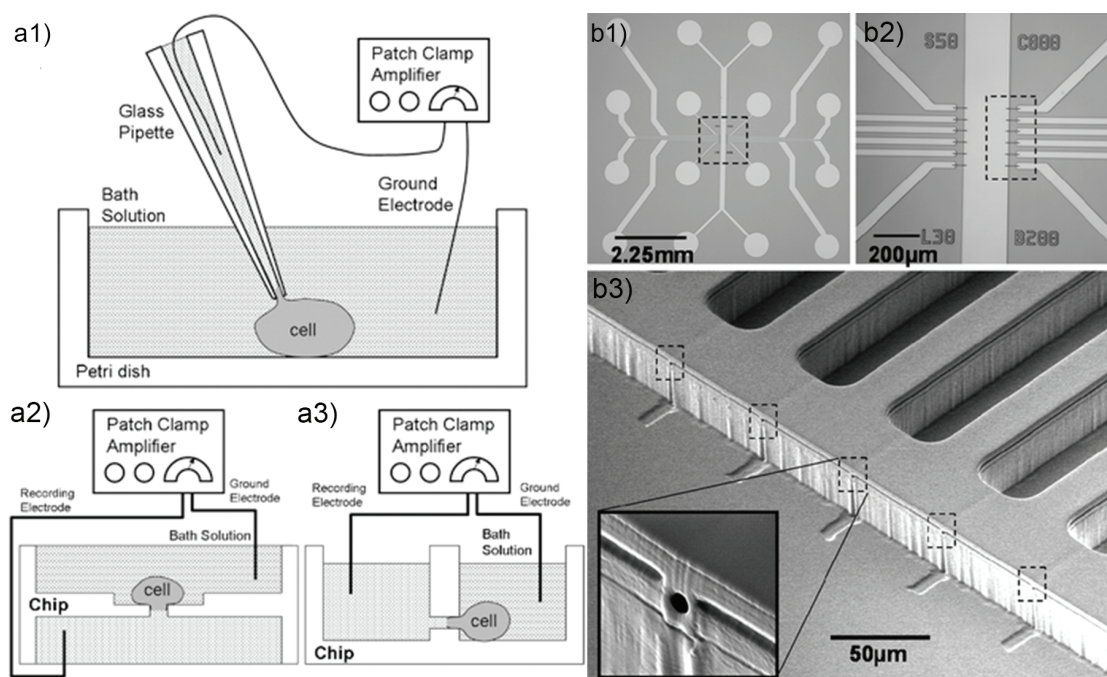
Figure 3 – Basic principle of different patch clamp setups (a1-a3) and a microfluidic patch clamp device (b1-b3). (a1) Schematic of a classic patch clamp setup, where the cell is measured through a glass capillary. Microfluidic based patch-clamp approaches, based on (a2) planar and (a3) lateral apertures. Reproduced from Ref. [34] with permission from The Royal Society of Chemistry. (b1) Picture of a full patch clamp device with microfluidic channels. (b2) Close-up of patch-clamp area. (b3) SEM image of the channel sidewall with the recording capillaries. Reproduced from Ref. [35] with permission from The Royal Society of Chemistry.

modes (current and voltage), there are five more configurations (cell-attached patch, whole-cell, inside out patch, outside-out patch and permeabilized patch [30, 31, 32, 33]) that enable a multitude of measurements.

However, there are several limitations to the conventional patch clamp technique. First, it is time-consuming [36, 37] and requires an experienced operator to move and place the pipettes. Initial attempts to solve this issue involved using robotic systems that were equipped with computer vision and capable of navigating micropipette electrodes [38]. However, such solutions did not bring the expected throughput as they were still based on the conventional approach. In the last decade, the field has profited from the rapid development in microfluidics and the fabrication of different devices that allow precise positioning of cells in a planar [39, 40, 41, 42, 43] (Fig. 3.a2) or vertical [34, 35, 44, 45] (Fig. 3.b3) aperture to perform the current recordings. In addition, such systems not only facilitate cell handling, but they also enable multiplexing to achieve dense arrays of measuring sites on a single chip (Fig. 3.b1-b3). The level of technological advancement in the last decade can be seen by the commercial products available from Sophion [46], Nanion [47, 41], Cytocentrics [48, 49], Molecular Devices (Ionworks [50, 51, 52, 53], PatchXpress [54, 55]) and Fluxion Biosciences [56]. However, it is

known that some products offer medium throughput but high-quality recordings, while others high throughput but only modest seals [57]. Furthermore, it is known that protein expression is not uniform over the cellular membrane and thus measurements of cell membrane patches are not representative [57]. Finally, in most scenarios, the cells are damaged, as the cell membrane is disrupted.

Electrokinetics

Electrokinetic technologies are based on placing cells in non-uniform electric fields and either moving (Dielectrophoresis - DEP) or rotating (Electrorotation - ROT) the cells by exerting an electrical force or torque on the induced dipole moment. The two phenomena are closely related and both depend on the polarization of the particles and the surrounding medium. The frequency dependent polarization can be modeled through the Clausius-Mossotti (CM) factor and the DEP force depends on the real and the ROT torque on the imaginary part. In theory, it is possible to extract the particle properties from both techniques; however, electrorotation is more suited for single-particle analysis, as the particles rotate at a fixed position with a constant strength in electric fields. Nevertheless, different techniques based on DEP make it possible to electrically characterize cells by curve fitting. However, as the spectra are generally assembled from measurements of a cell population, the found properties are the average parameters of a cell population than those of a single cell [58, 59, 60].

In electrorotation experiments, the cell rotation is induced by applying a rotating electric field. Such fields are commonly generated with electrode quadrupoles that are energized with signals in phase quadrature (Fig. 4.a). The rotation is observed and extracted for different frequencies and en electrorotation spectrum is constructed (Fig. 4.b). Finally, the found spectrum can be fitted with a theoretical model, in order to conclude on the electrical parameters of the observed cells [61, 62, 63]. The advantages of ROT are the possibility to extract a full dielectric spectrum of a single cell and the fact that it enables the extraction of inherent electrical properties of a cell with greater accuracy than any other technologies [64]. Nevertheless, the common drawbacks of the technique are its low throughput (about 30 min per cell) [65, 66] and the inability to achieve efficient rotation in high conductivity buffer [64]. While we will see in more details in the next chapter, the limited throughput mostly results from manual handling, as in many cases the cells are dropped on top of an electrode octopole and the rotation speeds are extracted by stop-watching. Furthermore, there are limited setups that allow for automatic cell handling.

Objectives and thesis outlook

From the above descriptions, it becomes clear that electrorotation is an interesting technology, however, it is not widely applied, due to the very low through put of such systems. For this reason, we decided to build a fully automated setup based on 3D electrodes that allows
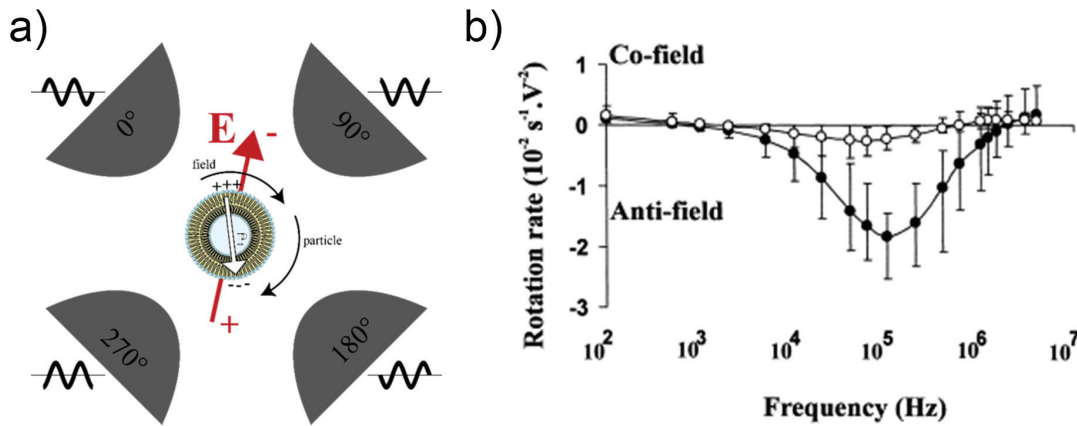
Figure 4 – The working principle of electrorotation and a sample rotation spectra illustrating the difference between alive and dead cells. (a) A ROT setup generally consists of an electrode quadrupole that is energized in phase quadrature to create a rotating electric field. The ac field polarizes the cells and generates a dipole, upon which it exerts a torque moment, resulting in the rotation of the particle. (b) A typical electrorotation spectra for viable (•) and non-viable oocytes (◦) of *Cyclospora cayetanensis*. Reproduced from Ref. [67] with permission from Elsevier.

for automatic sample handling through a combination of microfluidic and electrokinetic technologies. The development of this system will be discussed as follows:

Chapter 1 discusses the theoretical background and the current state of the art in electrorotation.

Chapter 2 focuses on the advantages and the fabrication of 3D electrodes and presents two new micro fabrication processes for such electrodes. The processes are unique in their characteristics and grant both high design flexibility and high conductivity.

Chapter 3 presents the integration of the 3D electrodes into microfluidic channels and a fabrication process for microfluidic channels compatible with high NA lenses. Moreover, we explain the ROT setup for automatic acquisition and detection of cell rotation spectra, followed by an explanation of a system for accurate cell positioning inside the microfluidic channels.

Chapter 4 Sums up the work that was done in the framework of this thesis and discusses further possibilities and improvements on the electrorotation setup. Furthermore, it introduces an additional microfabrication process to achieve high density 3D electrode arrays and it will give an overview of different possible applications for electrorotation.

"He who ask a question is a fool for 5 minutes. He who does not ask a question remains a fool for ever."

<div align="right">

—Chinese Proverb

</div>

1

Electrokinetic Theory

The response of particles to electrical fields has been studied for over 100 years (e.g. [68]). Initially, the focus was on particle motion or phoresis induced by DC electric fields. Approximately 50 years ago, scholars started to investigate the particles' response to AC fields and the influence of frequencies on the particles polarizability. In 1951 Pohl adapted the term dielectrophoresis from the term dielectric, which is used to describe materials of low conductivity and phoresis from the Greek term for motion. Dielectrophoresis (DEP) is commonly used to describe a particle's induced motion generated by inhomogeneous electrical fields, while electrorotation (ROT) and traveling wave dielectrophoresis (TW-DEP) are as based on rotating electrical fields [69]. In ROT, the rotating field is generated by an electrode quadrupole in order to exert a torque moment in the z-direction, while in case of TW-DEP the electrodes are aligned in a planar array to transport the particles either along or against the direction of the traveling electric field. The three different technologies are sometimes combined under the term generalized dielectrophoresis [70].

1.1 Suspended particles in electric fields

The suspension of biological particles in aqueous solutions leads to charge accumulations on their surfaces. Many biological particles consist of ionizable surface chemistry groups, such as $-COOH$ or $-NH_2$. Such examples are the ionizable head-groups of lipids that are incorporated in the cell plasma membrane. These head-groups result in slightly negative surface charges on the particle/medium interface and will attract free positive charges (ions) in the medium to neutralize the overall particle charge (Fig. 1.1.a). The surrounding counter-ion

atmosphere, together with the bound surface charges, is commonly referred to as the electrical double layer (EDL).

Upon application of a DC electric field, positive charges will be attracted by the anode and negative charges by the cathode, leading to particle motion that is commonly termed electrophoresis. In the case of bioparticles, electrophoretic motion is mainly caused by the induced surface charges, which is approximately 0.1% of the net surface charge [71]. In the case of human erythrocytes, a net migration speed of about $1\,\mu m s^{-1}$ can be achieved with an electrical signal of $1\,V cm^{-1}$.

This concept can be extended to AC electric fields and the different polarization effects that dominate at different frequency ranges. Up to few hundred Hz, the particle mobility is sufficient to follow the electric field and thus the particle's motion is dominated by electrophoretic forces. For higher frequencies, with field reversions faster than milliseconds, the inertia of the particle is too big and the particle is not able to follow the electric field, thus other effects dominate. Up to about 50 kHz, the dominant phenomena are the dynamic behaviors of the electrical double layer and the polarization around the cells. For higher frequencies, only interfacial polarizations are able to respond to such fast changes in field directions. At any frequency, the induced dipole moment is aligned with the electric field, with its direction depending on the polarizability of the particle and the surrounding medium. If the polarizability of the particle is greater than that of the medium, the dipole moment is parallel to the electrical field; if the particle's polarizability is smaller than that of the medium, the dipole is opposed to the electrical field (Fig. 1.1.c). However, as long as the particles are exposed to homogenous electrical fields, no particle motion is induced, due to the symmetry of the forces on each side of the particles. In order to induce DEP, inhomogeneous electric fields are required and particles that are less polarizable than the surrounding medium are directed away from the high field regions (negative DEP - nDEP) and, on the other hand, particles of higher polarizability than their surrounding medium are directed towards high field regions (positive DEP - pDEP) (Fig. 1.1.d).

1.1.1 Particles in rotating electrical fields (ROT, TW-DEP)

While stationary electric fields are used for DEP, there are two closely related technologies that work with moving electric fields, either rotating (in the case of ROT) or traveling (for TW-DEP). The above principle was formulated for the first time in 1978 by Pohl, when he stated that non-uniform (inhomogeneous) fields can sometimes induce a torque on a particle, causing it to spin. The first electrorotation devices were then described four years later [72, 73]. In ROT, a uniform rotating electrical field is generated by applying 90°-phase shifted sinusoidal voltages to four electrodes. The electric field exerts a torque moment on the induced dipole moment of the particle. Because this moment depends on the intrinsic properties of the particle, each particle has a unique response to each frequency and a complete rotation spectrum can serve as an electrical "fingerprint" of the particle. Furthermore, fitting the rotation spectrum with a
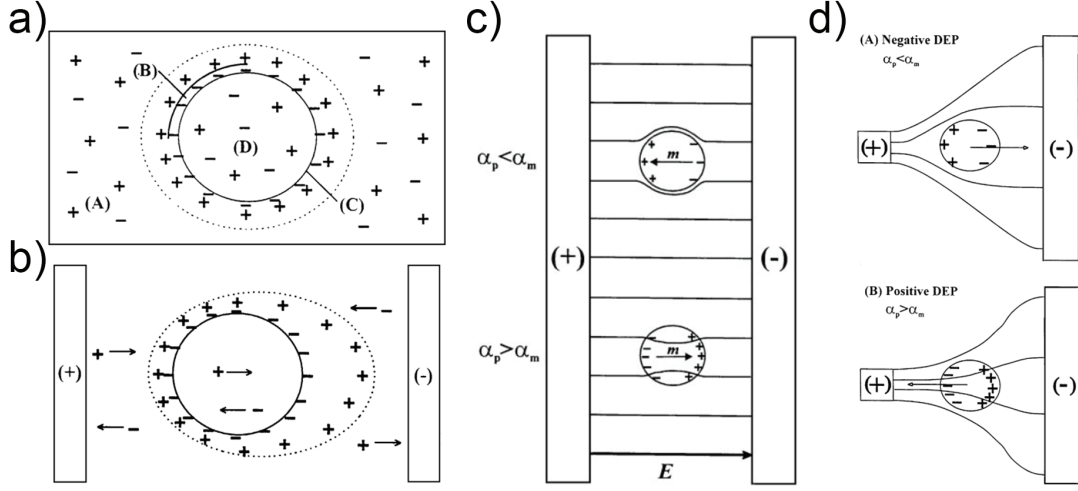
Figure 1.1 – Cell polarization in solution under the application of different types of fields. (a) A suspended cell in aqueous solution, with an electrical double layer (EDL) consisting of bound surface charges and free counter ions. (b) The application of a DC field attracts the ions to the electrodes, distorts the EDL and causes the cell to polarize. (c) Under application of a uniform electric field, the particles are polarized and the direction of the particle's dipole moment depends on the difference in cell and medium polarizability. (d) In an inhomogeneous electric field, the particles will experience a DEP force that pushes the particle either away from the high field regions (nDEP, A) or pulls them towards the high field regions (pDEP, B) Reproduced from Ref. [69] with permission from Cambridge University Press.

theoretical model enables different particle properties to be extracted [74]. At the same time, as the rotation rate depends on the induced dipoles, the medium polarizability plays a crucial role and, depending on the difference in polarizability of the medium and the particle, the latter can either rotate in the same direction (co-field) or against (anti-field) the direction of the electric field. The basic functioning principle of TW-DEP devices is very similar to that of ROT, with the sole difference that, with the former, the electrodes are placed in a linear array and the DEP force is used to move the particles over the electrode array. While the first TW-DEP devices used mainly low field frequencies (<100 Hz) to induce electrophoretic motion [75], later studies focused on higher frequencies to optimize the DEP forces. An advantage of TW-DEP is that it works in a stationary supporting fluid and without the need for fluid flow and therefore no dilution of the particles results [69].

1.1.2 Mathematical modeling of electrokinetic forces

The resulting electric force on a particle placed in an electric field can be calculated as:

$$\overline{F}_{elec} = q \cdot \overline{E} + (m \cdot \nabla)\,\overline{E} + \frac{1}{6}\nabla\left(\overrightarrow{Q} : \overline{E}\right) + \dots \tag{1.1}$$

11

The first term of this equation describes the Coulomb interaction of charges with the electric field; it vanishes for uncharged particles or for electric fields with a zero time-average. The second term depends on the particles dielectric polarization components induced by spatial inhomogeneities in the electric field and vanishes for spatial homogeneous fields ($\nabla E = 0$). All the remaining terms depend on induced multipoles, where the first term describes the induced dipoles [76]. In many cases, the higher order multipoles are neglected and thus the time averaged DEP force $\langle F(t) \rangle$ can be calculated by the dipole approximation as follows [77]:

$$\left\langle \overline{F}(t) \right\rangle = 2 \cdot \pi \cdot \varepsilon_m \cdot r^3 \left\{ \Re \left(f_{cm}(\omega) \right) \nabla E_{RMS}^2 \right.$$
$$\left. + \Im \left(f_{cm}(\omega) \right) \left(E_x^2 \nabla \varphi_x + E_y^2 \nabla \varphi_y + E_z^2 \nabla \varphi_z \right) \right\} \tag{1.2}$$

$$f_{cm}(\omega) = \frac{\varepsilon_p^*(\omega) - \varepsilon_m^*(\omega)}{\varepsilon_p^*(\omega) + 2 \cdot \varepsilon_m^*(\omega)} \tag{1.3}$$

$$\varepsilon^* = \varepsilon - j \frac{\sigma}{\omega} \tag{1.4}$$

where $f_{cm}(\omega)$ is the dipolar Clausius Mossotti factor, expressed in equation 1.3; r is the particle's radius; ω is the angular frequency; and E_{RMS} is the root mean square value of the applied electric field. E_i and $\phi_i (i = x, y, z)$ are the magnitudes and the phase of the electric field components in the principal axis directions. The complex permittivity (ε^*) of each material depends on its dielectric constant ε and electric conductivity σ and takes the form given by equation 1.4, where $j = \sqrt{-1}$ and the index m and p stand for the medium and the particle, respectively. Equation 1.2 indicates two independent force components: the first is due to field inhomogeneity depending on the real (in-phase or capacitive) component of the induced dipole moment and the gradient ∇E_{RMS}^2. Depending on the sign of $\Re \left(f_{cm}(\omega) \right)$, this force pushes the particle towards high or low electric field regions. The second term depends on the imaginary (out-of-phase or lossy) component of the induced dipole moment and the spatial non-uniformity $\nabla \phi_x, \nabla \phi_y, \nabla \phi_z$ of the field phase. This force either pushes the particle in the same or the opposite direction as the wave travels; depending on whether $\Im \left(f_{cm}(\omega) \right)$ is positive or negative. Furthermore, it can be seen that the Clausius Mossotti factor takes values between $1 \left(\varepsilon_p^*(\omega) \gg \varepsilon_m^*(\omega) \right)$ and $-0.5 \left(\varepsilon_p^*(\omega) \ll \varepsilon_m^*(\omega) \right)$. This shows the attraction of the particles toward high field regions (pDEP) for particles more polarizable than the medium, and retention of the particles towards low field regions (nDEP) for particles with polarizability lower than the medium. The above explanations show the importance of the suspending medium, as the strength of the DEP force will depend on the difference in polarization between the particle and the suspending medium. This is mostly important when DEP is used to separate two specific cell populations. A good choice of suspending medium enables to induce opposite DEP forces on each particle population and thus allows for particle sorting. Furthermore, as the DEP force depends on intrinsic particle properties, it is possible to sort the cells e.g. by size or cell membrane permittivity [78].

The above calculations can be further developed to find the frequency dependent rotation speed which can be calculated for a round shaped object by the following formula [62]:

$$\Omega(\omega) = -\chi \cdot \Im\left(\frac{\varepsilon_{eq}^* - \left(\varepsilon_0 \cdot \varepsilon_{r_m} + \frac{\sigma_m}{j \cdot \omega}\right)}{\varepsilon_{eq}^* + 2\left(\varepsilon_0 \cdot \varepsilon_{r_m} + \frac{\sigma_m}{j \cdot \omega}\right)}\right) = -\chi \cdot \Im\left(f_{cm}(\omega)\right) \tag{1.5}$$

Where the index m stands for the medium and χ is a coefficient depending on the electric field strength, the viscosity and the permittivity of the immersion medium. Finally, the complex particle permittivity ε_{eq}^* can be modeled through different existing cell models, as explained below. The above equation shows the impact of the Clausius-Mosotti factor for electrorotation experiments. This factor takes into account all the frequency-dependent effects. Knowing the Clausius-Mosotti factor, e.g. from ROT experiments, not only makes it possible to extract particle properties, but also to distinguish between two particles. When the particle properties are known for two particle populations, the two can be distinguished by applying a frequency where the particles rotate in opposite directions [79]. Furthermore, the knowledge gained from ROT experiments can be later used e.g. for DEP or TW-DEP experiments.

1.1.3 Cell models for DEP and ROT

One of the simplest cell models used for DEP and ROT experiments is the so called single-shell model. The particle is modeled as a homogenous sphere that is enclosed in a single layer of uniform thickness [80, 81, 82]. The particle is generally modeled with a particle radius of R_1 and a core radius of R_2 and the permittivities ϵ_2 and ϵ_3 for the permittivities of the outer shell and the inner core. The problem can be solved by assuming Laplace's equations for the electrostatic potential ϕ:

$$\Phi_1 = \left(-E_0 r + \frac{A}{r^2}\right)\cos\theta, r > R \tag{1.6}$$

$$\Phi_2 = \left(-Br + \frac{C}{r^2}\right)\cos\theta, R_1 > r > R_2 \tag{1.7}$$

$$\Phi_3 = -Dr\cos\theta, r < R_2 \tag{1.8}$$

With the boundary conditions:

$$\Phi_1 = \Phi_2 \text{ and } \varepsilon_1 \frac{\partial \Phi_1}{\partial r} = \varepsilon_2 \frac{\partial \Phi_2}{\partial r} \text{ at } r = R_1 \tag{1.9}$$

$$\Phi_2 = \Phi_3 \text{ and } \varepsilon_2 \frac{\partial \Phi_2}{\partial r} = \varepsilon_3 \frac{\partial \Phi_3}{\partial r} \text{ at } r = R_2 \tag{1.10}$$

By solving this equations, an effective homogenous dielectric permittivity value can be found:

$$\varepsilon_2' = \varepsilon_2 \left\{ \frac{a^3 + 2\left(\frac{\varepsilon_3 - \varepsilon_2}{\varepsilon_3 + 2\varepsilon_2}\right)}{a^3 - \left(\frac{\varepsilon_3 - \varepsilon_2}{\varepsilon_3 + 2\varepsilon_2}\right)} \right. \tag{1.11}$$

with $a = R_1/R_2$. In general in biology, the latter parameter can be approximated by 1, as cells have a very thin membrane in the order of few nm that can be neglected when compared to the total cell radius, which is in the the range of few μm.

While the single shell model is probably the most used model for DEP and ROT experiments, also more complex models exist. First, it is possible to build multi-shell models through the iteration of the above strategy. In this case, each iteration of the procedure adds up an additional layer or shell [74]. However, one downside of these models is that they assume a uniform sphere, while biological membranes often have surface features, such as microvilli, folds, ruffles and blebs. For this reason, a membrane folding factor was introduced, in order to take such membrane features into account [83]. Finally, biological samples are not always round-shaped and for this reason an ellipsoidal particle model was developed, for example for bacteria that have an elongated shape [84].

1.1.4 Optimization of the DEP/ROT medium

The optimization of the DEP medium is probably one of the most critical steps for electrokinetic experiments. We already saw in Equation 1.3 and 1.4 the dependence of the Clausius-Mosotti factor and the complex permittivity on the medium properties. It can be seen that at low and medium frequencies the dielectric response is predominated by conductivity, while permittivity will dominate at high frequencies. For non-dispersive media, in which both the conductivity and permittivity of the medium do not depend on the frequency, the frequency (f_0) at which the medium will change from conductivity to permittivity dominance can be calculated using the following formula [85]:

$$\sigma_m = 2\pi f_0 \epsilon_m \epsilon_0 \tag{1.12}$$
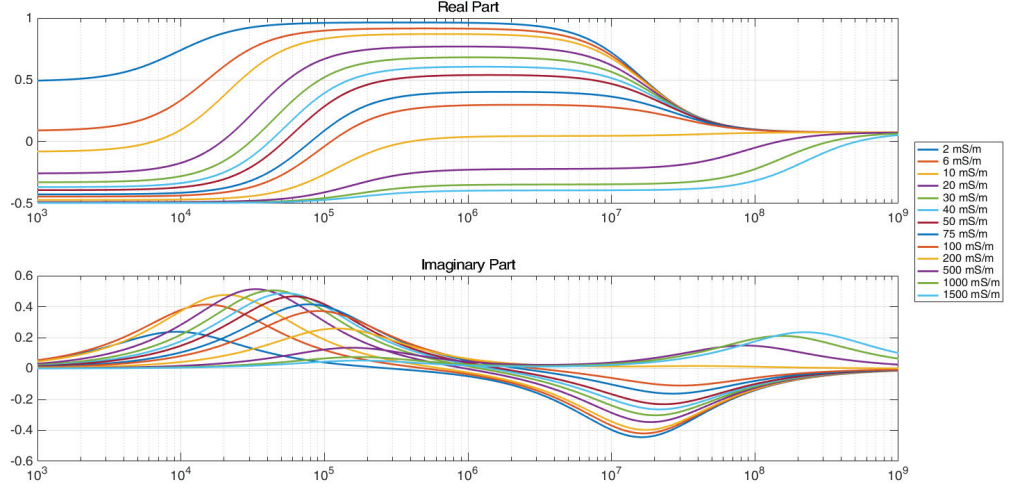
Figure 1.2 – Simulation results of the real and imaginary part of the Clausius-Mossotti factor for different medium conductivity.

For this reason, in the frequency range below f_0 the particles will experience pDEP in low-conductivity media and nDEP for high-conductivity media. At the same time, the medium conductivity also affects the imaginary part and causes a shift in location and strength of the rotation peak (Fig. 1.2). However, one of the problems with high-conductivity media is that it not only affects the polarization effect, but also increases the current density and the higher current leads to more Joule heating. This ultimately leads to more electrothermal effects and increases the risk of cell damage, as the voltage drop across the cell membrane is directly proportional to the medium conductivity. Typical cells have a membrane breakdown voltage in the range of 0.4 and 1 V [86] and the voltage drop can be calculated by:

$$V_m = \frac{1.5Er\cos\alpha}{\sqrt{1+\left(2\pi f\tau\right)^2}} \tag{1.13}$$

Where E is the electric field strength, r the particle radius and f the frequency of the electric field. α is the angle between the field lines and the normal from the particle center. Finally, τ is the cell membrane's time constant, which is given by [86]:

$$\tau = rC_{mem}\left(\frac{1}{\sigma_{cyto}} + \frac{1}{2\sigma_{media}}\right) \tag{1.14}$$

With C_{mem} the membrane capacitance, σ_{cyto} and σ_{media} the conductivity of the cytoplasma and the media, respectively.

15

Another parameter to consider is the medium permittivity, which not only affects the shape of the Clausius-Mossotti factor, but also the amplitude of the DEP force and the ROT torque (eq. 1.2). For this reason, high values of permittivity are interesting for electrokinetic media [87]. We will shortly discuss how these different parameters can be controlled and adjusted. However, let's first consider other properties that a DEP buffer has to fulfill.

In general, we already saw that it should have a low conductivity and a high permittivity. In addition, it needs to be iso-osmotic, non-toxic, should have a low viscosity, and the different components of the medium should not be able to cross the cell membrane, to avoid cell contamination. In addition, for longer experiments, the addition of cell nutrients should be considered. Finally, also the pH of the solution should be considered, which can be adjusted and stabilized through different buffers. There is a wide range of buffers that are known and generally used in cell biology. Among them, 20 that were introduced in 1966 by Norman E. Good [88] and are known as Good's buffers. These buffers make it possible to adjust and stabilize the pH of the medium. These buffers can serve as a basis for the DEP medium and the properties of these buffers can be adjusted. There are four different classes of materials that can be considered as additives for the buffer [87]:

- neutral molecules of large dipole moment

- small zwitterions (dipolar ions), such as amino acids

- larger zwitterions, such as polypeptides and proteins

- suspension of charged particles

The first category is generally not compatible with biological samples; the fourth one increases the medium conductivity and should therefore be added with care. For this reason, Arnold [87] tested a list of different materials of group 2 and 3. He showed that both small zwitterions and amino acids, as well as peptide solutions, can be used to increase the medium's permittivity, without affecting the conductivity. However, concentrations should be kept low; otherwise, at high concentrations the medium viscosity will also increase and, at solutions close to saturation, dielectric dispersion of the medium can occur. Finally, Arnold demonstrated the separation of dead and alive particles in a buffer of $1 M \epsilon$-amino-caproic acid (EACA), 2.5 mM HEPES and a total conductivity of $190 \, \mu S/cm$ that was not possible with a comparable buffer that had a smaller permittivity.

Finally, one of the most important parameters to consider is the osmotic strength of the solution, which should be in the same range as that of the cells. The osmotic pressure can be calculated as:

$$\Pi = iMRT \tag{1.15}$$

With Π the osmotic pressure, M the Molar concentration of the solution, R the ideal gas constant and T the absolute temperature. Finally, i is the van't Hoff coefficient, a measure of how the solute behaves in water and whether it breaks apart or not. For example, table salt (NaCl) has a Van't Hoff coefficient of 2, as it dissociates into two pieces, while sucrose has a Van't Hoff coefficient of 1, as the molecule remains one part. The osmolarity should be compatible with the cells as, otherwise, the osmotic pressure might either cause the cells to shrink and dry out (too high osmotic pressure) or swell and burst (too low osmotic pressure). In general, the osmotic pressure of mammalian cells is in the range of 260 and 300 $mOsm/kg$ [89], while some species, such as bacteria, can survive a wider range of osmotic pressures. As electrokinetic experiments are commonly performed at low conductivities, the osmotic strength must be adjusted; for example, by the addition of sugars, such as sucrose or dextrose. The latter also makes it possible to adjust the density of the solution, as a mole of sucrose and dextrose causes the same increase in osmotic pressure; however, because dextrose has twice the mass of sucrose, it causes a bigger increase in medium density than sucrose.

In the framework of this project, we used different buffer solutions, depending on the samples. In general, the buffers that were used were based on an isosmotic sucrose solution (8.5% sucrose, 0.3% dextrose) and the conductivity was adjusted by titration of PBS, while monitoring the conductivity with a conductivity meter. The medium conductivities were chosen by simulation of the DEP and ROT spectra in Matlab (Release 2012b, The Mathworks, Inc., Natick, Massachusetts, United States). The optimal medium conductivity was chosen to allow for efficient particle deflection at low frequencies by nDEP and to result in a well-defined rotation peak (Fig. 1.2).

1.1.5 Viability of cells after exposure electric fields

One of the major concerns for electrokinetic experiments is that the applied electrical fields and the medium employed might affect or alter the cells. We have already discussed cell membrane breakdown as a function of medium conductivity and the electric field strength. While cell membrane breakdown by electric fields can be used for poration, lysis, and fusion of cells [86, 90, 91], such effects require field strengths that are generally at least one order of magnitude higher than those used for electrokinetic experiments [69]. In addition, electroporation is a standard method used for gene transfection, where the cells are cultured normally upon exposure to the electric field. However, several studies have investigated cell toxicity caused by the exposure of cells to electrical fields that are commonly used for DEP and ROT. The first evidence of cell survival was given by trypan blue staining assays with dielectrophoretically separated erythrocytes [92] and successful culturing of yeast cells [93] and CD34+ [94] after DEP exposure. In general, there is not much evidence that cells might get damaged, nor from the field, nor from the buffers, as long as the field strengths are not too high. There is some evidence that pDEP might be more harmful to the cells, as the cells are directly attracted to the high electric field [95]. In addition, some studies showed that cells take more damage around the DEP cross-over frequency [96]. However, also in such cases,

the effect was statistical significant, but still affected only a low number of cells. Finally, the effect of DEP medium and electric fields was studied on neural stem progenitor cells, with an additional focus on possible affects on downstream differentiation. While some effects indicated cell toxicity around the DEP crossover frequency [96], no effect on the differentiation behavior was observed [97, 96, 98, 99]. A summary of these studies can be found in table 1.1. Although more evidence would be needed for a complete picture, however, these studies suggest, in order to minimize cell damage, cell membrane load should be reduced, for example by applying frequencies above megahertz or field strengths below few 10's kV/m [100].

Table 1.1 – Influence of the electric field used for DEP on the cells.

Cell line	Medium	Time	Field strength	Freq.	DEP	Parameters	Effect?	Ref
L929, 3T3	Saline	short, 3 days	30-60 kV/m	10-40 MHz	nDEP	viability, anchorage time, motility, growth and lag times	No	[101]
CHO, HFN 7.1	DMEM[1]	-	100 kV/m	10 MHz	nDEP	growth, glucose uptake, lactate levels, monoclonal antibody production	No	[102]
L929	RPMI	3 days	40 kV/m	100 kHz - 15 MHz	nDEP	cell division temperature	No[2]	[101, 103]
DS19	low conductivity	40 min.	100 kV/m	1 kHz - 100 MHz	nDEP	survival	No[3]	[104]

Continued on next page

18

Table 1.1 – continued from previous page

Cell line	Medium	Time	Field strength	Freq.	DEP	Parameters	Effect?	Ref
BHK 21 C13	10 mS/m isoos-motic	15 min.[4]	100 kV/m	5 MHz	pDEP	cell morphology, cell doubling time, oxydative respiration, gene expression and protein regulation	Yes [5]	[95]
NSPC[6]	DEP buffer[7] $150\,\mu S/cm$	10 min.[8]	$8\,V_{p-p}$ $100\,\mu m$ gap	25 kHz and 10 MHz	pDEP	viability	No	[97]
human and mouse NSPC[6]	DEP buffer[7] $110\,\mu S/cm$ (RPMI)	10 s - 30 min.	$8\,V_{p-p}$	10 kHz-10 MHz	pDEP and nDEP	trypan blue, LDH release, MTT	Yes [9]	[96]
human and mouse NSPC[6]	DEP buffer[7] $100\,\mu S/cm$ (KCl)	short time[10]	$10\,V_{p-p}$ $75\,\mu m$ gap	1 kHz-10 MHz	pDEP + nDEP	survival, proliferation, differentiation	No	[98]
mouse NSPC[6]	DEP buffer[7] $110\,\mu S/cm$ (RPMI)	5 min.	$7\,V_{p-p}$ $50\,\mu m$ gap	100 and 1000 kHz	pDEP	Trypan blue, cell differentiation	No	[99]
k562	various[11]	10 min.	$6\,V_{p-p}$	100 kHz	nDEP	Trypan blue	No	[105]

[1] Serum-free for CHO cells

[2] The cells resist higher field strengths at higher frequencies

[3] Below 10 kHz cells are affected due to peroxide production

[4] 15 min. exposure and 30 min. time delay

[5] It is not clear if the effects are of thermal or electric nature

[6] Neural Stem Progenitor Cells

[7] 8.5% sucrose, 0.3% glucose

[8] Buffer compatibility for up to 6 hours

[9] Damage was observed only at frequencies of 50 and 100 kHz and mostly for long exposure times

[10] Some hours for compatibility in buffer only

[11] 3 different buffers: 1) 1.5 M ϵ-aminocaproic acid, 2.5 mM HEPES, 2) 1.5 M ϵ-aminocaproic acid, 0.66 M saccharose, 3) 280 mM mannitol

1.2 Experimental setup for ROT experiments

A typical ROT setup consists of three main components: (1) a signal generator that is able to generate four signals with precise phase shifts, (2) a chip with the ROT electrodes that also contains either a microfluidic chamber or channels, and (3) an optical system for observation and acquisition of the particle rotation. The first ROT experiments were performed in square chambers that had four platinum as electrodes as sidewalls and that were energised by custom signal generators [72]. Since then, a lot of work has been devoted improve different parts of the setup for more precise and automated acquisition.

1.2.1 Generation of the electric field

The first ROT systems made use of conventional transistors to create the signals with accurate phase shifts at output voltages of up to 250 V. Such high voltages were needed to achieve sufficient field strength with the millimeter-sized electrodes. However, advances in microfabrication technologies made it possible to shrink the electrodes to sizes where small signal amplitudes (up to 10 V) are sufficient to generate the required field strength. While for DEP conventional signal generators can be used, ROT and TW-DEP require more elaborate instruments to generate four signals with precise phase shifts. Such signals can either be generated by custom quadrature oscillators [106] or commercially available arbitrary waveform generators, such as TTi TGA 12104, Fluke 280 and 290, TE WW 2074 or Hioki 7075.

1.2.2 Electrorotation chips

The development of microfabrication technologies not only made it possible to miniaturize the electrodes, but also to pattern the electrodes with higher precision. These advancements led to the analysis and creation of new electrode designs for ROT. For this purpose, the influence of electrode size, shape, and design were studied and analyzed. First, simulations were performed by modeling the rotation chamber as a resistor grid to confirm that the electric field strength increases with the electrode's curvature [107]. Later studies focused on other designs, such as rectangular, round, and pyramidal electrodes, and concluded that round-tipped electrodes resulted in the highest linearity of the electric fields [108, 109]. Furthermore, in order to reduce unwanted DEP forces, while providing a near uniform electric field in the central region, a special design of bone shaped electrodes was proposed [110, 67, 111].

While commonly electric fields in phase quadrature are used for ROT, in theory any number of $n > 3$ electrodes can be used for ROT, as long as they are energized with signals with a $360°/n$ phase shift. For this reason, in a study two planar designs of either four or eight electrodes were compared and although trapping and rotation was observed in both cases, the eight electrode design did not result in better performances. At the same time, the eight electrode chips do require a more careful chip design to prevent interferences of the electrical signals, and do require the generation of eight signals with precise phase shift instead of only four

[112].

Another problem is that the electric field decays quickly with distance from the electrodes and thus the rotation torque exerted on a particle or a cell depends on the particles height. For this reason, solutions are needed that enable more control on the electric fields in the 3D space. One such solution are octopole electrodes that consist of two stacked quadrupoles [113]. This solution is advantageous because the signals can be applied from the top and the bottom of the electrode chamber and can therefore achieve better performances for particle trapping. In addition, it is possible to simultaneously induce DEP trapping and ROT with the creation of a phase lag between the top and the bottom electrodes. This lag can either be created by patterning the top and bottom electrodes rotated with the lag angle [114] or by generating additional signals with the phase shift and applying eight different signals to the eight electrodes [115]. However, maximal trapping is achieved with a 180°-phase shift between the top and bottom electrodes; however, no rotation torque results in this case, while maximal ROT torque results from a 0°-phase shift, where no trapping forces result. Therefore, a compromise between trapping and rotation needs to be found [114, 115].

Although such co-planar systems make it possible to achieve higher field strengths and better particle trapping performances they are limited to small channel heights. On the other hand, 3D microelectrodes that span the full microfluidic channels grant higher control over the electric field distribution in microfluidic chambers, especially for bigger channel heights. However, as we will see in a later part, the fabrication of such electrodes is limited and thus only few examples of electroplated 3D electrodes can be found in literature[116, 117]. Nonetheless, in both papers the electrode designs are limited to small heights and wide electrode spacing. Although such electrodes grant higher control over the electric field distribution at the border of the rotation chamber, for large electrode spacing planar electrodes achieve similar electrical fields in the center of the ROT chamber. Once the electric field has expanded over the height of the microfluidic chamber, the generated fields are comparable and in general, the distance of the field expansion can be estimated to be similar to the channel height [118].

Table 1.2 summarizes the various electrode designs that have been applied for ROT experiments.

1.2.3 Particle Trapping

A general problem in ROT experiments is the resulting DEP forces that can destabilize the particles during the measurements. Although nDEP forces have a stabilizing effect and center the particles in the electrode chamber, pDEP forces disrupt the measurements and lead to attraction of the particles towards the electrodes. Therefore, the rotation speed can be affected by high levels of friction [134]. For this reason, different electrode designs, such as the Bone-shaped one [110], were developed to minimize the DEP forces. Furthermore, we have already seen the potential for using co-planar quadrupoles for simultaneous particle rotation and trapping. Nonetheless, trapping and rotation have to be compromised and the frequency for

Table 1.2 – Different electrode configurations that were used for ROT experiments

Design	#	Spacing	Material	Voltage	Ref
Plates	4	3 mm	Pt		[72]
	4	580 μm	Au	11 kV/m and 22 kV/m	[116]
Wires	4		Stainless steel	4 V_{p-p}	[119]
Needle electrodes	4	500 μm		8 kV/m	[120]
45°/90° Angle	8/4	100 μm	Cr/Au	50 V_{p-p}	[112]
90° angle	4	3 mm wide, 0.5 mm thick	Stainless steel		[121]
Polynomial	4	400 μm	Au	3 V_{rms}	[122, 123]
U-Wires	4	520 μm	Pt		[124]
Spiral electrodes[1]	4	140 μm	Cr/Au	2 V_{rms}	[79]
Polynomial	4	40 μm	Cr/Au	1 V_{rms}	[65]
Needle electrodes	4	1 mm	Pt	5-15 V	[125]
	4	800 μm	Au/Pd/Ti	2 V_{rms}	[95]
Rectangular	12 (3x4)	20, 40, and 80 μm	Ti/Pt		[126]
	4	100 μm, 1 mm	-/Pt needles	5-40 kV/m	[127]
Circular 60 μm	4	100 μm	Ta/Pt	$1 - 4.8\,V_{p-p}$	[128]
4 mm stainless steel electrodes	4	5 mm	Au	700 V/m	[129]
Circular 40 μm diameter	4	200 μm	Ta/Pt	$2.5 - 4.8\,V_{p-p}$	[130]
Bone	4	2 mm	Cr/Au		[110, 67, 131, 111]
Edges defined by a hyperbolic function in the center and parallel edges	4	400 μm	Cr/Au		[132]
Interdigitated[2]	4	20 μm	ITO	10-20 V	[133]
Co-planar quadrupole	8	40 μm	Au		[114, 115]
3D	4	300 μm	Au	1 V_{rms}	[117]

[1] For simultaneous TW-DEP ROT experiments
[2] Interdigitated electrodes at top and bottom

the trapping is the same as that for the rotation. For this reason, laser tweezers were proposed to trap the particles during the extraction of the ROT spectrum [135, 115, 136]. The advantage of such a system is that the trapping does not depend on the electrical fields and the tweezers enable additional possibilities, such as DEP force measurements [126, 137]. However, they come at a high cost, increase the setup complexity, and lead to higher risk of cell damage [135].
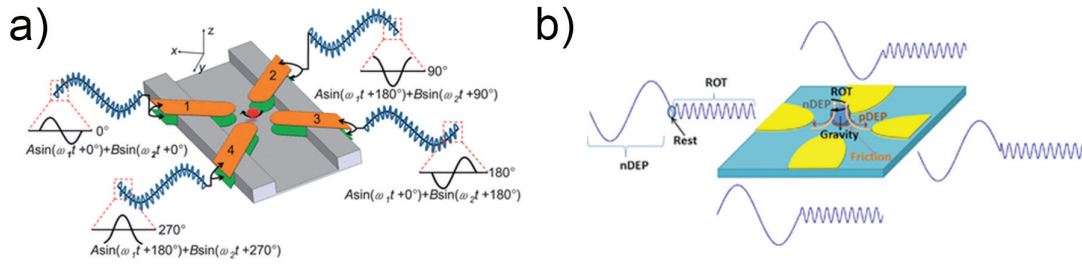
Figure 1.3 – Electrorotation setups for simultaneous cell trapping and rotation. (a) The cells are trapped in an electrode octopole by nDEP and the ROT signal is modulated on top of the DEP signal. Reproduced from Ref. [138] with permission from The Royal Society of Chemistry (b) The electrical tweezers approach for simultaneous DEP trapping and ROT experiments through spatial separation of the electrical signals. Reproduced from Ref. [134] with permission from John Wiley and Sons.

Recent studies have reported new strategies to simultaneous trap and rotate the cells by the simultaneous application of DEP and ROT signals. First, Han et al. proposed the modulation of the two signals, one on top of the other, to trap single cells in a octopole cage [138] (Fig. 1.3.a). However, as the two signals might interact with each other, the bandwidth of the ROT signal is limited and the spatial modulation of the two signals was proposed to increase the range of the ROT signals [134] (Fig. 1.3).

1.2.4 Measurement of rotation speed and parameter extraction

As ROT is generally targeted at the extraction of cell parameters, it is important to extract the rotation speed and the particle's parameters.

Measuring the rotation speed

While the first ROT setups were based on the recording of the cell rotation with extraction of the rotation speed by the experimenter, more elaborate systems have been developed. One such approach was the method for single- particle dynamics (MOSPAD), where a small rectangular opening is placed between the sample and the microscope optics. The opening is smaller than a single cell and the light intensity passing through the slit is acquired. The rotation speed is then measured as the periodicity of the intensity signal. This method enables a more automated extraction of the rotation speed; however, at least one full cell rotation is needed to extract the speed of rotation. This requirement increases the acquisition time, especially for slow rotation speeds[114].

On the other hand, increased calculation power led to new developments of computer algorithms for fast and accurate cell tracking. Such algorithms were used for real-time monitoring of rotation speed on automated setups [65, 139]. The extraction of the rotation speed was

achieved in about 15 seconds and a full spectrum with 20 frequencies could be acquired in 5 min. However, the measurements were less precise with mammalian cells, due to the deformation or restructuring of the organelles [65]. The use of cross-correlation tracking and feature point tracking were studied and compared to be used for the extraction of cell rotation speed. While accurate rotation detection with both methods was reported, the cross-correlation tracking method achieved higher efficiency [140]. Finally, circular spatial filtering velocimetry (CSFV) was tested for ROT experiments and cell rotation speeds in the order of 1-100 s per revolutions were observed. Combined with high-speed imaging at 2500 frames per second, they monitored field-on effects and reported linear torque-friction behavior during the cell acceleration [141]. However, one of the problems was that the algorithms were not implemented shift-invariant and for this reason, small motion of the particle in the x-y direction might have affected the measurements [141].

Parameter extraction

Extraction of the cell parameters from ROT experiments is challenging, since the underlying formulas are complex and non-linear. While some parameters can be extracted from the ROT spectrum with high accuracy, others are almost impossible to extract via standard curve fitting [62]. For this reason, the use of frequency-dependent coefficients for the fitting procedure was proposed to improve the fitting accuracy. In addition, an optimized fitting algorithm with bounded intervals for each parameter was proposed and both measures were shown to increase the confidence levels of the extracted parameters [63].

Another option for extracting the electrical cell parameters is by acquiring the peak rotation frequency for different medium conductivities. For this method, linear fitting is performed on the peak rotation frequency vs. the medium conductivity. It is then possible to deduce the membrane capacitance and conductance from the slope and the intercept of the fitted line [61]. However, such measurements are hard to be performed on single cells and thus the extracted parameters refer to the average cell population.

"There are no old roads to new directions."

—Advertisement of the Boston Consulting Group

2

3D electrodes for ROT experiments

We saw in the previous chapter there were some groups that used 3D electrodes for electrorotation experiments, however, these electrodes had mostly big inter-electrode distances. This chapter focuses on the use of 3D electrodes for electrorotation experiments, and will start by comparing 3D electrodes with planar ones by means of modeling. The second part of this chapter will then focus on the fabrication of 3D electrodes where we present two new fabrication processes for 3D electrodes that were developed in the framework of this thesis. Finally, the chapter concludes with ROT experiments that were performed on chips with 3D electrodes.

2.1 *In-silico* comparison of 3D and planar electrodes for ROT applications

A commercially available simulation software (Comsol Multiphysics) was used to compare the ROT torque and DEP forces. For ease of reading, this chapter will only focus on the main simulation parameters, while a full description with all the parameters and options can be found in Annex A.

The electrodes were designed in a parabolic shape with an inter-electrode distance of $40\,\mu m$. The planar electrodes were defined on the surface, while the 3D electrodes were extruded through the full height of the microfluidic channel ($50\,\mu m$). The electrode sidewalls were defined as platinum, and the surrounding medium inside the rotation chamber was defined as water, with a conductivity adjusted to $100\,\mu S/m$.

We applied a sinusoidal electrical signal with a frequency of $100\,kHz$ and a phase distortion of $\Pi/2$ between neighboring electrodes. The model was solved with a frequency-dependent solver for the ROT torque and a time-dependent solver for the DEP forces. The visualization of the ROT torque is based on the expression of the effective torque moment, described by M.P. Hughes [142]:

$$E_{eff}^2 = \begin{pmatrix} E_{z0}E_{y0}\sin\left(\varphi_{z0}-\varphi_{y0}\right) \\ E_{x0}E_{z0}\sin\left(\varphi_{x0}-\varphi_{z0}\right) \\ E_{y0}E_{x0}\sin\left(\varphi_{y0}-\varphi_{x0}\right) \end{pmatrix} \tag{2.1}$$

while the DEP force is given by [143]:

$$F_{DEP} = 2\pi\varepsilon_0\varepsilon_r r^3 \text{Re}\left[f_{cm}\left(\omega\right)\right]\nabla E^2 \tag{2.2}$$

For the visualization, we only considered the electric field square ∇E^2, as this is the contribution of the electrode geometry to the DEP force and we integrated this gradient over one full period of the ROT signal.

2.1.1 Simulation of the rotation torque

We start our comparison with the strength of the ROT torque for different signal amplitudes ranging from 0 to $5\,V$. The vertical electrodes have the advantage of applying the electric potential over the full height of the channel. For this reason, there is no z-dependence of the electric field. This is not the case for the planar electrodes, as they apply the signal only from the bottom of the chamber. The electric field declines rapidly with distance from the electrodes, and as a result, the ROT torque decreases with height. For this reason, the torque moment generated by vertical electrodes at mid-channel height is higher than that generated by planar electrodes (Fig. 2.1). In other words, 3D electrodes require a lower voltage to achieve a certain rotation torque. In the case of a signal with an amplitude of $5\,V$ that is applied to the planar electrodes, a torque moment of $1.1*10^9\,V^2/m^2$ results. On the other hand, for vertical electrodes, an amplitude of $1.5\,V$ is sufficient to generate a similar torque of $1.2*10^9\,V^2/m^2$ (Fig. 2.1, red stars). As the ROT torque is one of the most important parameters during ROT experiments, we will consider these two values for comparison in the simulations that follow.

Next, we compare the distribution and evaluation of the electric field in the x-y and x-z planes (Fig. 2.2). For the same reason as mentioned above, the 3D electrodes not only achieve greater efficiency, but also result in a more uniform distribution of the ROT torque (Fig. 2.2.a and b). To compare the area that results in a maximum deviation of $\pm10\%$, we extracted the maximal radius of a circle that can be fitted inside this area. The measurements confirm the previous
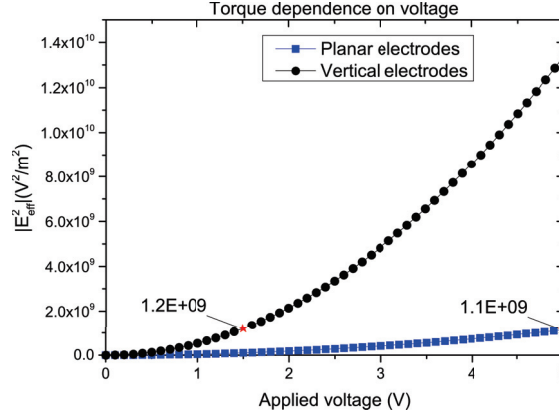
Figure 2.1 – Dependence of the effective torque moment on the amplitude of the applied signal for vertical and planar electrodes. The stars indicate the voltages that result in a similar torque moment.

finding, with a circle radius of $17.0\,\mu m$ for the vertical electrodes, compared to $15.7\,\mu m$ for the planar ones. Although there is a slight difference in the x-y plane, it is much more prominent by comparing the x-z plane. The vertical electrodes do not lead to any dependence on the z-direction, and their torque distribution is the same at any height inside the ROT chamber (Fig. 2.2.c). However, the planar electrodes lead to a ROT torque with high dependence on the z-position. A change of only few μm can cause a change in rotational torque of more than $\pm 10\%$ (Fig. 2.2.d).

Another illustration of the previous finding is the plotting of the ROT torque along the z-axis in the center of the chamber (Fig. 2.3). Again, the vertical electrodes result in a constant rotational torque over the full ROT chamber, while planar electrodes create a torque that depends on the z-position. It is the highest at the bottom of the chamber and rapidly decreases over the full chamber height by an approximate factor of 4.

The z-component of the rotation torque is generally the most important component, as it is the easiest to observe. However, there are also components in x and y directions (see eq. 2.1 and Fig. 2.4)which might impact the extraction of the cell rotation speed.

From eq. 2.1, the torque components in the x and y plane vanish in the case of the vertical electrodes, as the z-component of the electric field (E_{z0}) is zero. For this reason, the torque of the vertical electrodes is strictly in the z-direction throughout the chamber (Fig. 2.4.a). However, this does not hold through for planar electrodes, as a z-component results. Although the z-component is rather small in the center of the electrodes, it becomes more prominent on the borders of the chamber, particularly right above the electrodes. The torque moment declines toward the horizontal direction (Fig. 2.4.b).
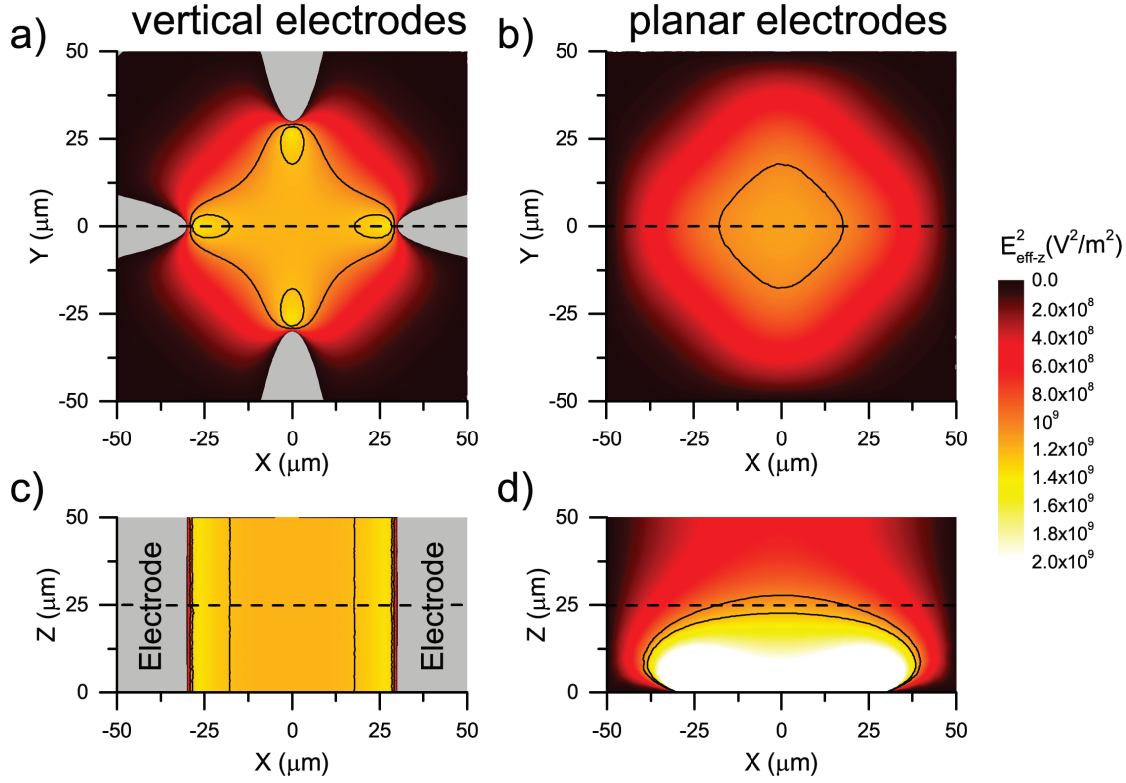
Figure 2.2 – z-component of the generated effective torque moment for vertical (a, c) and planar (b, d) electrodes for cut planes parallel (a, b) and vertical (c, d) to the bottom of the chamber. The color indicates the strength of the torque in z-direction, and the lines indicate a difference in strength of ± 10% in respect to the value in the center of the rotational chamber. The dashed lines indicate the cut planes.

2.1.2 Simulation of the DEP forces for planar and vertical electrodes

For ROT experiments, DEP forces are mostly considered as parasitic, as they will induce particle motion and as the ROT torque is not uniform throughout the ROT chamber, the DEP forces can disrupt a ROT experiments. Although nDEP forces generally stabilize the particles by pushing them in towards the electrode center, pDEP forces destabilize them and pull them towards the electrodes. While the DEP forces depend on many parameters, (such as frequency, choice of medium, and intrinsic properties of the particles), we will base our comparison solely on the gradient of the field square, as this is the part of the DEP force that is given by the electrodes (Eq. 2.1). All the other parameters are experimental and can be adjusted for the different experiments. Furthermore, it was already demonstrated that 3D electrodes can be used for more efficient particle trapping with DEP forces [144]. For this reason, we will mainly focus our discussion on the DEP forces that result from the application of the ROT signals. Finally, with the goal to use the electrical tweezers approach, the amplitude ratio of DEP to ROT signal can be adjusted to achieve stable trapping.

We compared the simulated forces in the x-z (Fig. 2.5 a and b), and the x-y plane (Fig. 2.5 c and
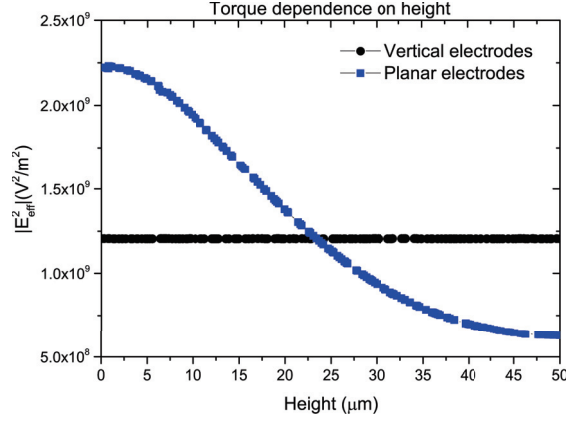
Figure 2.3 – The z-component of the effective torque moment in the center of the rotation chamber as a function of the height inside the ROT chamber for planar and vertical electrodes.
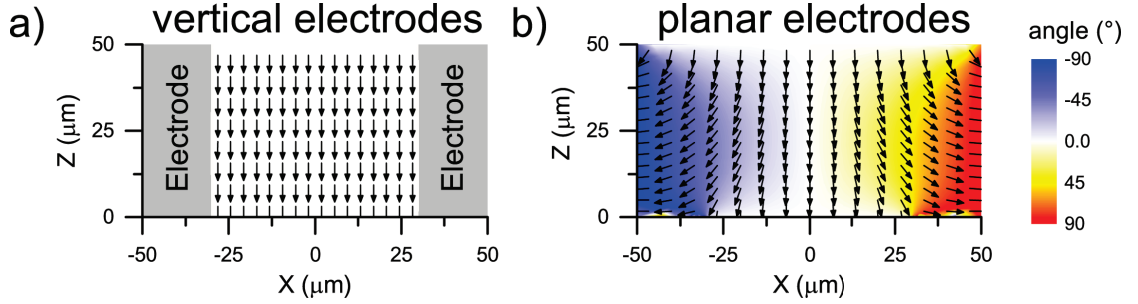
Figure 2.4 – Direction of the ROT torque for vertical (a) and planar (b) electrodes inside the ROT chamber. The vectors are normalized and indicate the direction of the effective torque moment, while the surface colors indicate the angle between the torque vector and the z-axis.

d). The simulations were performed with the parameters found in Annex A.1. For the same reason as above, the vertical electrodes generate electrical fields without a z-component, so neither a field gradient nor DEP forces result in the z-direction (Fig. 2.5.a). Consequently, as the planar electrodes lead to an electric field with a z-component, it can be seen that DEP forces result in this direction as well (Fig. 2.5.b). This z-component is the highest right above the planar electrodes and decreases toward the center of the chamber. Such forces in the z-direction are particularly critical in the case of planar electrodes, as the ROT torque also depends on the z-position.

Furthermore, the DEP-force changes the direction in x from bottom to top, where the reversal appears in the center of the chamber (Fig. 2.5.b). This observation makes the discussion of the DEP in the x-y plane more problematic, as the pattern will change with height (Fig. 2.6). The particle height during the rotation experiment can be found by using DEP levitation theory, in which, gravitational forces are balanced against the DEP forces [145]. The exact particle height depends on many parameters. A thorough analysis of these parameters on the particle height can be found in [146], where the case of latex beads were analyzed and the results for an electrode spacing of $40\,\mu m$, showed that the particles can be levitated up to $80\,\mu m$ with a
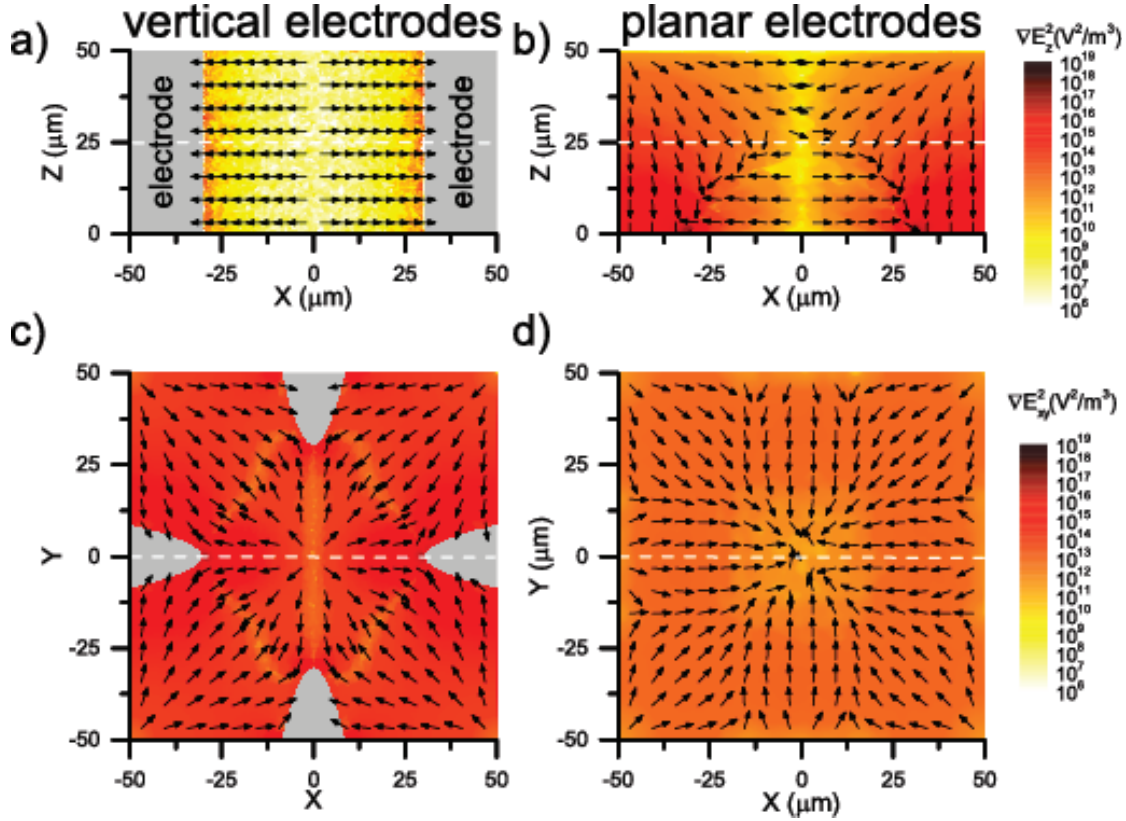
Figure 2.5 – Uniformity of the gradient of the electric field square for vertical (a, c) and planar (b, d) electrodes in vertical (a, b) and horizontal (c, d) cut planes. The arrows are normalized and show the direction of the DEP force, while the color scale indicates either the z-component (a, b) or the magnitude in the x-y plane (c, d). The dashed lines indicate the position of the cut planes.

signal of 8 V_{p-p}. Although the maximal height might be adjusted by different parameters, this example shows the importance levitation might have on the particle positioning.

Although a reduced z-component of the DEP force is mostly positive, it is more complicated for the DEP forces in the x-y direction, which can have both stabilizing and destabilizing effects. In order to get an accurate extraction of the particles spectrum, it is important that the particles stay at a fixed position, either because the DEP forces are low enough, or they are trapped and held in position. For this reason, the DEP forces should either be small enough, so that they will not move the particles, or they should be of negative nature to result in particle centering. Nevertheless, small electrodes in general lead to higher field curvature and thus higher DEP forces. For this reason, we decided to use signal modulation to induce DEP and ROT at the same time and we mainly focus our analysis on the ratio of the DEP forces generated by the 90° (ROT) and 180° (DEP) phase-shifted signals to guarantee efficient trapping. While the distribution and the gradient of the electric field square is given by the electrodes, the force ratio can be adjusted by applying different amplitudes for the DEP and the ROT signal. We
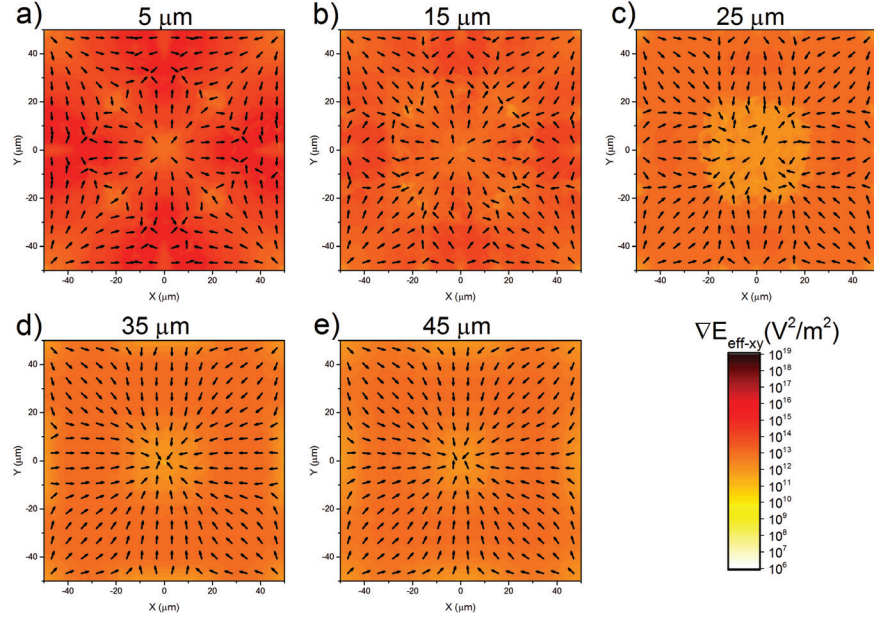
Figure 2.6 – z-stack of DEP forces in the x-y plane resulting from planar electrodes. The different images show the cut along different heights. At lower heights (a:5 μm and b:15 μm), the DEP forces will center the particle under nDEP conditions, while nDEP conditions will destabilize the particles at greater heights (d: 35 μm and e: 45 μm). Finally, the forces change direction in the center (c: 25μm). The arrows are normalized to indicate only the direction. The color indicates the strength of the DEP forces.

only show the results for one voltage here, while the linearity of the Laplace's equation allows to apply standard scaling laws to obtain the forces for different amplitudes. For this reason, we are mostly concerned about the force pattern than the absolute value and are mostly concerned that the electrodes will center the particle at any height. Although this works quite well for the 3D electrodes (Fig. 2.5.a and c), it is not the case for the planar ones (Fig. 2.5.b and c). In cases where the particles levitate above the center of the chamber, the trap can become unstable [100]

However, the bigger problem is that the planar electrodes cannot achieve as high a trapping force as the 3D electrodes. Although it might be possible to increase the signal amplitude, the cells will start to levitate as soon as the DEP force overcome the gravitational forces. This will, on one hand, lead to a decrease in DEP trapping force, as the cells will be further away from the electrodes, and on the other hand, the energy landscape will change with height and the trap becomes unstable, as we saw above [100]. On the contrary, 3D electrodes span the full channel height and thus an increase in signal amplitude will enforce the DEP barrier, but without cell

levitation, as the electric field has no z-component. Furthermore, the signal is applied over the full channel height, which results in bigger DEP-trapping forces of 3D electrodes than the planar ones[144]. As already mentioned in the beginning of this chapter, such strong DEP forces can be used to ensure stable particle positioning during the ROT experiments, through the electrical tweezers approach [134].

2.1.3   Electric field peaks and Joule heating

Other aspects that have to be considered, are high field peaks and heating effects, as both of them can harm the particles and the electrodes. For this reason, we will first consider the maximal electric field peaks and then discuss local and global heating effects. Moreover, planar electrodes apply the signal only on a very small surface, which leads to a high field density on the electrode edges and thus, high electric field peaks result. In comparison, the 3D electrodes have a much bigger surface and therefore, the electric field is applied over the full channel height, resulting in much lower peaks of the electric field in general (Fig. 2.7.a). However, when the voltages are adjusted to result in similar torque moment, the electric field peaks originating from vertical electrodes are further reduced. Although the field peaks are less problematic in the case of nDEP, they can become critical in the case of pDEP, where cells are directly attracted to the electrode edges. Furthermore, such peaks might damage the electrodes by electro-erosion.

On the other hand, Heating might also damage cells and electrodes and the high electric fields used for dielectrophoresis can lead to a high power density generated in the fluid surrounding the electrodes. This power per unit volume can be calculated as:

$$W = \sigma_m E^2 \tag{2.3}$$

where E is the electric field and σ_m stands for the electric conductivity of the medium. From equation 2.3 one can see that the generated power not only depends on the electric field, but also on the conductivity of the medium. Assuming a general field strength of $10^5\,V m^{-1}$ and a low medium conductivity of $10\,mS m^{-1}$, as generally used for DEP and ROT experiments, a total power dissipation of $10\,mW$ results.

However, as the main goal of this chapter is to compare planar and vertical electrodes, we will do this comparison at a given medium conductivity ($100\,\mu S m^{-1}$). This allows the comparison of heat generation of the two types of electrodes. While the actual heating would also be dependent on the medium conductivity, we assume that in both cases the experiments would be performed at the same conductivity and thus heating would scale similarly in both cases.

We already saw that the maximal field strength of planar electrodes is much bigger than the one of vertical ones, and therefore, according to eq. 2.3 also more heating results. However,
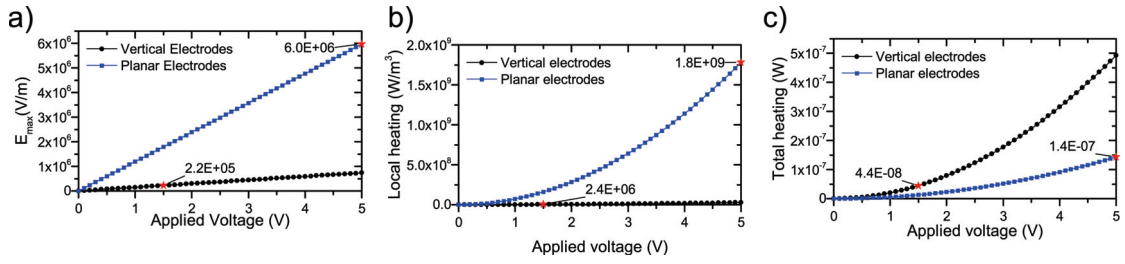
Figure 2.7 – Analysis of electric fields and induced heating by vertical and planar electrodes from 0 to 5 V. The plots show a) the maximum electric field at the surface of the electrodes, b) the maximum heat dissipation at the electrode surface, and c) the total heat generated by the electrodes. Points of equal torque moment are highlighted with red stars

this effect is even more prominent, as the heating is proportional to E^2 and a difference in local heating of almost three orders of magnitudes results when the planar and vertical electrodes are compared to each other (Fig. 2.7.b). On one side, local heating can cause damage to the electrodes and on the other side, it leads to electro-thermal effects that are caused by temperature gradients. This gradient leads to an increase in temperature of the liquid, which will induce thermal motion of the medium. Finally, such vortices can interfere with the ROT or DEP experiments. Finally, as the planar electrodes lead to more local heating, such effects are more striking. In addition, as the vertical electrodes will heat the medium along the full electrode surface, heating is more uniform and thus it is harder to establish liquid streams, which would also follow a different pattern. Although such motion was observed during ROT experiments at higher voltages, it was not investigated in more details, nor was it characterized.

Finally, the total heat generated by the electrodes can be calculated by the integration of the local heat dissipation over the full electrode surface. Although local heat generation is higher for planar surfaces, the bigger electrode surface of the vertical electrodes results in more overall heat dissipation at a given voltage. However, as the vertical electrodes are more efficient in generating the rotation torque, the signal amplitude can be lowered and thus heat dissipation also decreases, so that overall, for similar torque moment, less heating occurs with vertical electrodes (Fig. 2.7.c stars).

2.2 Microfabrication

Recent developments in microfabrication technologies enabled the fabrication of smaller devices and constantly increased the resolution for microchip fabrication. Nevertheless, most microfabrication processes are planar and limited to thin features, generally in the sub-micrometer domain. There are only a few microfabrication processes that enable micro-electrodes with thicknesses above few μm.

2.2.1 Fabrication of 3D electrodes - State of the art

The probably best-known process to fabricate 3D microelectrodes is electroplating, which is based on the reduction of cations in an electrochemical reaction to form a coherent metal coating on a planar electrode. This process comes in two variations, one with the application of a current to favor metal deposition [144, 147] and one without a current [148, 149]. Although electroplating has applications in many industrial processes, its principal application in microfabrication is mostly through combination with a mold to control the shape and size of microstructures. Electroplating normally consists of different steps: Application and patterning of the seed layer; formation of a mold to constrain and define the electrode design; metal deposition; and dissolution of the mold. There are some disadvantages to this process, including that the composition of the ionic bath must be carefully monitored or otherwise, the surface quality of the metallic structures might be negatively affected. Moreover, it is important to achieve uniform current densities all over the wafer and the structures, to avoid non-uniform growth or poor layer properties [150]. Such drawbacks result design constraints and limit the cross-section of the electrodes. Likewise, the seed layer must be designed with great care, as the individual electrodes must be singularly addressable. The different pads must be similarly connected so that equal current density will result for each pad. Otherwise, non-uniform heights of the electrode structures may occur. Furthermore, the metal composition is limited by the availability of electroplating baths, and a special bath is required for each metal [150]. Finally, commonly used metals, such as Au or Pt, come at a high cost. While the amount of deposited metal is low in the case of thin film techniques, it cannot be neglected in the case of bulky electrodes resulting from techniques such as electroplating.

An alternative fabrication process involves pyrolysis of polymeric precursors to create glassy carbon-like electrodes, or the so-called *C-MEMS* [151]. Although a wide range of polymeric precursor can be used for this process, SU-8 is the most common one. Its main advantages are the possibility to achieve structures up to $200\,\mu m$ in a single coating step, aspect ratios up to 20:1, and high-resolution patterning. Nevertheless, the fabricated structures generally undergo 50 to 70 percent precursor shrinkage during pyrolysis [152], leading to design constraints. Besides limiting the height of the structures, it impedes the creation of sharp corners. In addition, the shrinkage, although isotropic, is less prominent at the base of the pillars, as adherence to the substrate limits the possibility to shrink. For the same reason, only a limited number of substrates are available for this technique. C-MEMS processes have been demonstrated on either Si substrates, with or without SiO_2 coating, and on fused silica [153]. However, the most important disadvantage of such electrodes is their rather low conductivity, which is about three orders of magnitude lower than the one of metal electrodes [154].

Finally, other processes were proposed based on mixing conductive particles, such as silver or carbon, into polymeric precursors (SU-8 or PDMS) [155, 156, 157, 158]. Although SU-8 can be patterned by means of photolithography, there are only few techniques that can pattern PDMS. While it is possible to use photosensitive precursors [158], this generally leads to a very limited resolution, with minimal feature sizes in the range of $100\,\mu m$. On the other hand,

PDMS can be molded, but careful control of the applied PDMS volume is vital. Otherwise, connections on the top or bottom of the electrodes (depending on the complete fabrication process) might result. Another option is to use ion-implantation techniques [159]. However, the biggest drawback for all of these fabrication processes is the low conductivity of the electrode structures.

While this short description covers the most common used fabrication processes, a more detailed description can be found in [160]. However, there is a real need for further fabrication processes to realize 3D electrodes, and the main requirements to do so are the ability to create electrode structures that span the full height of the microfluidic channels; being either integrated into channel side-walls or being freestanding; and have good conductivity in the range of the ones of metals. For these reasons, the framework of this thesis includes some new fabrication processes for 3D electrodes, based on uniform coating of insulating structures with metals. In a first process, we used passivated silicon structures [161] and then moved to a more convenient fabrication process based on SU-8 structures [162]. For the ease of reading, this chapter just discusses the most important fabrication parameters. A full process description can be found in Appendix B.

2.2.2 Metal-coated silicon structures

The fabrication process starts with the dry etching of the 3D topography into the silicon substrate. We chose this approach, since photolithography and Bosch etching enable high spatial resolution and aspect ratios of 20:1. To prevent short-circuiting through the silicon substrate, the structures are then passivated by a $1\,\mu m$ thick silicon dioxide layer applied by CVD. The structures and substrates are then homogeneously covered in metal by sputter coating of a $20\,nm$ Ti adhesion layer and a $200\,nm$ Pt layer. Finally another $20\,nm$ Ti adhesion layer is applied by evaporation to improve the adhesion of a passivation layer that is deposited later. As the passivation layer is only applied to the horizontal planes, it is deposited by evaporation, which guarantees much higher directionality, and avoids Ti contamination on the vertical sidewalls. The structuring of the metal layer is then done through photolithography and metal etching. While the photoresist was applied by spray coating, due to the high topography of the substrate [161].

The main novelty of this process is the use of sputter coating to uniformly cover high topographic features. For this reason, we designed different test structures and carried out different characterization steps to investigate on the uniformity and properties of the metal layer.

First, we fabricated arrays of 5x3 pillars (Fig. 2.8) to conduct resistive measurements and to confirm the connection between planar and vertical metal layers. The arrays contained either round or rectangular pillars, of sizes between $10\,\mu m$ and $70\,\mu m$, and gaps between $10\,\mu m$ and $60\,\mu m$. The arrays were designed with connection pads on either side of each line to measure the five pillars in series.
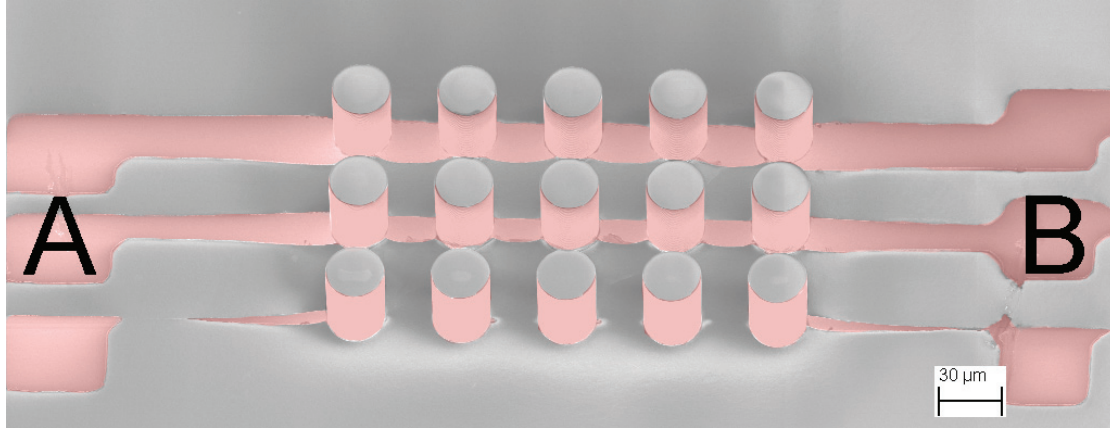
Figure 2.8 – An SEM image of an array test structure used for the electrical characterization of the vertical electrodes. The array consists of three lines with five round-shaped micropillars. The pillars have a diameter of $30\,\mu m$, with a $20\,\mu m$ gap between them. Each line is connected with a planar metal line of different widths, ranging from $10\,\mu m$ to $30\,\mu m$.

Table 2.1 – The extracted values of the electrical parameters of the micro-pillar electrodes from the fitting procedure shown in Fig. 2.11.b.

	$R_{buffer}\,(\Omega)$	$CPE_{DL}(Q)\,(nF)$	$CPE_{DL}\,(\alpha)$	$C_{stray}\,(pF)$	$R_{PAR}\,(\Omega)$	$C_{PAR}\,(pF)$
Value	12246	1.26	0.88	2.82	7206	0.36
Error (%)	2.9	1.6	0.2	1.5	0.5	0.3

From these measurements, we found that the width of the gaps strongly influenced the resistance (Fig. 2.9.a). Furthermore, we compared different widths of the connection lines and found that the resistance and its variability increased for smaller lines (Fig. 2.9.b).

In addition, we performed SEM imaging, combined with energy-dispersive X-ray (EDX) analysis of pillars and their cross-sections. The latter was performed on a chip that was previously cleaved. By imaging the cross-section, we visualized the presence and uniformity of the metal film on the silicon pillars (Fig. 2.10.a and b) and confirmed the presence of the metal layer by EDX analysis (Fig. 2.10.c).

The next step was to ensure the proper exposure of the vertical metal layers. For this purpose, we fabricated pillars with facing sidewalls and gaps of $40\,\mu m$ in a $160\,\mu m$ wide microfluidic channel obtained by bonding a PDMS cover on top of the chips. These chips were used to extract the double-layer capacitance of the electrodes by impedance measurements. The AC measurements were performed in air and in aqueous solution (1x PBS). The comparison of the two measurements qualitatively shows the exposure of the electrodes to their surroundings (Fig. 2.11.a). The parameters of the electrode interface listed in Table 2.1 were extracted by fitting the measurements in aqueous solution to the electrical circuit shown in Fig. 2.11.b and we found a close fit of the theoretical and the experimental data (Fig. 2.11.c).
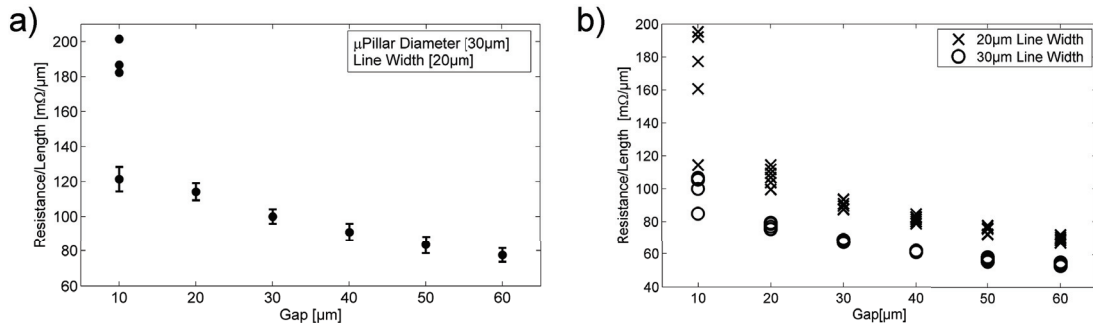
Figure 2.9 – Resistive measurements of different micro-pillar arrays. a) the mean resistance and its variability (18 chips) of an array, normalized by its length for different gap widths. For the arrays with a $10\,\mu m$ gap, the three separately indicated measurement points were substantially higher than the rest. b) The influence of the connection-line width on array resistance normalized by its length. The measurements were performed on pillars with different diameters, ranging from $20\,\mu m$ to $70\,\mu m$.

However, this process has several drawbacks. First, we observed shrinkage of planar lines caused by the overexposure of the photoresist that was needed to achieve proper patterning inside the arrays (Fig. 2.12). Although we found that the shrinking of the lines was quite constant for planar features, with a mean shrinking of around $7\,\mu m$ (Fig. 2.12.b), the patterning inside arrays of 3D electrode arrays is less uniform. For instance, there was less shrinkage inside different pillar arrays (Fig. 2.11.c and d). Moreover, the patterning of the connection lines is limited by the spray coating to arrays with gaps bigger than $20\,\mu m$. Second, the dry-etching step for the 3D scaffolds imposes some design restrictions, such as the maximal amount of exposed silicon surface and the etching receipt must be optimized to work properly when big silicon structures are exposed, otherwise black silicon might form [163]. If a tool with mechanical clamping is used, it is not possible to etch all the way to the border and the resulting frame around the wafer can interfere with later processing steps, such as spin coating of photoresists. Third, as the pillars are etched into the substrate, there is a restriction in the choice of substrates. Pillar fabrication on glass is already time- and cost-intensive, while silicon structures will have the typical scallops on the pillar sidewalls. Fourth, the fabrication cost of this process is rather high, with many different steps and tools needed and as the structures are in silicon, an additional insulation step to prevent short-circuits through the silicon substrate is needed.

2.2.3 Metal-coated SU-8 structures

For the above-mentioned drawbacks, we developed a further fabrication process based on homogeneously coating of SU-8 structures with metal [162]. The advantage of SU-8 is that it is possible to achieve high aspect-ratio structures, with good chemical properties and smooth side-walls in a single photolithography process. Furthermore, the additive nature of the photoresist enables the use of different substrates. For the main part of the devices fabricated
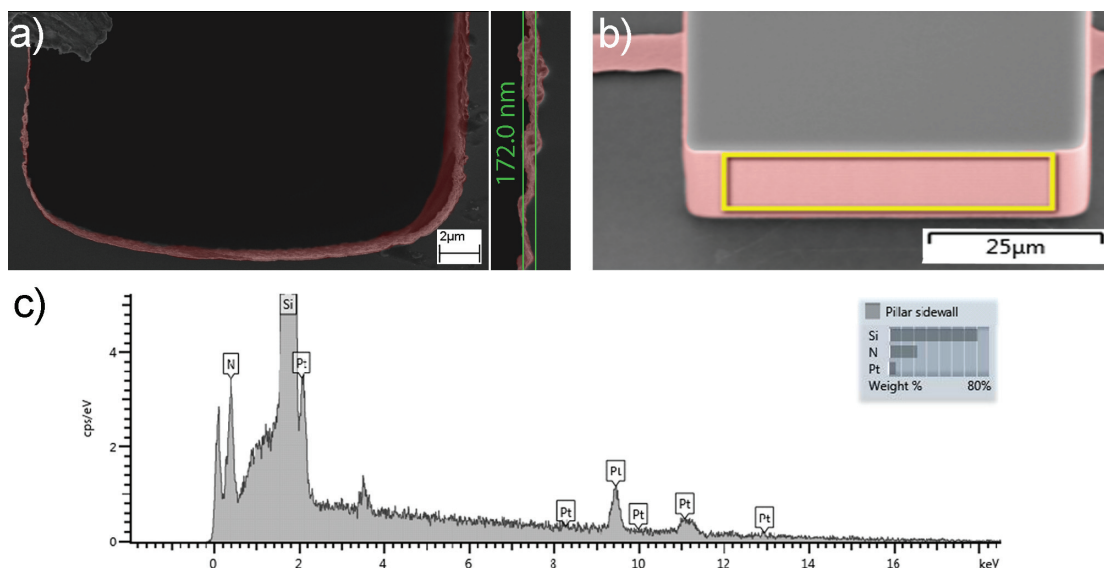
Figure 2.10 – Verification of the presence of the metal layer on the vertical sidewalls. a) SEM image of a gap between two pillars, showing the presence of the metal. b) SEM of the pillar used for the EDX analysis, with the square indicating the measured region. c) EDX spectrum of the vertical pillar sidewall, showing the Pt metal layer.

for this thesis, we worked on silicon substrates, but the process was performed on glass as well.

The first step was to optimize the adhesion of the metal layer on the SU-8 substrate. We investigated different process variations, including a hard bake and activating the polymeric structures with oxygen plasma at different intensities. We tested the adhesion on different structures, from small to big sizes, and found that the hard bake was essential for the tested structures to prevent cracks and peeling off of the metal. In cases with hard bake, the metal adhered on the structures, but plasma activation was needed to achieve a good result. In cases without activation, many cracks resulted on both smaller and bigger structures (Fig. 2.13.a and d). A moderate plasma activation (200 Watt) improved the adhesion in both cases (Fig. 2.13.b and d), but was only good for the smaller structures. Finally, with the highest activation (500 Watt) we achieved sufficient adhesion on both small and big structures (Fig. 2.13. c and e).

Patterning of connection lines by means of dry-film photoresist

Although it might be possible to use spray coating for the patterning, we decided to use a dry-film resist to structure the metal connection lines. The resist was applied on top of the structures, and the metal layer was patterned by dry etching (Fig. 2.14. c and d). The advantage of this approach is that it is quick and cost-effective, without any need for special tools. However, the resolution of the metal patterning is limited by the dry-film. We used a
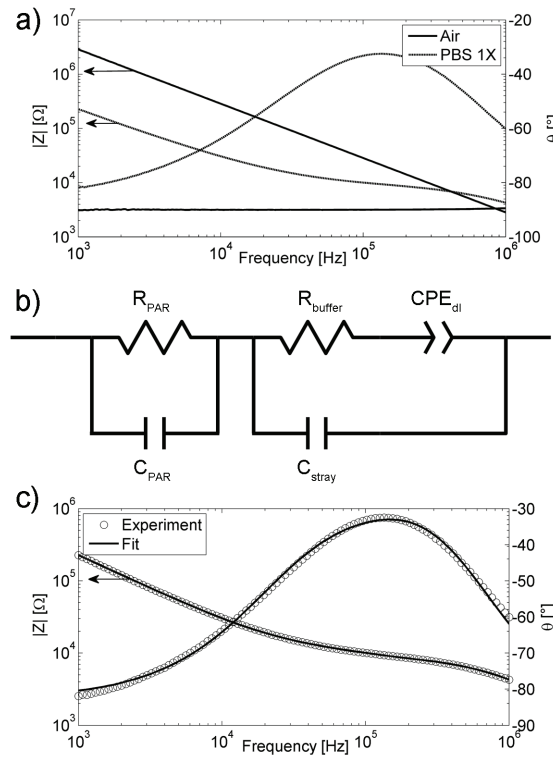
Figure 2.11 – Verification of the proper exposure of the vertical metal sidewalls by impedance spectroscopy. a) The modulus and phase of two pillars in dry (solid lines) and wet (dashed line) conditions. b) The equivalent circuit used to fit the experimental data. c) plot of the fitting results with the experimental data.

film of a thickness similar to the height of the 3D pillars, in combination with vertical flanges designed on the sides of the pillar sidewalls to achieve sufficient adhesion of the film on the 3D topography (Fig. 2.15.b). The limitation comes with the rather low patterning resolution of the resist, which is generally in the range of their thickness (Fig. 2.15.c).

Patterning of connection lines by means of lift-off

Due to the limitation in resolution, we decided to profit from the additive nature of the process and pattern the connection lines at the beginning of the process on the flat substrate (Fig. 2.16.a). We chose to deposit the metals by a lift-off process, although patterning by dry etching upon metal deposition would be possible as well. The 3D SU-8 structures are then formed on top of the connection lines and are homogenously covered in metal by sputter coating (Fig. 2.16.c). Finally, the excess metal on the horizontal surfaces is removed by anisotropic metal etching (Fig. 2.16.d). We used secondary ions mass spectroscopy (SIMS) to monitor this etching process and stop it once we etched through the top metal layer. This is especially important, as we do not apply any etch mask, and etching too long might remove
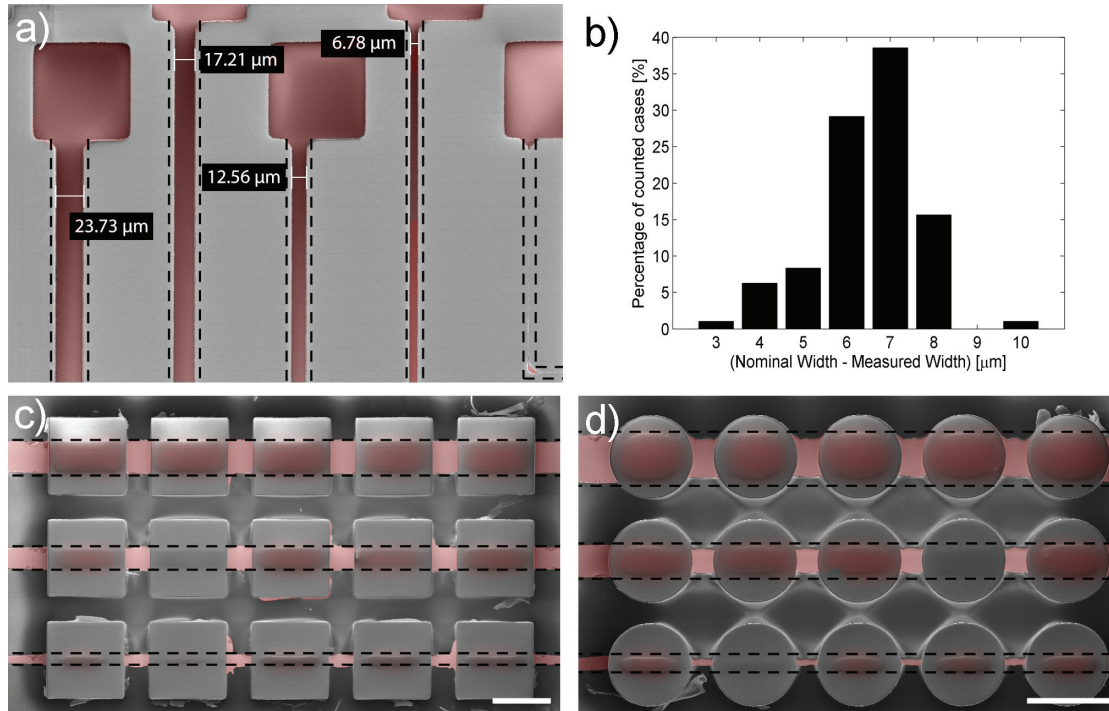
Figure 2.12 – Characterization of metal line shrinkage caused by photoresist over-exposure. a) SEM image of planar metal lines, with the dashed lines indicating the original designs of the lines. b) The mean shrinkage of 96 different connection lines was found to be approximately $7\,\mu m$. c-d) Patterning of metal lines into arrays of rectangular (c) and round (d) pillars. The scale bars indicate $50\,\mu m$

the underlying metal layer deposited at the beginning of the fabrication process.

With this lift-off process, we achieved $50\,\mu m$ high structures, with diameters down to $20\,\mu m$ and gaps of $10\,\mu m$, and each pillar singularly addressed with lines of $5\,\mu m$ (Fig. 2.17.a). In addition, it is possible to combine planar and vertical electrode features, thanks to the high alignment accuracy (Fig. 2.17.a and b). Finally, we carried out SEM imaging (Fig. 2.17.c), EDX analysis, and electrical measurements (Section 2.2.4) to proof the proper connection.

2.2.4 Electrical characterization of metal-coated SU-8 structures

In addition to having better patterning resolution, the lift-off process also enables new possibilities to characterize the electrodes and the connections of bottom and sidewall metal layers. For example, it is possible to achieve pillar structures that are connected from each side. Such structures enable extraction of additional resistance due to a single pillar by simple DC measurements. For this reason, we fabricated such pillars, connected by planar wires on each side, but without a continuous metal layer on the bottom. From 192 measurements on such test structures, we found a proper connection of planar and vertical metal layers in 93 percent of the cases. By comparing the measurements to planar connection lines, we found that a
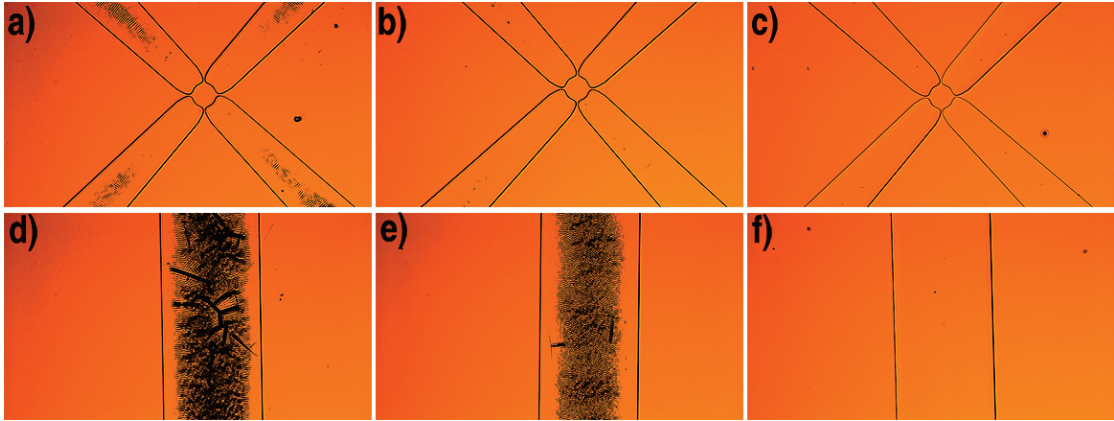
Figure 2.13 – Microscopic images of structures that were treated with different activation protocols before metal deposition. Without activation, no good metal adhesion is achieved on either small (a) or large (d) structures. Moderate activation (200 W) increases adhesion of metal on small SU-8 structures (b), but is not sufficient for big ones (e). Only activation at 500 W is sufficient to achieve good adhesion on small (c) and large (f) structures.
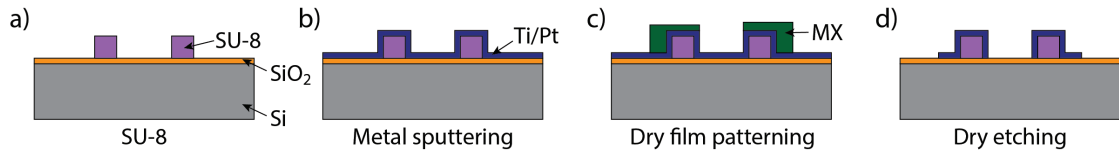
Figure 2.14 – Illustration of the microfabrication process for free-standing metal-coated pillars with patterning of the connection lines by dry-film processing. First, the 3D scaffolds are patterned in SU-8 (a) and covered with a sputter-coated titanium (Ti) and platinum (Pt) layer (b). A dry-film resist (Dupont MX) is then applied to the wafer (c), which serves as an etch mask during metal etching (d).

single pillar caused a resistance increase of $12.56 \pm 0.52\,\Omega$ (Fig. 2.18.a). While the resistance is already low, it would be even lower for the final structures because the resistance is measured twice (on each side of the pillars) and the final contact length between the planar and the vertical layer is on the full perimeter and not only on half of it.

We next fabricated some rectangular pillars of different lengths to extract the sheet resistance of the vertical metal layers and compare it with the resistance of the planar ones (Fig. 2.19.b). For this, we first measured the planar wires and extracted its sheet resistance (Fig. 2.18.b $\square$) and then measured the complete test structures. Finally, the sheet resistance was deduced by the substraction of the resistance from the planar lines and deviding by the number of squares (Fig. 2.18.b $\diamondsuit$). As expected in both cases, we found a linear behavior of the resistance and the length of the structures. However, the sheet resistance of the vertical metal layers was slightly higher than that of the planar wires ($1.80\,\Omega/\square$ vs. $1.14\,\Omega/\square$). This can be explained by the not-fully isotropic deposition of the sputtering, resulting in a thinner metal film on the vertical sidewalls. Furthermore, the plot shows that the linear fits have a different offset on the y-axis. The offset for the planar wires is due to the use of a two-point measurement
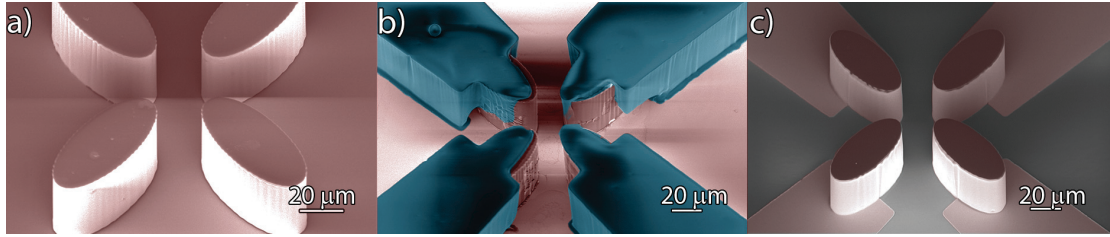
Figure 2.15 – SEM images of 3D electrodes consisting of metal-coated SU-8 scaffolds patterned by dry-film resist. The sputter coating results in a homogenous coating of the SU-8 scaffolds (a). Dry-film resist is then applied to mask the connection lines during the etching process (b) and is removed after the etching (c).
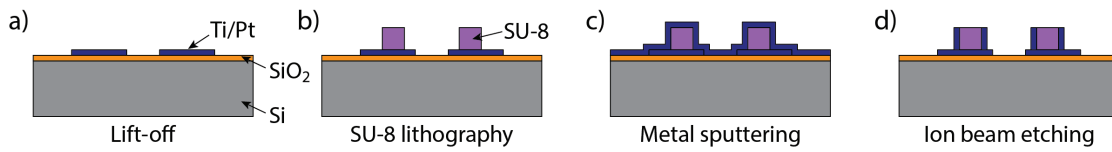
Figure 2.16 – Illustration of the fabrication process for free-standing pillar electrodes, with the metal lines patterned by lift-off. The process starts by patterning the titanium (Ti) and platinum (Pt) connection lines (a) and adding the 3D SU-8 structures on top of the connection lines (b). The electrodes are then uniformly sputter-coated in metal (c), and the excess metal on the horizontal surfaces is removed by dry etching (d).

setup rather than a four-point one, so that the y-intercept indicates the resistance of the cable connections. In the case of the vertical electrodes, we found an additional offset, which can be explained by the connection resistance of the planar and vertical metal layers. The values from both measurements match well.

Finally, to verify the exposure of the vertical electrodes to their surroundings, we performed AC measurements in dry and wet conditions. For this purpose, we realized 3D electrodes of variable lengths (L) contained inside microfluidic channels (Fig. 2.19.a). The height of the channel and the electrodes was $50\,\mu m$, the distance of two facing electrodes was either
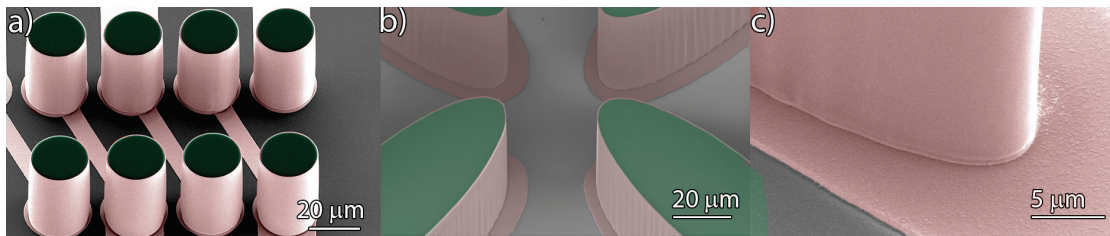
Figure 2.17 – SEM images of $50\,\mu m$ high metal-coated SU-8 structures with the connection lines patterned by lift-off processing. The lift-off process grants high patterning resolution for the planar lines (a) and high alignment accuracy between planar and vertical structures (b). A close-up of the bottom of the vertical electrodes suggests a continuous metal film and connection between planar and vertical layers.

a)

b)
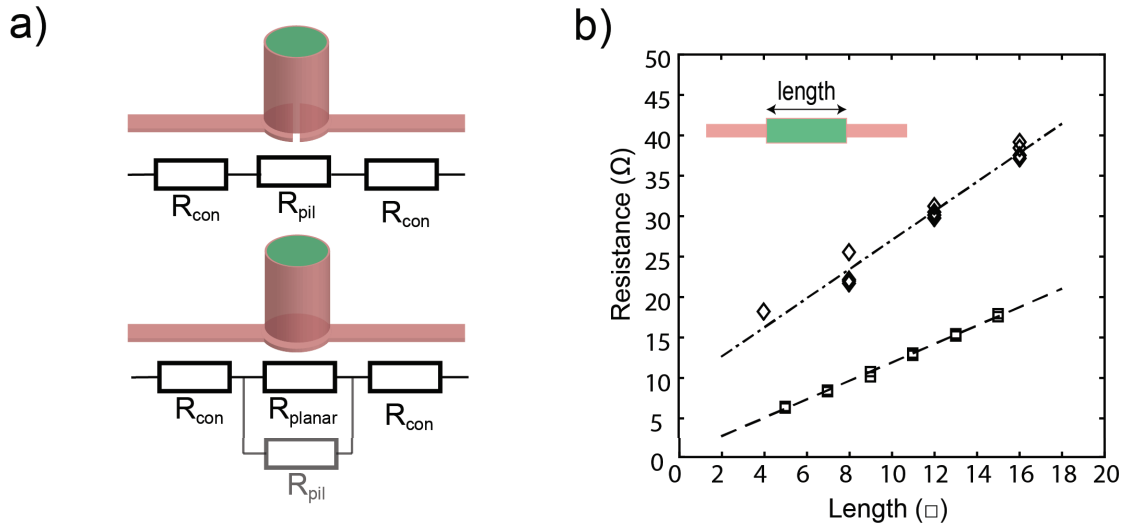
Figure 2.18 – DC measurements to extract the sheet resistance of the planar and vertical double layers. a) cartoon of the test structures and the equivalent electrical circuit. b) Measurement of the resistance of different structures plotted against the length in □. The lines indicate the best linear fit in both cases.

$100\,\mu m$ or $200\,\mu m$, and the electrodes extruded into the channel by a distance of $d' = 15\,\mu m$. We extracted the frequency spectrum of the electrodes and fitted them with the electrical circuit, shown in Fig. 2.19.b to extract the double-layer capacitance. By plotting the measured capacitance against the electrode surface, we confirmed a linear behavior and found an average double-layer capacitance of $2.7 \pm 0.54\,\mu F/cm^2$. This value is a good indication for the double-layer capacitance. The low standard deviation suggests homogeneous exposure of the electrode surface.

2.2.5   Process optimization, options, and variations

However, so far, we only discussed the working process and neglected the different optimization steps. There were several critical problems that had to be solved to establish this fabrication process, with the two main concerns being the sidewall angle and the adhesion on the metal of the SU-8 structures.

Electrode design

In addition to properly covering the electrode sidewalls with metal, it is also important to expose the metal to its surrounding and connect the vertical layer with the planar one at the bottom. We showed above that the combination of sputter coating and oxygen-plasma activation enables uniform coverage of the SU-8 scaffolds. Nevertheless, it is important to control and monitor the sidewall angle of the SU-8 structures. When this angle is slightly bigger than 90°, the bottom part of the electrodes is exposed during the dry etching of the
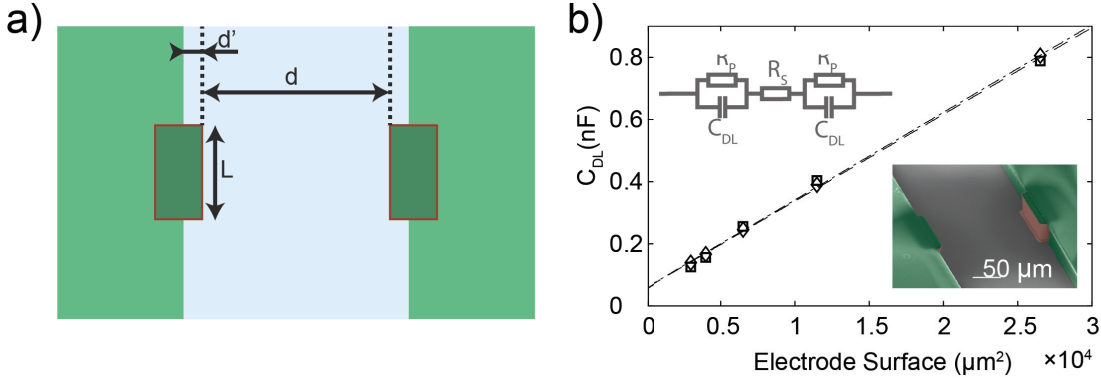
Figure 2.19 – AC measurements to verify the proper sidewall exposure of the vertical electrodes. a) Illustration of the test structures integrated in a microfluidic channel. b) Extracted double-layer capacitance for the different electrodes. The values were obtained by fitting with the equivalent circuit indicated. The inset shows one of the test structures that was characterized.

metal layer. Since we do not use any etch mask, this would lead to the disconnection of the planar and vertical metal layers. There are different fabrication parameters that can influence the sidewall angle of the SU-8 structures [164, 165], and a well-controlled fabrication process is mandatory. However, we found that when SU-8 is etched with an isotropic oxygen plasma receipt, the etching outcome is not homogeneous, and the top of the structures resists the plasma better than the middle or the bottom parts. A possible explanation for this is that during the exposure of the structures, the top part of the structures gets a slightly higher dose than the bottom part. While this might be seen as a problem, it also provides an opportunity to correct the shape of the SU-8 pillars by choosing the right oxygen plasma time and power. The resulting crown on top of the structures can then be used to protect the connection between the planar and vertical metal layers (Fig. 2.20).

Adhesion of the SU-8 scaffolds on the connection lines

Another issue we had to optimize was the adhesion of the SU-8 structures on the metal connection lines. Although, we used a double metal layer consisting of Ti and Pt in the beginning, the adhesion of the SU-8 on the Pt layer was poor and the pillars did not stay on the pads. For this reason, we tried to pattern the metal pads with donuts shapes. The main idea was that, although the pillars did not adhere well on the Pt, there would be SiO_2 in the center, where the pillars could adhere. Although this strategy worked and the pillars stayed on the surface, the problem was that they did not adhere well on the Pt and were loose on the borders. As a result, we did not establish a connection between the planar and the vertical metal layers. In addition, the SU-8 structures were wider on the bottom, what might be explained by interference of the UV-light on the different material layers. For this reason, we decided to use full metal pads with a triple metal layer of Ti/Pt/Ti, in which the top Ti layer serves as an adhesion layer for the SU-8. This strategy works well, as Ti provides better adhesion for the SU-8 than does Pt [166, 167].
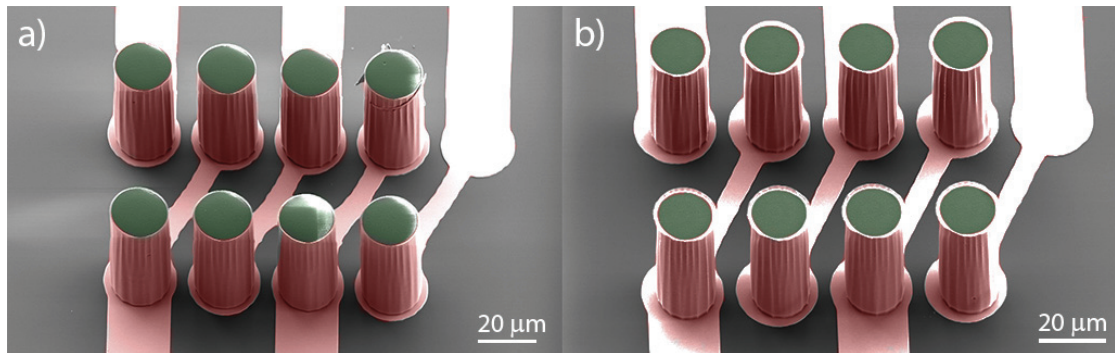
Figure 2.20 – Different SU-8 pillars (green) were treated in oxygen plasma and covered in metal (red). The SU-8 etching was not uniform resulting in the formation of a crown-shaped extension on top of the pillars. Such features can be employed to protect the connection between the planar and vertical metal layer from being etched in a later step. Although the effect was only slight for a short plasma time (a, 1 min.), a longer etching time (b, 3 min) led to a more prominent correction of the shape.

2.2.6 Comparison of the different fabrication processes for 3D electrodes

Finally, we conclude this part of the chapter, by comparing the established fabrication processes with the existing ones. First, we developed a process based on metal-coated silicon structures. Although this process allows to fabricate 3D electrodes, it has several drawbacks. Limitations resulted from the etching step, it requires non-standard equipment (spray coating), is limited in substrates, and the fabrication cost is high.

For this reason, we developed another fabrication cost that is based on the homogenous coating of SU-8. SU-8 has the advantages that, in a single lithographic step, structures of up to $200\,\mu m$ are possible; it allows for aspect ratios of 20:1 and above all; it has good chemical stability; and can be processed on various substrates [168, 164, 169, 170]. The latter is important, as it is possible to use insulating substrates, making abundant the need for insulation.

We could achieve sufficient adhesion of the metal layer by hard-baking and oxygen-plasma treatment. We first patterned the connection lines by dry-film resist. The advantage of such resists is that they can be applied with a simple office laminator, and the films guarantee a good homogeneity of thickness [171]. However, the main disadvantage of dry-film resists is their low resolution, which is in the order of the film thickness [172]. In addition, as mentioned above, we needed to pattern lateral overlaps on the 3D pillars to achieve sufficient adhesion of the film on the 3D topography. For this reason, the dry-film approach is good in cases in which low patterning resolution is sufficient.

However, when higher patterning resolution is needed, the SU-8 approaches makes it possible to first structure the metal layers on the flat substrate and then pattern the SU-8 on top of the metal connection lines. Beside the high patterning-resolution, this process also grants high alignment accuracy for planar and vertical features.

While so far we only describe the established processes, the question is how they compare to other existing ones? As illustrated in the beginning, electroplating is a time-consuming process that is hard to control. A great deal of experience is needed to achieve good results, and only limited electrode heights are generally possible. Furthermore, it is expensive, and the surface quality might not be the best and design restrictions result.

The C-MEMS process is a simple way to fabricate 3D electrodes and requires only two SU-8 steps (one for the connection lines and one for the 3D electrodes) plus a pyrolysis step. However, this last step imposes a lot of restrictions. First, the substrate is heated up to $700°C$ and special furnaces are required. Furthermore, the structures shrink during the pyrolysis, leading to a widening of electrode gaps [152]. However, the biggest drawback of this process is the achieved conductivity that is four orders of magnitude lower than the ones of metals [154].

Overall, we see that especially the SU-8 based processes is a very interesting alternative, as it allows to fabricate metal grade electrodes with high patterning precision. Furthermore, the fabrication cost for this process is rather low, although in the case of lift-off patterning, two metal deposition steps are required. Table 2.2 sums up the comparison of the different fabrication processes.

Table 2.2 – Comparison of the different fabrication variations, including their advantages, disadvantages, and limitations.

	Spray coating	Dry film	Lift-off	Electroplating	C-MEMS
Patterning resolution	$20\,\mu m$	$50\,\mu m$	$1\,\mu m$	$1\,\mu m$[1]	$1\,\mu m$[2]
Process difficulty	+++	+	++	+++	+
Cost	\$\$\$	\$	\$\$	\$\$\$	\$
Aspect-ratio	20:1	20:1	20:1	15:1[3]	20:1[4]
Minimal Gap	$20\,\mu m$	$40\,\mu m$	$10\,\mu m$	$20\,\mu m$	$40\,\mu m$
Conductivity	+++	+++	+++	+++	+

[1] Patterning resolution of SU-8 mold
[2] Patterning resolution of SU-8 precursor before pyrolysis
[3] Assuming isotropic shrinkage of the aspect ratio is the same as SU-8
[4] see [173]

2.3 Electrorotation experiments with 3D electrodes

We used such 3D electrorotation chips to perform experiments on neuroblastoma cells (BE(2)-M17 (ATCC® CRL-2267™)), obtained from the Lashuel laboratory (EPFL) and purchased from ATCC, USA. The cells were cultured in DMEM:F12(1:1) medium, supplemented with 10% FBS, $100\,\mu g/\mu l$ penicillin/streptomycin (Life Technologies). Prior to ROT experiments, the cells were washed with PBS (Life Technologies) and harvested by treatment with trypsin (0.025%, Thermofisher Switzerland). The cells were then removed from the culture plate and re-suspended in culture medium. Finally, the cells were spun down at 1200 rpm for 5 min. in a centrifuge (Hettich Universal 320R) and were washed twice and re-suspended in a special DEP
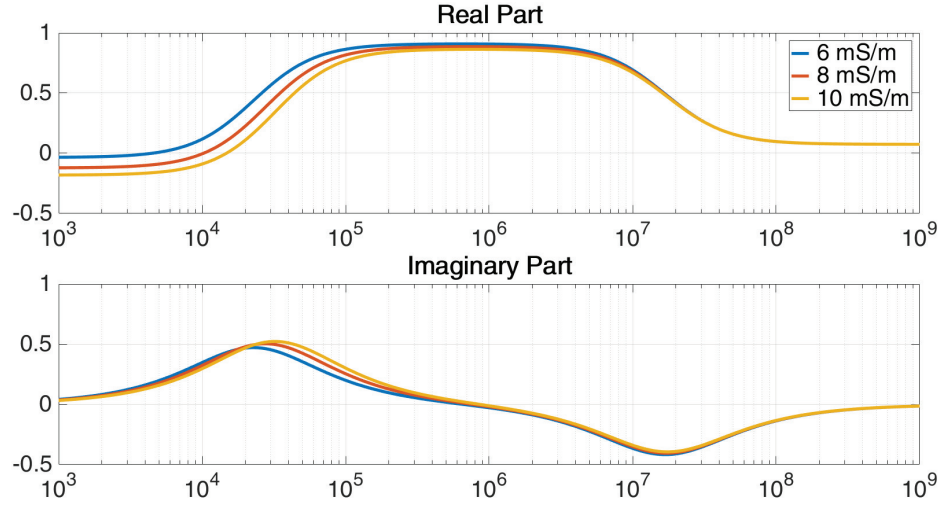
Figure 2.21 – Simulation of the real and imaginary part of the Clausius-Mossotti factor for different medium conductivities. The spectra were obtained by assuming the following parameters: membrane capacity $\left(C_m = 16.95 \, mF/m^2\right)$, membrane conductance $\left(G_m = 800 \, S/m^2\right)$, cell radius $\left(R = 6.9 \, \mu m\right)$, cell permittivity ($\epsilon_c = 100$), cell conductance ($\sigma_c = 0.23 \, S/m$).

buffer consisting of a 300 mM sucrose solution. The conductivity of the buffer was adjusted with PBS (1x), while the conductivity was measured on a conductivity meter (Eutec CON 700). In addition, we simulated a reference spectrum, which indicates a transition from pDEP to nDEP in the lower frequency range and we would expect a negative rotation peak around $20 - 30 \, kHz$ (Fig. 2.21.

The experiments were performed on ROT chips with bone-shaped electrodes [110, 67] with an inter-electrode spacing of $400 \, \mu m$. The medium containing the cells was spotted on top of the chips and covered by a thin microscope slide. The experiments were performed at 29 different frequencies, logarithmically distributed between $10 \, kHz$ and $40 \, MHz$. We used signals with an amplitude of $4 \, V$ to prevent systematic experimentation errors the frequencies were applied in a random order. For each frequency, 19 frames were acquired at a rate of five frames per second.

The experiments show a negative rotation peak in the expected frequency range, and the frequency peak shifted with the medium conductivity (Fig. 2.22). However, a shift in the rotation rate was also seen for the different conductivities, especially for the low medium conductivity. One possible explanation for this observation is the evaporation of the medium, as the evaporation of the water would lead to an increase in higher salt concentrations. The experimental data show the same trend as the one that we observed from the theoretical calculations (Fig. 2.21). Furthermore, this also explains why we see less drift for the higher conductivities, as changes in medium conductivity have a lower impact on the rotation spectrum. In addition, there might be an additional effect as the medium evaporation rate might change with increasing salt concentration [174].
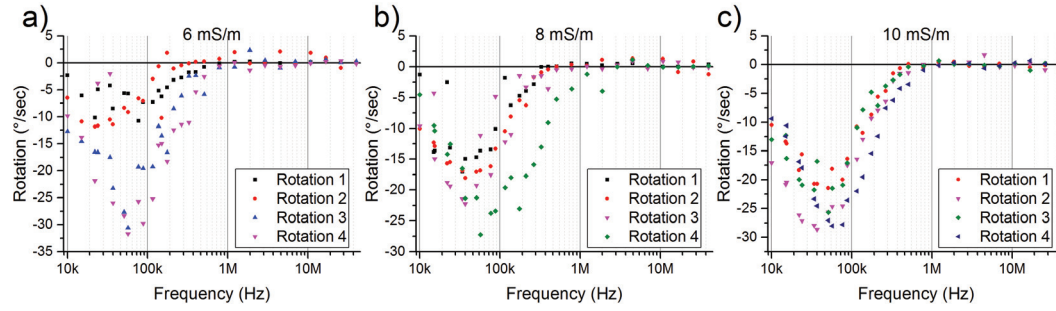
Figure 2.22 – Electrorotation spectra of single M17 neuroblastoma cells in sucrose medium with the medium conductivity adjusted to 6 mS/m (a), 8 mS/m (b) and 10 mS/m (c). The results show a prominent negative rotation peak in the lower frequency range, while a drift in rotation magnitude and peak frequency is observable. The drift is more prominent for low medium conductivity (a) than for higher ones (c).

Finally, the comparison of the theoretical model (Fig. 2.21) with the experimental data (Fig. 2.22) shows that we have an anti-field rotation peak as we would expect, however, the theoretical peak is lower (between 10 and 30 kHz) than the experimental one (between 40 and 90 kHz). Another problem that can be seen from the experimental plots is that there is no high frequency peak observable. In general, there are only few spectra that show some co-field rotation. Although we were not able to fully solve this issue in the framework of this thesis, however, there are different explanations for this phenomenon. In our understanding, the problem comes from signal attenuation caused by parasitic currents at higher frequencies. These parasitics can have different origins, such as the connection and cables, a mismatch between output resistances, and parasitic currents on the chip, e.g. through the substrate. For this reason, we used short and shielded cables with standard connectors and set the output resistance accordingly. Furthermore, we used a passivation layer on the silicon substrate. However, as the problem persisted, it might be that the SiO_2 layer is short circuited at the higher frequencies and thus it might be interesting to test chips that are fabricated on glass supports. Finally, if the problem still persists, another solution could be to re-design the chip-holder with a PCB that contains active amplification electronics. This would allow to take the load of the signal generator and to control the signal amplitude right before the connection with the chip. Nevertheless, for this approach to work, the electronic components should be chosen with care, in order to ensure that they suit the targeted frequency range.

Another issue that was observed was that different cell rotation speeds were observed for different cells. This can be explained by the variation of the ROT torque throughout the chamber. It would be possible to overcome this problem by adjusting the rotation spectra with the mapped field strength inside the chamber [175] or to use electrical tweezers to simultaneously trap and rotate the cells in the center of the electrodes. Nevertheless, in general during the fitting procedure, the amplitude of the rotation spectrum is not taken into account.
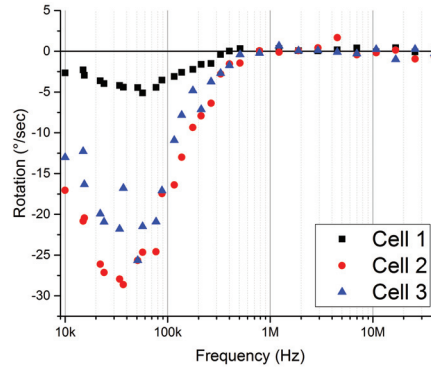
Figure 2.23 – Three ROT spectra of a single M17 cells acquired simultaneously. While the three spectra have a similar shape, it can be seen that the amplitude of the rotation speed differs for the three cells, due to their different position inside the electrorotation chamber.

We finally used Origin (Origin labs) to fit the obtained spectra with the single shell model. Due to the above-mentioned problems, we neglected the high frequencies (above 1 MHz) and thus did not fit for the interior parameters of the cell. Furthermore, we fixed the cell membrane conductance as it in general has a low impact on the rotation spectrum and thus is hard to extract. The fitted membrane capacitances for the different cells and the different medium conductivities are summarized in Table 2.3. The results show that although the different problems with the rotation experiments, we managed to extract the membrane capacitance for different cells at different medium conductivity. Furthermore, it can be seen that the results are in general in good agreement, with low standard errors.

Table 2.3 – The extracted cell membrane capacitance in mF/m^2 that were extracted for the different ROT experiments at the different medium conductivities.

Medium conductivity:	10 mS	8 mS	6 mS
	9.44 ± 1.51	12.16 ± 2.04	9.22 ± 1.28
	11.18 ± 0.57	12.26 ± 0.60	21.17 ± 3.44
	10.2 ± 0.61	23.14 ± 2.05	16.04 ± 1.08
	13.19 ± 0.41	13.31 ± 1.85	10.27 ± 0.82
	12.12 ± 0.91	5.36 ± 0.30	8.76 ± 0.74
	7.63 ± 0.26	7.34 ± 1.17	6.7 ± 1.01
	9.21 ± 1.65		7.1 ± 1.03
	9.44 ± 1.51		
Average	10.30 ± 1.06	12.26 ± 1.51	11.32 ± 1.60
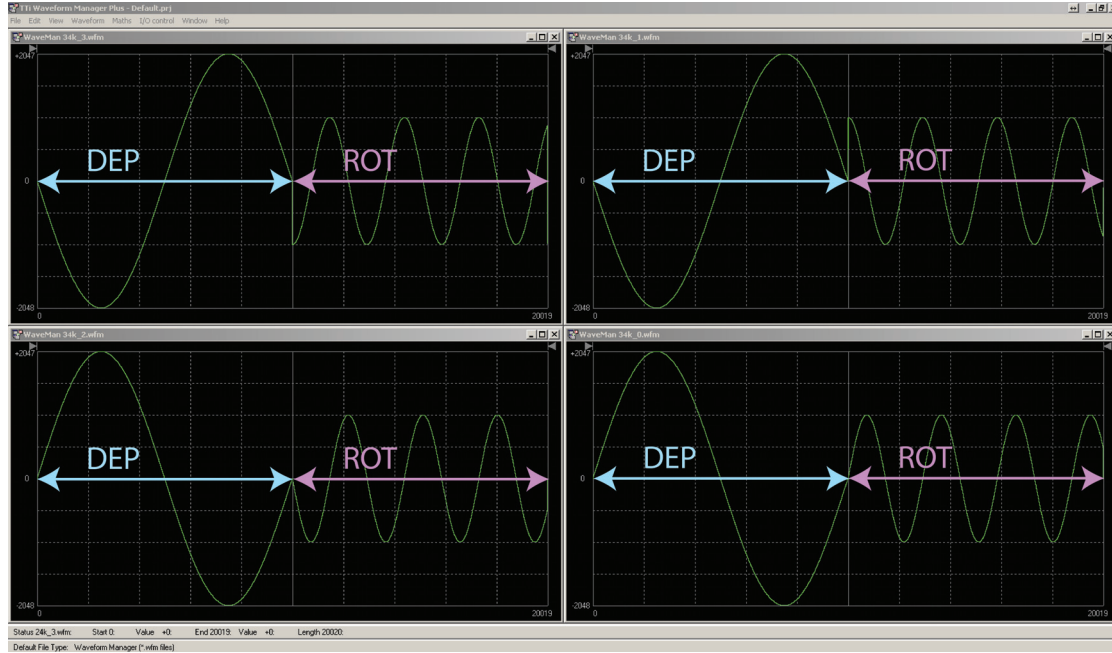
Figure 2.24 – Screenshot of the design software for the electrical tweezers. Four signals were designed, each consisting of a first part to induce nDEP, and a second for ROT. The phase shifts between neighboring electrodes are 180° and 90° for DEP and ROT experiments.

2.3.1   Electrical tweezers with 3D electrodes

We designed the electrical tweezers as arbitrary wave signals with a DEP and a ROT part in the Waveman software provided by TTi. The DEP signals were designed with a 180° phase shift at a frequency of $10\,kHz$, while the ROT signals had a 90° phase shift and were designed for each frequency of the ROT spectrum (Fig. 2.24). A short break of $10\,\mu s$ between the two parts gave the dipole time to relax, in order to avoid interferences between the two signals [134]. We designed different sets of signals consisting of 30 frequencies with a logarithmic distribution in the range of $10\,kHz$ and $40\,MHz$, with each set having its own DEP:ROT amplitude ratio (1:1, 2:1, and 4:1). The higher amplitude of the DEP signal ensured that the trapping forces overcame destabilizing forces to reach stable particle trapping.

The experiments were performed with A549 (ATCC® CCL-185™)) lung-cancer cells, obtained from the Forro laboratory (EPFL). The cells were cultured in DMEM medium, supplemented with 10% FBS $100\,\mu g/\mu l$ streptomycin and $100\,U/ml$ penicilin (Life Technologies). Prior to electrorotation experiments, the cells were washed with PBS (Life Technologies) and harvested by treatment with trypsin (0.025%, Thermofisher Switzerland). The cells were then removed from the culture plate and re-suspended in culture medium. Finally, the cells were spun down at 1200 rpm for 5 min. in a centrifuge (Hettich Universal 320R), washed twice with DEP buffer and finally they were resuspended in the DEP buffer. The buffer preparation was the same as described above. We chose a medium conductivity of $10\,mS/m$ to decrease heating effects, get nDEP for the tweezers and keep the rotation peak at the lower end of the spectrum. The

cells were suspended at $100'000\,cells/ml$ and spotted on top of the electrodes. However, this procedure did not produce very high control over the amount of cells inside the rotation chamber. We found that the combination of DEP and ROT worked well (Fig. 2.25), but the observation of cell rotation was only possible so long as only a few cells were in the rotation chamber (Fig. 2.25.a1-a4). The presence of a larger number of cells in the chamber, resulted in their clustering in the center, making it impossible to track single cells or extract their rotation speed (Fig. 2.25.b1-b4). While we did observe that cells were pushed towards the center of the electrodes, we did not observe that all of the cells were centered and there might be different possibilities for this. First, we chose a medium conductivity and frequency that showed nDEP when modeled (Fig. 2.21). However, the nDEP was very low and the frequency that we chose to work with (10 kHz) was very close to the theoretical cross-over frequency (about 15 kHz). For this reason, some slight changes in cell properties might have undergone pDEP instead of nDEP. Furthermore, as we worked with adherent cells, the cells tended to adhere on the chip However, in order to avoid such problems, a higher medium conductivity could be chosen, to ensure nDEP for all the cells. Finally, we did not investigate in details on the limit of cells that can be observed in parallel, however, the maximum number of cells that we managed to image, while still being able to extract from, was a total of 4 cells. However, it would be possible to increase this number, by adjusting the amplitude ratio of the DEP and ROT signal to ensure a stable balance between the forces generated by each signal. However, with the final goal of having a single cell in a small quadrupole, we did not further investigate into this direction.

2.4 Conclusion

We started this chapter with the interest in 3D electrodes for electrorotation experiments, and we discussed the need for new microfabrication processes for 3D electrodes. For this reason, we developed different microfabrication processes based on the homogenous coating of insulated scaffolds with metal layers. While a first process based on the etching of silicon structures for the 3D electrodes still has certain limitations, we targeted these issues by developing a new fabrication process based on additive manufacturing, enabled by SU-8 photolithography. This process is unique in its characteristics, as it grants high design flexibility at low fabrication cost, while the 3D electrodes are built out of metal surfaces that grant high conductivity. Furthermore, the process is compatible with different substrates. In a later chapter, we will explain how it is possible to achieve high-density 3D electrode arrays by having multiple levels of connection layers. We would also like to point out that the process is fully CMOS-compatible and would allow to combine the two technologies.

For what concerns the quality of the electrodes, we verified by electrical measurements the proper connection of the planar and vertical metal layer and we demonstrated proper exposure of the sidewall electrodes. Furthermore, we characterized different cell types by ROT experiments and were able to extract the cell membrane capacitance of single cells that was consistent for different cells of the same population. However, we also saw different problems
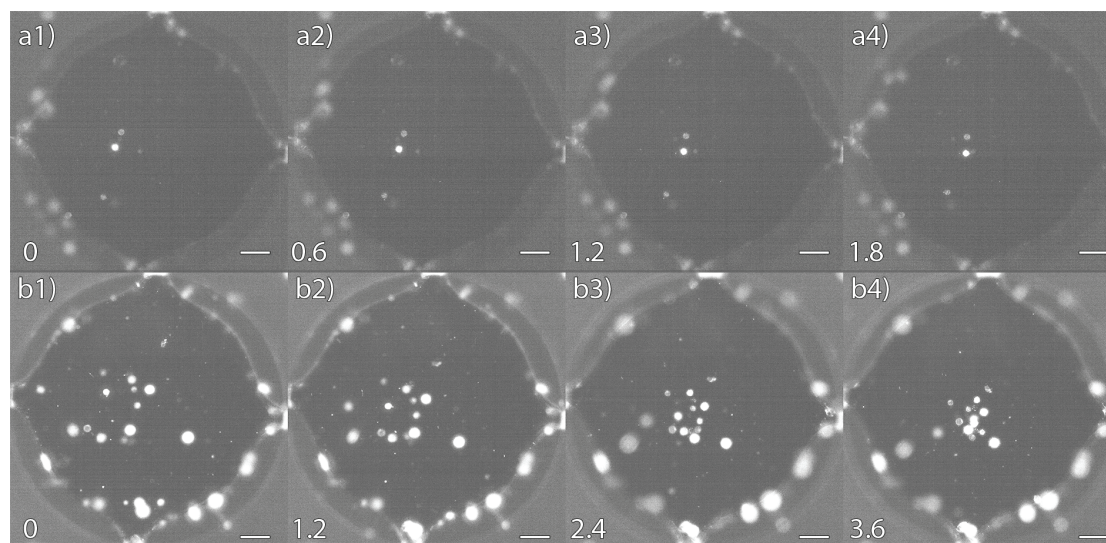
Figure 2.25 – The picture shows two different sequences of cells being pushed to the center, while they rotate. The electrodes are indicated in green and the cells were stained with a fluorescent membrane stain (DiI). a1-4) At low cell density, the cells still keep sufficient distance to be tracked, while they do not rotate around the cell cluster. b1-b4) At higher cell density, the cells are pushed together and cluster up. It is almost impossible to extract the speed of rotation of a single cell. The cell cluster itself rotates. Time is indicated at the bottom left of the images in seconds, and the scale bars correspond to $50\,\mu m$.

that should be addressed, such as medium evaporation and cell clustering. Both of them can be addressed through the use of microfluidic technologies, as we will explain in the next chapter.

"The real measure of success is the number of experiments that can be crowded into 24 hours"

—Thomas Alva Edison

3

A microfluidic system for automated, single-cell electrorotation

In the previous chapter, we discussed the advantages of using small 3D electrodes for a ROT system. We combined the 3D electrodes with microfluidics to provide a closed fluidic system and single-cell handling through the precise control of injection volumes. In this chapter, we will present the integration technology to obtain 3D electrodes in microfluidic channels. We first provide simulations of the 3D electrodes inside the microfluidic channels in support of the explaination of the basic working principle and then cover the realization of such channels along with the discussion of the packaging challenges. We will extensively cover the integration of all the functionality in a single interface that enables fully automated extraction of a complete electrorotation spectrum. In particular, we will discuss the development of novel algorithms based on the pattern matching approach that allows for accurate extraction of the cell rotation speed. Finally, we will report on experiments that were performed to position single cells inside the electrorotation chamber.

3.1   Integration of 3D electrodes into microfluidic channels

The goal of this thesis was to integrate the 3D electrodes directly in the sidewalls of the microfluidic channels, in order to avoid cell deflection around the electrodes. In the first place, we planned to use a bone-shaped design, in order to achieve good torque linearity and reduce DEP forces [110]. However, the main problem with this design was the combination of such 3D electrodes with microfluidic channels. Although the initial idea was to bring the particles into
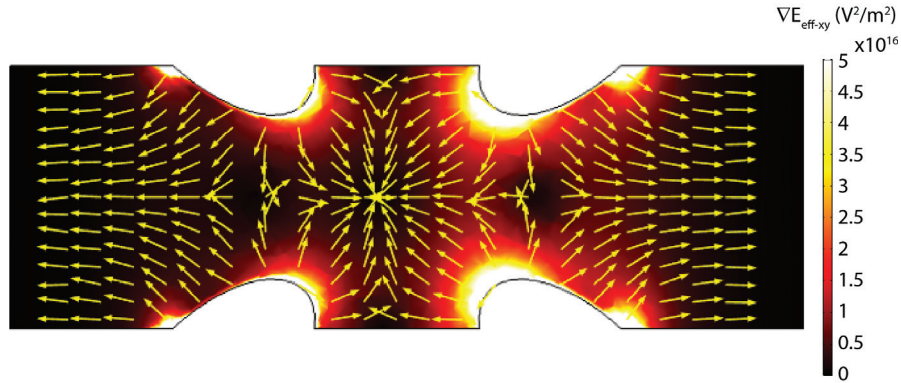
Figure 3.1 – Simulation of the DEP forces inside a quadrupolar trap with parabolic electrodes. The cells would be injected from the left side of and the two earlier electrodes are energized with a lower DEP signal ($3\,V$) to achieve a lower entry barrier, while the output barrier was raised by applying a higher amplitude ($5\,V$). Furthermore, it can be seen that the asymmetric shape of the electrodes allows to achieve a lower field gradient on the electrode side away from the center.

the chamber through the gaps in between the electrodes, this lead to very high flow speeds in these gaps and consequently limited control on the cell positioning. Furthermore, this approach did not allow to obtain chambers with size comparable to single cells, as otherwise the microfluidic accesses would have been too small for cells to pass.

For this reason, we opted for a parabolic electrode shape, as this design allows to achieve asymmetric DEP barriers, as the field gradient that the particle experiences to leave the trap is steeper than the one that the particle has to climb upon entering into the trap (Fig. 3.1).

In what follows, we will describe the different elements that are integrated on the chip and that were combined to achieve the different functions. We already discussed the advantages of 3D electrodes for ROT experiments in the previous chapter and we will now focus on the other parts of the system. The electrode quadrupole was meant to be used not only for cell rotation, but also to position and trap the cells inside the microfluidic channel. We developed a side channel to reduce the flow speed to make it compatible with DEP trapping. In order to drive cells in the channel where the quadrupole was present (rotation channel), we developed a special DEP element that allows to deviate the cells to the thinner channel. Furthermore, we developed a focusing element, that centers the cells inside the channel, to ensure a safe entry into the quadrupolar trap. In what follows, we will give an overview of these different elements and we will describe their functioning.

3.1.1 Simulation of DEP focusing and trapping in microfluidic channels

We used finite element calculations to calculate the particle trajectories inside our microfluidic device. For this purpose, we combined the fluid flow, electrostatics, and particle-tracing mod-

ule from Comsol Multiphysics and performed the simulations with the parameters indicated in Annex A.2. In a nutshell, we solved the electrostatics module with a frequency domain solver and the fluid-flow module with a stationary solver and plugged the solutions into the particle tracing module to calculate the particle trajectories based on resulting gravitational, DEP, and fluidic drag forces.

The trapping module was designed with parabolic electrodes and a small channel with a width of $40\,\mu m$ that brings the particle into the trap. The fluid flow is actuated by an input pressure of $5\,mbar$ and the electrodes are energized by signals of $1.5\,V$ on the first set of electrodes and $5\,V$ on the second set. We chose different voltages on the two sets of electrodes, in order to achieve different strengths in the DEP barriers that the particles have to overcome. The lower voltage of the input electrodes helps to center the particle and provide stability form the side. We found that from our simulation the pressure and voltage ranges were suitable to achieve particle trapping (Fig. 3.2) and we saw that the entry barrier was low enough for the particles to enter into the trap and the output barrier was high enough to retain the particles inside the trap. Furthermore, we saw that the particles were centered in the x-y plane, why they took up the shape of the flow profile in the y-z plane (Fig. 3.2.

The next step was to design an element to center the particles inside the microfluidic channel. For this reason, we designed an element consisting of circular 3D electrodes that are integrated inside the sidewalls of the microfluidic channel. The idea was to connect the electrodes with Π-shifted signals, in order to create high field regions on the side of the channels, that would under nDEP conditions repel the cells from the sidewalls and center them (Fig. 3.3). However, one of the question was to investigate on the effect of connection lines that are patterned on the bottom of the microfluidic channels and if we would have to insulate them or not. For this reason, we simulated a device with a $100\,\mu m$ wide channel and different widths of the connection lines (5, 10, 15 or $20\,\mu m$) and observed the particle trajectories (Fig. 3.3). These simulations showed us a proper working of the centering. However, we also found particle levitation in all of the cases, due to the presence of the connection lines (Fig. 3.4). Nevertheless, the cell levitation was different for the different widths (Fig. 3.4) and it was the lowest in the case of the $5\,\mu m$ wide connection lines,and the particles moved at a higher speed (Fig. 3.4.a) than in the case of 10, 15 or $20\,\mu m$ (Fig. 3.4.b, c, and d). For this reason, we decided to design the centering element as short as possible and use it only in the $40\mu m$ wide rotation channel (Fig. 3.5).

Finally, we needed one further element that helps to deflect the particles in the microfluidic channel and prevents them from escaping through the side channel that is used to reduce the flow speed. The idea was to place 3D microelectrodes into this junction and to energize the electrodes in order to create DEP barriers in between the electrodes that would retain the cells from passing in between the pillars. This time, we simulated the full chip with the three different elements and studied the behavior of the particles inside the microchannel. Furthermore, we reproduced the electronic connection schematic as on the real chips, we were limited to only four different electrical signals that we could apply to the chips. For this
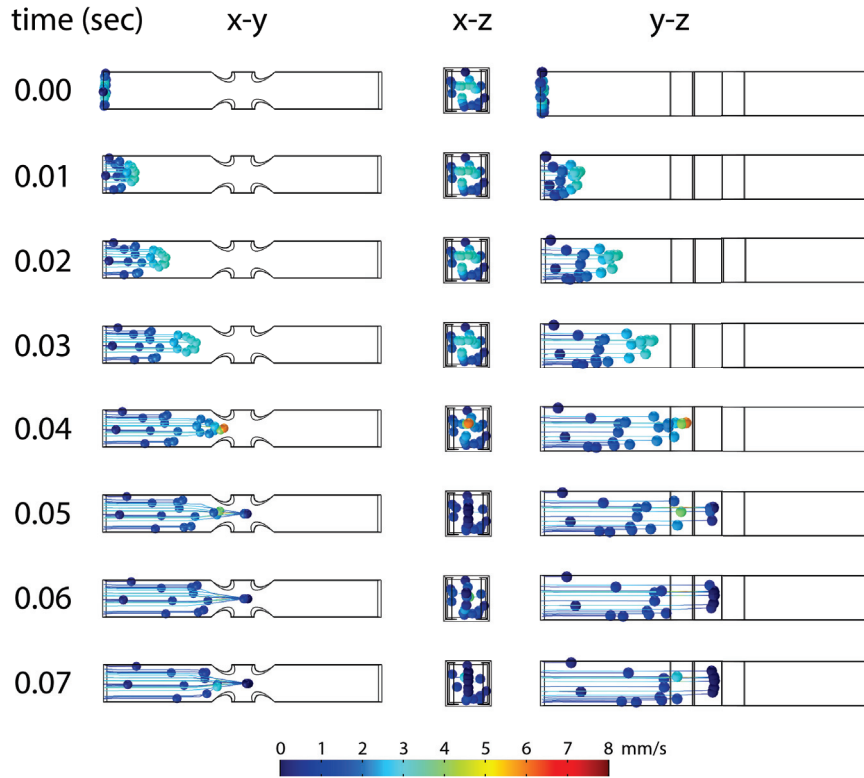
Figure 3.2 – Simulation of the particle-trapping element in three different cut planes, over a time course of 0.07 *sec*. Most of the particles arrive after a short time in the trapping element and are retained. At the same time, they are focused in the center of the chamber, while the particles take up the shape of the parabolic flow profile (y-z plane).

reason, we applied signals with the same amplitude to the deflection and centering element, as well as to the two first electrodes of the trapping element, as on the real device they would all be connected together, while the second two electrodes of the trapping element had a higher signal amplitude. Due to this restriction in the connection scheme, we had to compromise between complete particle deflection and the particles being able to enter the trap (Fig. 3.6). However, as the particles that could not be withheld managed to escape at the beginning of the deflection element (Fig. 3.7), we decided to extend the 3D electrodes in our final design further down along the microfluidic channel to push the cells into the center of the channel before they reach the intersection.
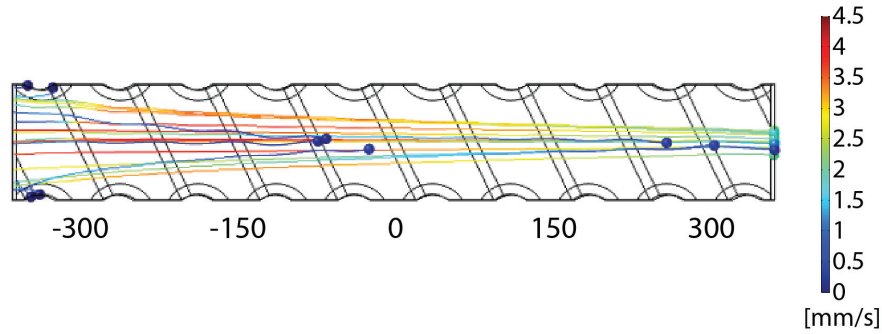
Figure 3.3 – Top view of a particle-focusing element based on 3D electrodes integrated into channel sidewalls. Opposite electrical signals are applied to neighboring electrodes, resulting in DEP forces pushing the particles to the center of the microfluidic channel.

3.1.2 Integration of 3D electrodes into microfluidic channels

The next step was then to realize such microfluidic channels and to develop the microfabrication technology required for it. The main objectives for us were to realize channels with the same height as the 3D electrodes and to design chips that allow us to use high NA-lenses for imaging. Such lenses are mainly interesting as they provide excellent image quality, however, they generally come at short working distances (in our case $280\,\mu m$) and at bulky sizes. For this reason, we decided to develop our own fabrication process that allows to realize the microfluidic accesses on the backside of the chips and that uses only a thin but rigid cover to seal the channel. The latter is the most important, as a thin but soft sealing might either break or lead to flow dumping and thus would not allow for precise microfluidic handling.

Nevertheless, the first step was to realize the microfluidic channels, which we did in a second SU-8 process (Fig. 3.8.a). This approach enables to reach matching heights between the electrodes and channels by applying the same process parameters in the two cases and no further process optimization is needed (Fig. 3.9.a). Nevertheless, the spin coating of the SU-8 for the microfluidic channel was done with the 3D electrodes already on the wafers and thus we added a relaxation step of $30\,min$ between the spin coating and the soft-bake, in order to let the resist relax. Another advantage of the SU-8 process is that polymerization is performed after the application of the resist, which enables the fabrication of both freestanding (Fig. 3.9.b) and sidewall-integrated (Fig. 3.9.a) electrodes.

Next, we had to fabricate the access holes for the microfluidics, which were etched through the full wafer. This was a major hurdle for this process, as it is hard to pattern an etch mask that is hard and uniform enough to resist the long etching procedures that are required to etch through a complete wafer. For this reason, we used a silicon shadow mask that was aligned to the wafer prior to etching and removed afterward [162] (Fig. 3.8.b). The mask was fixed with a special wax (Quick stick 135) that could be applied and removed by simple heating. The microfluidic accesses and the chip outlines were etched $300\,\mu m$ deep into the silicon substrate. After removal of the shadow mask, the holes were opened completely by grinding from the
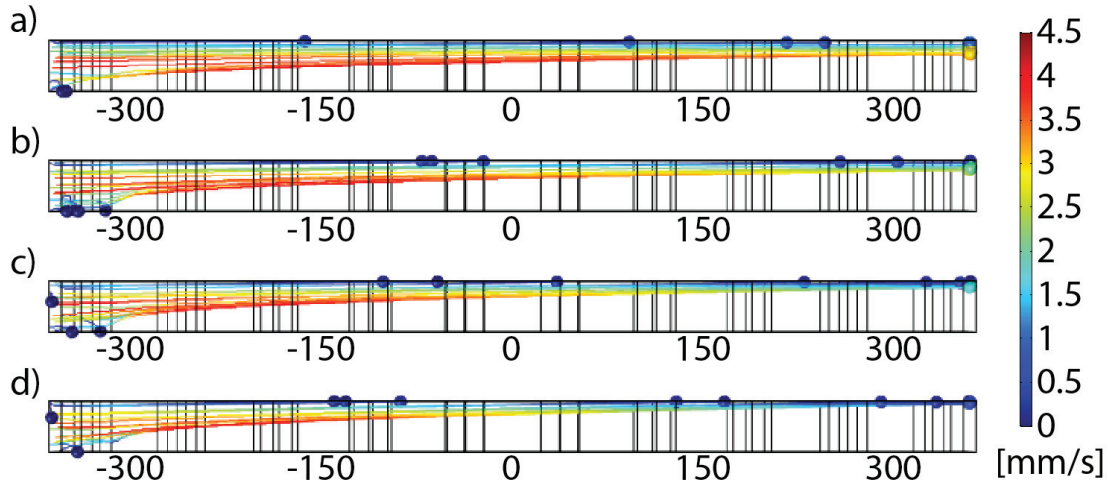
Figure 3.4 – Side view of particle levitation due to different widths of bottom connection lines. The different widths (a: $5\,\mu m$, b: $10\,\mu m$, c: $15\,\mu m$ d: $20\,\mu m$) of connection lines result in different levitation heights.

backside (Fig. 3.8.c). Finally, the chips were sealed by bonding a glass cover slip on top of the microfluidic structures (Fig. 3.8.d). Due to the thinness of the slides, we decided to use a chemical bonding procedure with an intermediate PDMS layer. The procedure consisted of applying a PDMS film on top of the glass coverslip, followed by oxygen-plasma activation and silanization. After the slide and the chips were combined and the two were baked together for 1 h at 150°C under the application of pressure (2 mbar, Fig. 3.8.d) [176]. This approach achieved a $150\,\mu m$ thin but rigid sealing of the microfluidic channels. Such thinness was compatible with our high-NA lens with a working distance of $280\,\mu m$. Furthermore, this procedure was well-sealed, as the PDMS layer accounted for small unevenness in the SU-8 layer and improved the bonding (Fig. 3.9.c). However, besides the evenness of the SU-8 layer, also the one of the PDMS layer is important, as we will discuss further down in section 3.1.2.

Different approaches for the microfluidic channels and accesses

We developed the above-described process in order to be able to work with high-NA lenses.

However, we will hereby discuss other possibilities to create the microfluidics, in cases where such lenses would not be needed. In this case, the simplest strategy is to mold the microfluidic channels in PDMS and bond it on top of the device. Such channels were successfully combined with 3D electrodes in a different project in our laboratory. However, this approach does not allow to integrate the electrodes into the channel sidewalls. Furthermore, for the technique to work, a rather thick PDMS block is required, to achieve sufficient stability and avoid collapsing of the channel. Finally, the alignment of the PDMS to the wafer has to be done by hand and thus only limited alignment accuracy can be achieved.
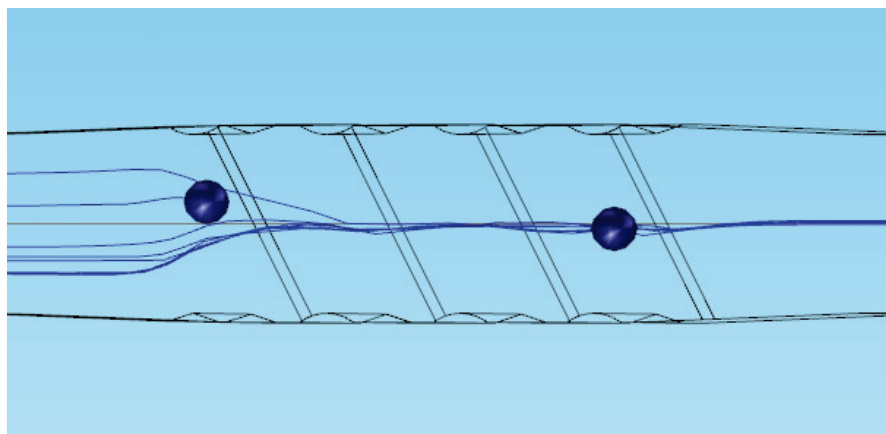
Figure 3.5 – The simulation of particle trajectories inside a focusing element integrated in the ROT channel. The side-wall integrated electrodes are energized to move the particles to the center of the channel.

Another possibility is a mixed approach of PDMS and SU-8 channels, where the microfluidic channels are developed in SU-8 and are sealed with a PDMS top layer. The advantage in this case is that the channels can be defined with high precision in SU-8 with the possibility to integrate the 3D electrodes. Then, the channels can be sealed with a thick PDMS layer with the already punched access holes. In this way, the alignment of PDMS and SU-8 can be done by hand, as it only requires to align the fluidic accesses on the chips with the ones in the PDMS. Furthermore, the tubing can be directly fixed in the PDMS and no connectors are needed. The advantage of this approach is that no backside accesses are needed, the channels can be defined and aligned with high precision, and the electrodes can be integrated into the sidewalls. However, the downside is that a thick PDMS layer is required to achieve sufficient stability and avoid collapsing of the microfluidic channel.

There are further possibilities, such as the use of double-side tape or the gluing of micromachined parts on top of the chips. However, in both cases the problem is the same as with the PDMS approach and the electrodes can not be integrated in the microchannels and the alignment accuracy is rather low.

Process optimization

Before moving on to the microfluidic integration, we will now spend some words on the optimization process and what had to go into the process to achieve this final goal. We will discuss the different steps and give an indication on what was tried and what worked and what didn't.

Optimization of the dry etching process for the backside microfluidic accesses   One of the major hurdles in the microfabrication process, was to find a way to etch through the whole
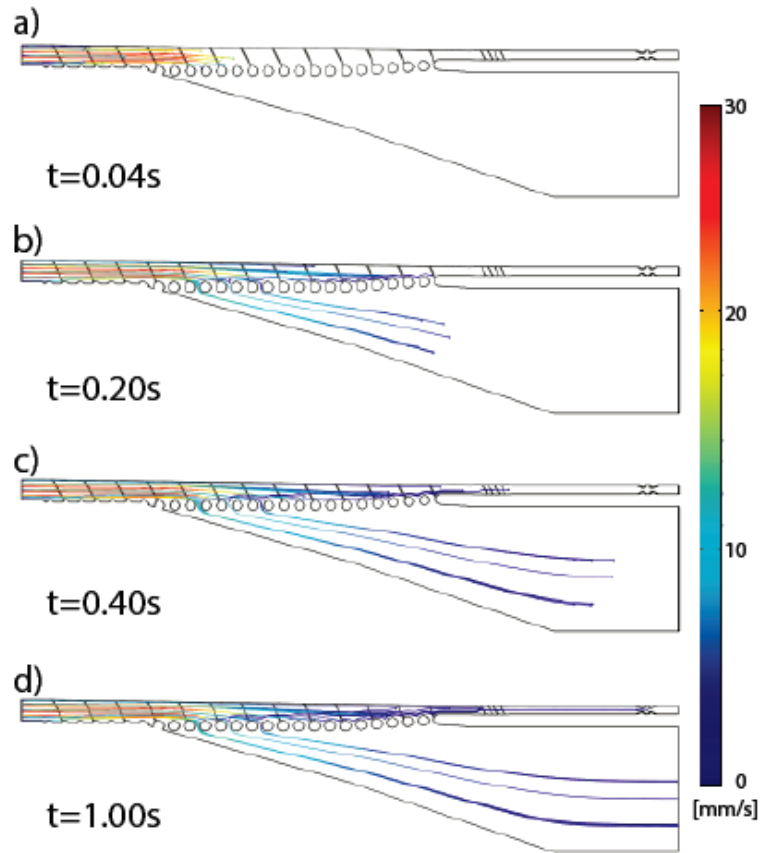
Figure 3.6 – Simulated particle trajectories in the full chip design. The particles are brought into the chip by hydrodynamic drag and deflected into the main ROT channel by DEP forces. The side channel is designed to achieve lower flow speeds in the ROT channel, to facilitate particle trapping in the quadrupole. The particle position is shown at different time points and the color indicates the particle speed in mm/s.

wafer. The base of the problem is to pattern a mask on top of the 3D structures, which would be resistant enough to withstand the long Bosch etching procedure that was required to etch the trenches into the silicon wafer, without attacking neither the metal, nor the SU-8. It is especially critical to not etch into the SU-8, as otherwise the etch chamber gets contaminated and the etching process will either slow down or not work at all. Furthermore, the high topography makes it almost impossible to use a standard photoresist.

Dry-film resist Such resists come as films with standard thicknesses ranging from 10 up to $100\,\mu m$. The advantage of such films is that they can be applied with a standard office laminator and lead to uniform thickness, as the latter is defined by the film and not by the application process. A detailed description of the fabrication process with all the equipment
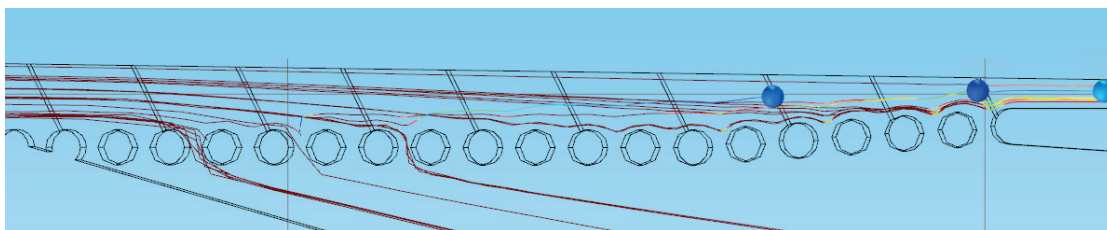
Figure 3.7 – Close-up image of particle-deflection elements showing the different particle trajectories.

| a) SU-8 lithography | b) Shadow mask + etching | c) Backside grinding | d) Bonding |
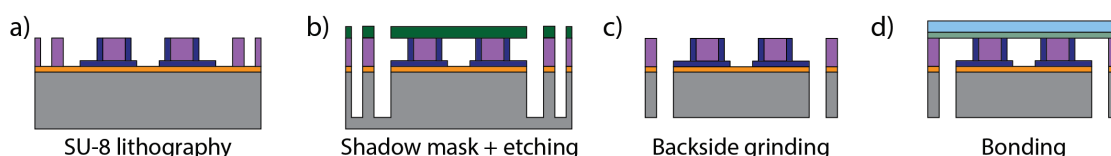
Figure 3.8 – Illustration of the microfabrication process for the microfluidic integration of 3D electrodes. a) First, the microfluidic channels are defined in an SU-8 process, b) A shadow mask is then applied and used to etch the fluidic accesses and chip outlines. c) After the shadow mask is removed, the trenches are opened by grinding from the backside, and the single chips are released. d) Finally, the channels are sealed by PDMS-mediated bonding of a thin glass coverslip on top of the microfluidic channels.

and the parameters can be found in the appendix (B.5.1). While the patterning and the etching were straightforward, the main problem with the films was their removal. In general such films can be removed in basic solutions, however, in our case, this was not possible. The film was attacked and dissolved, nevertheless, certain parts of the film resisted and stuck to the chip. Such residues were on one side problematic for the sealing of the chips, but also clogged the microfluidic channels, so that the chips were not usable. Besides longer treatments with stripper, we also tried harsher treatments with NaOH up to 1 M concentration for several hours. However, this did not improve the situation or dissolve the resting parts on the surface. The only good outcome from these experiments, were that we knew that the 3D electrodes can resist such harsh treatments.
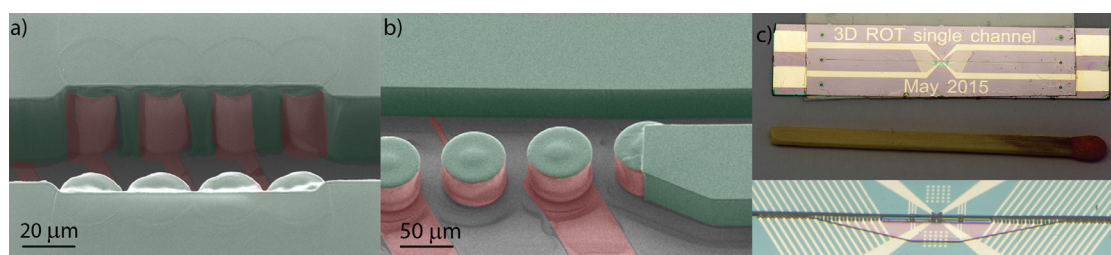
Figure 3.9 – 3D electrodes integrated into microfluidic channels. The SEM images demonstrating the possibility of side-wall integrated (a) and freestanding (b) electrodes in microfluidic channels. c) The channels are sealed by a PDMS-mediated bonding process of a thin glass slide on top of the electrodes.

The cause of the problem lies most likely in the dry etching process. Our hypothesis is that the plasma etching of the film altered its properties and made it resist the NaOH treatment, probably due to the Teflon$^{\text{TM}}$ deposition during the Bosch etching process. There are different measures that could have been taken to solve this problem. Some of them being the optimization of the cleaning step, the use of a protection layer between the dry film and the SU-8, or the etching of the resist top layer with an oxygen plasma before the stripping. However, we decided to try a different strategy.

Etching trenches at the beginning of the process   This approach consists in etching the trenches approximately $300\mu m$ deep into the silicon substrate and then fabricate the 3D electrodes and microfluidic channels on the substrate with the pre-etched holes. The accesses were then completely opened at the end of the process by grinding the wafer from the backside. The advantage of this process is that the etching step can be done on the flat wafer and for this reason it is much easier to pattern a photoresist layer and use an additional oxide layer as hard mask. Furthermore, a wider range of chemicals can be applied to strip the photoresist, as the wafers do not contain any electrode structures. The complete list of parameters and tools that were used for the concerned steps can be found in the appendix (B.5.2). Nevertheless, this approach has two main concerns, first, in case of big trenches and access holes the mechanical stability of the wafer is impaired, second, the trenches will act as flow resistance during spin coating steps and thus a sort of "Edge-Bead-Effect" will impair the flatness of the photoresist. While the mechanical stability was not a major issue, the flatness did create more problems, especially in the second SU-8 step, where we did pattern the microfluidics. The problem was that in this second step, we had to pattern the microfluidic structures close to the access holes and for this reason the SU-8 was impacted. Finally, the uneven SU-8 layer impacted the sealing process of the channel and resulted in either the breaking of the top glass cover or led to incomplete sealing. While this problem could be overcome by adapting the design and leave more space around the access holes, this results in major design constraints and thus we decided to try a different strategy.

Shadow mask   For this approach, a rigid mask is fabricated that is stuck to the wafer for the etching procedure and is removed afterwards. The mask was fabricated in-house, based on a silicon wafer, as described in Annex B.5.3. While the concept worked with these masks, the main problem was that they were brittle and easily broke. The main cause for wafer breakage was the combination of an etching tool based on mechanical clamping and the high topography between the two wafers. The pressure exerted on the border of the wafer results in a torque moment, which leads to mask failure. For this reason, we designed the next version of shadow masks with a diameter smaller than the clamping ring. The mechanical clamping then only holds the wafer, but not the mask (Fig. 3.10). In addition, we patterned a metal ring around the wafer to protect it from being etched. While these masks survived the etching procedure without problems, they heated up and burned the SU-8. There were two possible explanations why this did not happen with the bigger masks. First, the masks were sufficiently
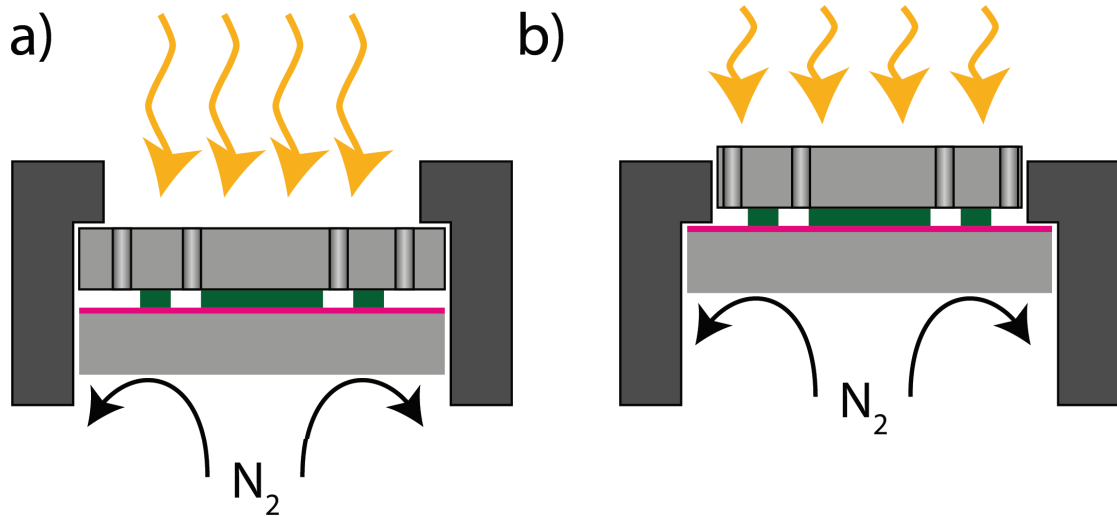
Figure 3.10 – Schematic of the mechanical clamping of shadow masks with different diameters. a) With a regular mask, the clamping is performed on the mask, which breaks easily due to the pressure of the clamping ring in combination with the high topography that results in a torque moment exerted on the shadow mask. b) A smaller mask has the advantage that it fits inside the clamping ring and for this reason, the clamping is performed on the wafer and not on the shadow mask to avoid the torque moment and the breaking of the mask.

cooled through the wafer. Second, sufficient heat conduction occurred through the clamping ring. However, since the clamping ring is not actively cooled and is exposed to the plasma, the first hypothesis is more likely and the cooling might result from pressing the mask border on the wafer.

While this procedure allowed us to fabricate chips with backside accesses, the problem with the failure of the mask resulted in long procedures and made the process unnecessarily expensive. While this problem might be overcome (e.g. by using a metal mask that is flexible enough and has good thermal conductivity), the etching through the deep trenches took much longer than similar etching on a flat wafer. And for this reason, we decided to try to use a hard mask for the etching as explained next.

Hard mask   In this last approach, an aluminum hard mask is sputtered on the wafer. Aluminum provides good etching resistance and is easy to remove. For the patterning of the mask, a standard $4\,\mu m$ thick photoresist is applied on top of the aluminum. The photoresist is overexposed to guarantee good patterning inside the 3D topography and the aluminum and underlying oxide layers are structured by wet and dry etching. The pattern is then transferred into the silicon by Bosch etching and the remaining photoresist is removed by IPA, and the Al is dissolved in a bath of NaOH (1M). The advantages of this approach are the high selectivity for silicon over aluminum during the Bosch etching; good patterning precision (although slightly lower than with standard photolithography due to the overexposure); and the possibility of

aligning the trenches with photolithographic precision.

Comparison of the different etching methods   The different strategies to etch through the wafers are summarized in Table 3.1. Although not all the options worked in our case, the problem in some cases resulted from design restrictions or equipment availability and thus might work in other configurations. Furthermore, the table summarizes possible approaches to troubleshoot the processes.

While so far, we mostly considered this etching step to realize the microfluidic access, we also made use of the same step to etch cleave marks into the wafers. The advantage is that once the cleave marks are designed, there is no additional cost and we do not have to dice the wafers and thus can safe a processing step. Furthermore, as dicing is a rather harsh process, it also reduces the risk of chip damage. Finally, this approach allowed us to place two further chips on the wafer that are rotated in respect to all the other chips. While in the case of dicing, the chips would be cut in half, while dicing the other chips, this was not the case for the cleaving. For this reason, we could reduce fabrication cost by about 25 percent, as we had 9 chips that were fabricated in parallel, instead of 7. Nevertheless, we had to optimize the shape of the cleave marks to work properly, as described below.

Table 3.1 – Comparison of the different etching processes to realize microfluidic accesses on the backside of the wafer.

	Dry film	Etch at the beginning	Shadow mask	Hard mask
Process steps	3	4	2^1	4
Process difficulty	+	+	+++	++
Patterning resolution	$25\,\mu m$	$10\,\mu m$	$20\,\mu m$	$10\,\mu m$
Alignment accuracy	$1\,\mu m$	$1\,\mu m$	$50\,\mu m$	$1\,\mu m$
Worked	No	No	$(Yes)^2$	Yes
Problems	Dry-film removal	Uneven SU-8	Brittle mask	-
Improvements	lift-off layer	design optimization	SU-8 support structures or metal mask	-

[1] Without mask fabrication
[2] Worked but mask consumption was too high

Etching the chip outlines   The challenge with the cleaving was to find a design that grants enough stability for the wafer to survive the etching process, but enables easy cleaving. In our first design, we patterned $4500\,\mu m$ long and $200\,\mu m$ wide trenches, with some additional
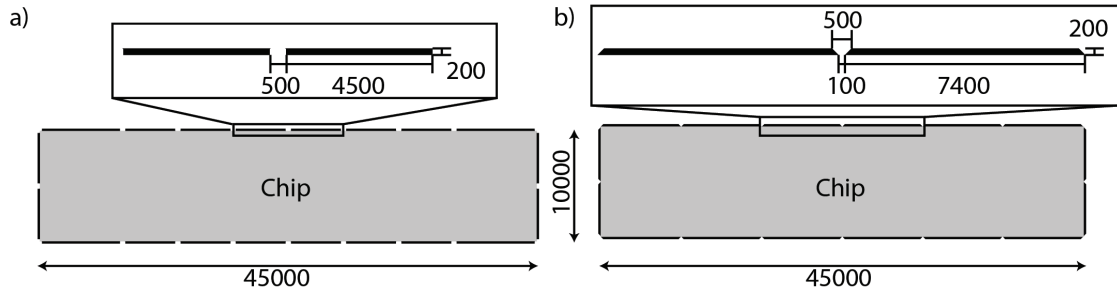
Figure 3.11 – The two versions of the trenches etched into the wafer for chip cleaving. The chip area is indicated in gray and the trenches that were etched into the wafer are in black. The top schematic shows a close-up on the trenches (in blue). All the dimensions are given in μm a) The first version with straight trenches. The trenches are 4500 μm long and 200 wide, while they are spaced by 500 μm gaps. The gaps are mostly rectangular, but have a small sharp corner close to the chip. b) The second design of the trenches, with trapezoidal trenches. The trenches are 7400 μm long at the base and 7000 μm at the top, with the base close to the chip. The base of two trenches are spaced by 100μm, leading to inverse trapezoidal shapes of the bridges, with the short part close to the chips, in order to avoid bridges after the chip cleaving.

triangles in the corners close to the chip. The latter was designed to enforce cleaving close to the chips and avoid having the bridges stay on the chips (Fig. 3.11.a top inset). Such trenches were distributed around the chips, with gaps of 500μm between two of them (Fig. 3.11.a bottom). Furthermore, the chips were designed with a frame around them to further increase the mechanical stability of the wafer. Although this first layout provided good stability for the wafers and enabled cleaving, the little triangles were not transferred properly into the silicon. For this reason, the silicon broke in the center of the bridges and bumps around the chips resulted. These bumps had to be removed in a later processing step because they hindered proper insertion of the chips into the chip holder and resulted in failure of the chips due to breakage.

For this reason, in a second design the trenches were designed as trapezoids, with the larger base close to the chips to favor cleaving on the chip border. We kept the width of the trenches at 200 μm and increased the length of the trenches to 7400 μm for the side closest to the chip and 7000 μm on the opposite side (Fig. 3.11.b inset on top). On the other hand, the gaps became inverse trapezoids. The bottom length closest to the chips was 100 μm, and the base on the other side was 500 μm (Fig. 3.11.b bottom). As expected, this design facilitated cleaving and resulted in smooth borders around the chips, without bumps. At the same time, it still provided sufficient mechanical stability for the wafers to guarantee safe handling and prevent failure of the wafers during the etching process.

Influences of electrode shapes on channel sealing   Although we already discussed the basic principles of channel sealing, we discuss here some final considerations on how the electrode design affects sealing quality. While in the beginning the goal was to use a simple pressure-

temperature bonding process [177], the problem was that the thin glass cover slides could not withstand it. The main problem was the unevenness of the second SU-8 layer resulting from the spin coating into the high topography of the 3D electrodes. Although this problem can be solved by applying an SU-8 layer thicker than the electrodes, this was not a valid option for us, as we targeted 3D electrodes that span the full height of the microfluidic channels. For this reason, we investigated the use of CMP to planarize the SU-8 layer [178]. Although this worked for small bumps, the stiffness of the SU-8 prevented removal of big bumps that prevented us to achieve proper channel sealing. However, in the beginning, we had much bigger 3D electrode shapes. For this reason, we decided to shrink them down, as smaller structures will have less impact on the SU-8 spin coating. While we could observe an improvement in the result, we were not able to achieve the proper sealing with a thin glass cover slip.

We then changed the bonding strategy to use a soft intermediate layer that could compensate for the eventual topography in the SU-8. Although we used a $10\,\mu m$ thick PDMS layer in the beginning, we later increased the thickness to $50\,\mu m$ to achieve better sealing.

While so far, we only considered the flatness of the SU-8, the PDMS must be considered as well. In a first attempt, we spin-coated the PDMS directly on the glass slides. However, this did not work properly due to the edge-beading effect that caused PDMS bumps on the border of the glass slides. For this reason, we used a dummy wafer, on which we first coated the PDMS and then deposited the glass slides on top of the still-wet PDMS. The wafers were then degassed to remove trapped air and the PDMS was then polymerized for $2\,h$ in a furnace at $80°$.

Chip and wafer design The microfluidic chips were designed in accordance with the simulations. However, each chip had some additional test structures similar to the ones used for the electrical characterization in the previous chapter. In addition, passive particle filters consisting of SU-8 pillars, with a diameter of $40\,\mu m$ and a gap of $20\,\mu m$, were patterned at the in- and outlet of the chips. Furthermore, the center of each chip contains an array of planar metal circles, with diameters and spacing of $50\,\mu m$ that can be used for image corrections and calibrations. Nine such chips were combined on a wafer with additional wafer-level test structures. We also kept the protective metal circle on the border of the wafer.

Fluidic and electrical access to the chips Finally, we designed a chip holder and a stage for our microscope (Fig. 3.12.a). The chip holder had standard microfluidic (Upchurch) and electric (SMB) connectors to provide access to the chip. We designed it with a big top window to provide access for bulky microscope lens. The top part of the chip holder held a PCB containing spring contacts for electrical connection, and the lower part provided microfluidic access. O-rings provided sealing between the chip and the lower part (Fig. 3.12.b). Finally, the chip holder was mounted on an upright microscope (Leica DM 2500), which is compatible with the observation of cells on nontransparent substrates.
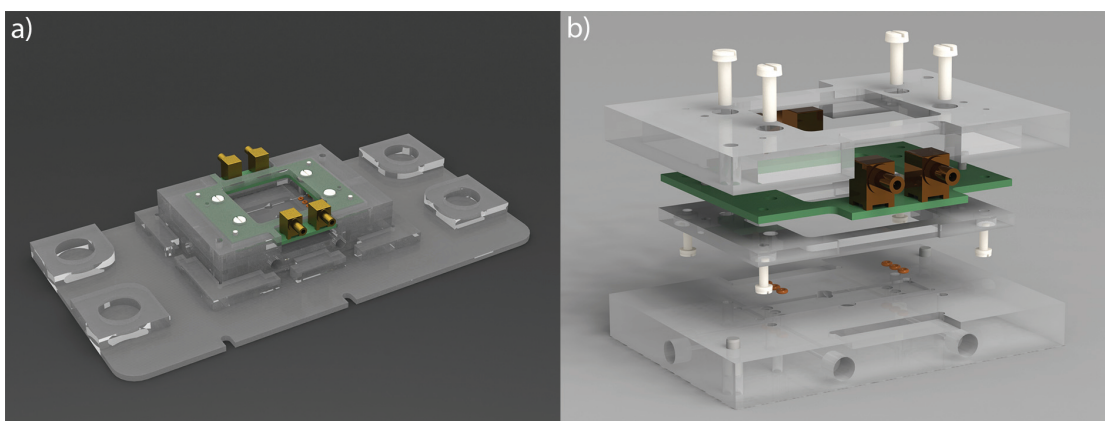
Figure 3.12 – CAD Drawing of the chip holder with its different parts. a) A custom microscope plate fixes the chip holder under the microscope and provides additional fixation for valves. b) The chip holder is an assembly of different parts to fix the chip and provide electrical and fluidic access.

3.2 Microfluidic liquid handling and stop flow

We now focus on controlling the flow and the liquid injections, together with the cell positioning inside the quadrupole. For this purpose, we needed a system that allowed accurate control of the liquid injections, with the ability to achieve a fast flow stop. There is a wide range of pumping techniques that are commonly used for microfluidics. However, not all of them were suitable for our needs. We will provide a quick overview of the most common techniques and compare them on price, complexity, accuracy, flexibility, and the ability to achieve fast flow stop. For a more in-depth coverage of the topic, there are specialized reviews, such as [179, 180, 181, 182].

The working principle of **Syringe pumps** is rather simple. A syringe is placed on the pump, with the piston fixed on a slider. The slider is moved through a screw that transmits the rotation of a stepper motor. The simplicity of such pumps makes them widely available and quite affordable. Furthermore, there are varieties that provide a wide range of flow speeds, accuracy, and ability to use different syringe sizes or multiple syringes at the same time. Nevertheless, one of the main problems with syringe pumps is that they may damage the chips, since the pumps are based on the application of a force on the syringe piston, with no direct control over the pressure. This results in long reaction times of syringe pumps and it can take up to several minutes to reach a stable state [183]. More precise flow stop can be achieved by combining two syringes and using them on each side of the chip, with the two pumps operating in opposite mode. Nonetheless, this approach requires accurate syringe pumps and increases the risk of chip damage due to high pressures that can build up if the pumps are not well synchronized. A further disadvantage of syringe pumps is that the injection is not constant, especially at low flow speeds, as the movement of the piston might be discontinuous. There are two main reasons for this. First, syringe pumps are generally based on stepper motors. Second, the

mechanical driving of the piston over the screw might reach its limits and lead to ratchet-like movement.

Peristaltic pumps are based on the movement of a rotor-based system that compresses tubes to move the liquid trapped inside. Although such systems are affordable and used for different applications, they are generally more suitable for handling large liquid volumes. Peristaltic pumps can be used bi-directionally, to inject and withdraw fluid. However, the flow is pulsatile and oscillatory, due to the working principle of the pumps [180]. In addition to commercially available peristaltic pumps, there are also examples of micro-peristaltic pumps that can be fabricated right on the microfluidic chips [184].

Although **pressure-driven systems** are quite similar to syringe pumps, there are some subtle differences. In contrast to syringe pumps, in which a force is applied to inject the liquid, pressure-driven systems control the injection by direct application of pressure on the liquids. This provides high control over the pressure inside the liquid circuit and avoids damage to the chips caused by high back-pressures that can build up with other systems. In addition, flow sensors can be added to the system in a feedback loop, in order to achieve control over the flow speed. The fast reaction times of such systems provide good control over the sample injection and enable to achieve fast flow stop. Nevertheless, such systems generally come at a high cost and level of complexity. Furthermore, the flow throughput depends on the applied pressure and the total flow resistance of the system. Although this might be considered a disadvantage, it also provides further ability adjust the flow rate [185].

As its name states, **centrifugal microfluidics** is based on centrifugal forces that are exerted when fluids are spun on a disc. For this purpose special discs are designed that combine different functions, such as valving or mixing. These discs are placed on a spin stand that controls the speed of rotation and combines further access to the disc if needed. Valving is mostly based on surface tensions, and the valves can be designed and positioned on the disc to break at specific rotation speeds [186]. This allows the liquid to be handled through a simple protocol of rotation speeds. Nevertheless, the main disadvantage of such systems is that it is only possible to achieve liquid flow away from the disc center, without the ability to reverse the flow.

Electro-osmotic flow (EOF) is based on the application of electrical potentials to move the electrical charges inside the Stern layer of the microfluidic channels. One of the advantages of EOF is that it is not based on the application of pressure or similar and thus no microfluidic connections are needed. It is enough to have two liquid reservoirs, with electrodes placed inside. However, the main disadvantage of this technique is the high voltages that are required. Signals in the range of several hundreds (or even thousands) of volts are generally needed, depending on the channel dimensions. Although there are DEP devices that use insulating pillars to shape the strong electric field created by EOF [187, 188], there are no such devices that enable ROT with this technique. For this reason, there would still be a need for metal electrodes. Such electrodes might actually impact the technique to work and further investigation would

have to be performed to ensure this technique to work.

Capillary pumping is a passive technique, where liquid is displaced by capillary forces. The flow rate of such pumps is determined by the dimensions of the channel and its surface tension. The advantage is that it is a passive technology and does not require additional equipment. Furthermore, it allows for accurate control on the flow speed [189, 190]. However, the disadvantage of the technique is that as it is passive, it does not allow for flow control and stopping the flow speed. Finally, as the capillary technique is based on surface tensions, the presence of the metal electrodes alters the tension and might affect it from properly working [191].

From the above descriptions, it can be seen that only syringe pumps and pressure-driven systems provide the ability to achieve flow stop in microfluidic channels (Table 3.2). Since syringe pumps are widely available, we first tried to implement flow stop by combining two syringes connected on each side of the chip. The syringes worked in opposite mode, meaning that when one injected fluids, the other withdrew them. We used a custom Labview interface that enabled fast, simultaneous control over the two syringe pumps. Although we had better control of the injections than with a single-syringe pump, we could not achieve good flow-stop capabilities. For this reason, we chose to use a pressure driven system and implemented it as explained in the next part.

Table 3.2 – Comparison of different solutions for handling microfluidic samples

	Syringe pump	Peristaltic pump	Pressure system	Centrifugal	EOF	Capillary
Flow control	++	++	+++	++	+	+
Withdraw	Yes	Yes	Yes	No	Yes	No
Fast flow stop	(Yes) [1]	No	Yes	No	No	No
Equipment	–	——	——	–	——	-
Cost	$$	$$$	$$$	$	$$	$
Flow range						

[1] Possible with two syringe pumps

3.2.1 Implementation of the pressure-driven flow system

Although the principle for achieving flow stop is rather simple – applying the same pressure on both ends of the chips – it requires a pressure pump or controller, and a valving system. We applied a static pressure on the pressure controller (Elveflow OB1) and used the flow multiplexer (Elveflow MUX) to control if, and on which side, the pressure is applied (Fig. 3.13). In this way it is possible to inject the sample into the chips (high pressure on the inlet, low pressure on the outlet), stop the sample (high pressure on both sides), or withdraw the sample (low pressure on the inlet and high pressure on the outlet). The advantage of this approach, as opposed to direct control of the pressure, is that the flow multiplexer is much faster in opening
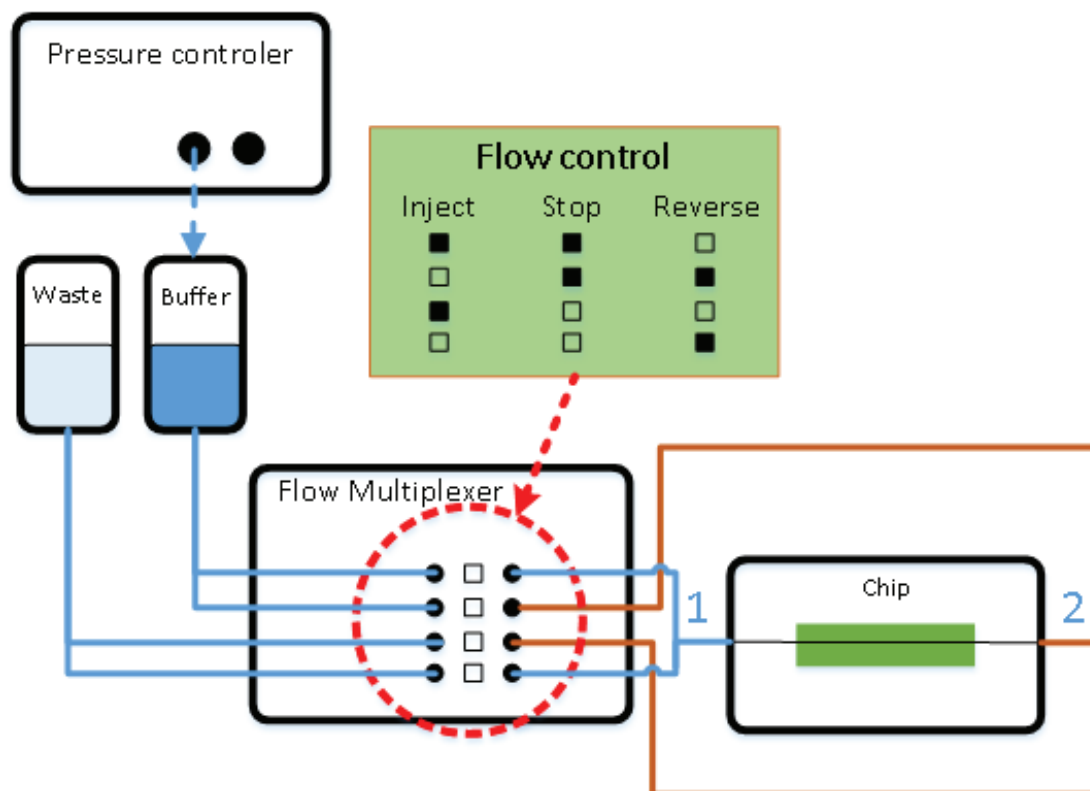
Figure 3.13 – The basic principle of the microfluidic system to achieve flow stop. The schematic shows that a constant pressure is applied on the buffer reservoir, while the waste reservoir is at atmospheric pressure. The sense of injection inside the chip is then controlled through a flow multiplexer, that enables to either inject, withdraw or stop the flow.

and closing the valves (20 ms) than the pressure controller in adjusting the pressure (down to 40 ms). Furthermore, this technique allows to work with one pressure source that is driving the liquids and for this reason it will always be the same pressure that is applied on both sides, while in the case that two pressure sources are used, a mismatch in pressure might result.

This basic system was then modified to increase the flow stability and enable fast injection of biological samples. First, we used a pressure controller with two channels and applied the pressure in a differential manner. This allows to rise the base pressure and small perturbations (tubes that move) had less impact on the flow speed. Second, we added an L-valve in front of the chips where we could directly inject the cells. This allowed for fast injection of the cells, as they do not have to go through the full flow system. This valve had two positions: one to inject the cells, and the other for the buffer (Fig. 3.14). In addition, we added a valve at the end of the system to add an additional flow resistance to the circuit. This resistance allows increasing the overall resistance of the complete flow circuit and thus it enables to reduce the flow speed, as we will explain in more details in the next section.

Figure 3.14 – An updated version of the basic schematic of the microfluidic system. We adjusted the system to work in differential mode, to reduce instability that might result from small flow disturbances and we added different features for more control. We placed an L-valve in front of the chips that allowed to inject the cells right in front of the chips and to avoid them going through the full microfluidic system. Furthermore, an additional valve was placed before the waste container. This valve allowed to increase the flow resistance of the full system, in order to reduce the flow speed.

3.2.2 Calculation of the flow speed

For a pressure-driven system, the flow speed depends on the total resistance of the fluidic system. For this reason, we first develop the mathematical expressions to calculate the flow resistance and the throughput of the system and later discuss the practical applications for the control of the flow speed of the system.

The flow speed inside a tube is given by *Poiseuille's law*:

$$Q = \frac{\pi r^4}{8\eta L}\Delta P = \frac{1}{R}\Delta P \tag{3.1}$$

with ΔP the pressure difference across the tube, Q the flow speed, η the dynamic viscosity of the solution, L and r the length and the radius of the tube. Finally, by expressing the fraction as the resistance of the circuit (Eq. 3.1), the similarity with *Ohm's law* becomes obvious.

Figure 3.15 – The different flow resistances of the microfluidic chips. a) schematic of the microfluidic channels of the electrorotation chips. b) illustration of the circuit we used to calculate the flow resistance with the different channels.

Although the flow resistance as described above (Eq. 3.2) is only valid for channels with a circular section, the resistance for a rectangular section can be calculated as in Eq. 3.3.

$$R_{tube} = \frac{8\eta L}{\pi r^4} \tag{3.2}$$

$$R_{rectangle} = \frac{12\eta L}{wh^3 \left[1 - 0.63 \frac{h}{w} \tanh\left(1.57 \frac{w}{h}\right)\right]} \tag{3.3}$$

With these basic equations, we can use the analogy with electrical circuit theory and use *Ohm's* and *Kirchhoff's* laws to calculate the total flow resistance of the system [192].

Eq. 3.3 can be used to calculate the flow resistance of the microchips. For this, we split the channel into four parts: The long inlet channel, the central part with the rotation and side channel, and the long outlet channel. For our calculations, we approximated the channels with rectangles (Fig. 3.15). The dimensions and the values for each channel can be found in Table 3.3 and Fig. 3.14. By applying *Kirchhoff's law*, the total flow resistance can be calculated as:

$$R_{chip} = R_{inlet} + \frac{R_{ROT} \cdot R_{side}}{R_{ROT} + R_{side}} + R_{outlet} \tag{3.4}$$

Under the assumptions that R_{inlet} and R_{outlet} are the same and that R_{main} is much bigger

than R_{side}, the formula can be simplified as:

$$R_{channel} = 2 \cdot R_{inlet} + R_{side} \qquad (3.5)$$

Finally, with R_{side} being two orders of magnitude smaller than R_{inlet}, the resistance of the side channel can be neglected.

We next used *Kirchhoff's second law* to calculate the reduction of the flow speed in the ROT channel due to the side channel. From *Kirchhoff's first law*, we know that the pressure difference over the ROT and the side channel must be equal:

$$q_{ROT} \cdot R_{ROT} = q_{side} \cdot R_{side} \qquad (3.6)$$

Where q_{ROT} and q_{side} are the flow rates through the two channels. By rearranging these values, we find:

$$q_{ROT} = \frac{R_{side}}{R_{ROT}} \cdot q_{side} \qquad (3.7)$$

And from eq. 3.7 it becomes clear that the flow rates through the channels can be adjusted by the ratio of the resistances of the two channels.

Table 3.3 – The flow resistances of different parts of the microfluidic channel

	Length μm	With μm	Height μm	Flow resistance Pa s m^{-3}	Volume μL
R_{inlet}	10000[1]	100	50	1.40×10^{13}	0.05
R_{side}	3000[2]	600	50	5.08×10^{11}	0.09
R_{ROT}	2000[3]	40	50	1.45×10^{13}	0.004

[1] Long access channel 2x
[2] Side channel to reduce flow speed
[3] Main channel for ROT

Knowing the flow resistance of the microfluidic channels, we will now turn to the calculation of the resistance that the fluidic connections and tube will contribute. We chose to use PEEK tubing for our system, as it provides high strength and rigidity to prevent dilatation of the tubes in case of fast flow switching and at high pressure. We used tubes of different diameters and lengths with the dimensions indicated in Table 3.4 and the location in Fig. 3.14. According to

Kirchhoff's law, the total flow resistance can be found by summing up all the flow resistances in the system. We used eq. 3.2 to calculate the resistance of the single tubes and added them up to calculate the total resistance for each tube diameter. In our case, the green and orange tubes were regular tubes that were fixed in the flow system, and the red tube provided additional resistance to reduce the flow speed. By comparing the resistance values of the chip (table 3.3) with those of the tubes (table 3.4), it becomes clear that without the red tubing, the total flow resistance is dominated by the one of the chips. For this reason, the green and orange tubing can be neglected. However, the additional resistance (red tubing) has a flow resistance of approximately one order of magnitude greater then the chip, so when added, reduces the flow speed by about one order of magnitude.

Table 3.4 – The flow resistances of the different tubes of the fluidic system

Color	Length cm	Diameter mm	Flow resistance $\mathrm{Pa\,s\,m^{-3}}$	Volume µL
Green	49	0.762	5.93×10^{10}	223.5
Orange	62	0.508	3.80×10^{11}	125.7
Red[1]	189	0.127	2.97×10^{14}	22.8

[1] Additional resistance to reduce flow speed

Finally, we calculated the time to fill the system and the passage time of a particle through the full system. These values are important to guarantee that no air bubbles remain in the system and to get an indication of the filling times of the system. In addition, the time of cells to pass through the system can be calculated. We first calculated the total volume of the system with the values provided in the tables above. The flow speed is given by eq. 3.1 and the filling time results from dividing the total volume by the flow speed. It can be seen that reasonable filling times can be achieved with high pressure and without the additional flow resistance. However, it has to be considered that these filling times are only estimates and that the real times would be lower, as the calculation do assume fixed resistances of the tubes etc. However, as in the beginning the tubes are empty, the resistance will constantly adjust and increases from almost zero to the indicated value.

3.2.3 Filling the microfluidic system and extracting bubbles

One of the big problems with microfluidic systems is the creation or trapping of bubbles inside the channels. Once bubbles get trapped inside a system, they alter the flow stream and can cover major parts of the chips such as sensing areas. Therefore, we followed a special filling protocol to first fill all the tubes and the chip with water and make sure the system was properly sealed. The water was then substituted with the DEP buffer prior to the experiments. Nevertheless, even careful filling of the system most times resulted in bubbles due to the channel design. In addition bubbles could result either from being trapped in the liquid or being generated by electrolysis. In such cases, it was possible to apply a pressure from both

Table 3.5 – Calculation of the flow speed and approximate filling times for the fluidic circuit

Pressure mbar	Flow resistance $Pa\,s\,m^{-3}$	Total volume μL	Flow speed $μL\,min^{-1}$	Time to fill min
1	$2.4 \times 10^{13*}$	349.22	0.02	1631.86
200	$2.4 \times 10^{13*}$	349.22	42.80	8.16
1	$2.97 \times 10^{14**}$	373.16	0.21	18 446.86
200	$2.97 \times 10^{14**}$	373.16	4.04	92.23

[*] Without external resistance
[**] With external resistance

sides, to expel the air. This worked thanks to the intermediate PDMS layer, which is permeable to air [193]. Although the time of bubble ejection depends on the size and volume of the trapped air, it took only few minutes to expel the bubbles (Fig. 3.16.

3.2.4 Control of flow speed and fast flow stop

Finally, we tested the flow-stop capabilities of our system with HEK cells diluted in PBS. The cells were injected into the system, and we used different pressures to study the system's capabilities to reach a fast flow stop. The cells were stained with acridin orange and visualized at a frame rate of 10 fps. We used a 20x lens for the imaging, as this allowed us to visualize the full width of the microfluidic channels. We first injected the cells at high flow speeds, by applying a pressure of 200 mbar at the inlet. While in this case, it was not possible to see the cells pass, as they were too fast for the camera to detect them (Fig. 3.17.a and b), we could achieve fast flow stop where it only took a short time where the cells oscillated (Fig. 3.17.c and d), and finally reached a stable position (Fig. 3.17.e-f). From these experiments we learned that we can reach fast flow stop in a fraction of a second, even at high flow speeds. Next we lowered the pressure to achieve slower injection rates and to study the cells propagation inside the microfluidic channel. For these experiments, we injected the cells with a pressure of $5\,mbar$ and used a particle-tracking plugin (TrackMate) from ImageJ to detect the cells and extract their position. This data showed us that although the cells travel at different speeds, once the flow is stopped, they all stop together and keep a stable position, until we started to inject again (Fig. 3.18).

3.3 Single-cell positioning and rotation

With the system in place, we will now report on different experiments that were performed to show the proper functioning of the system with its different elements.
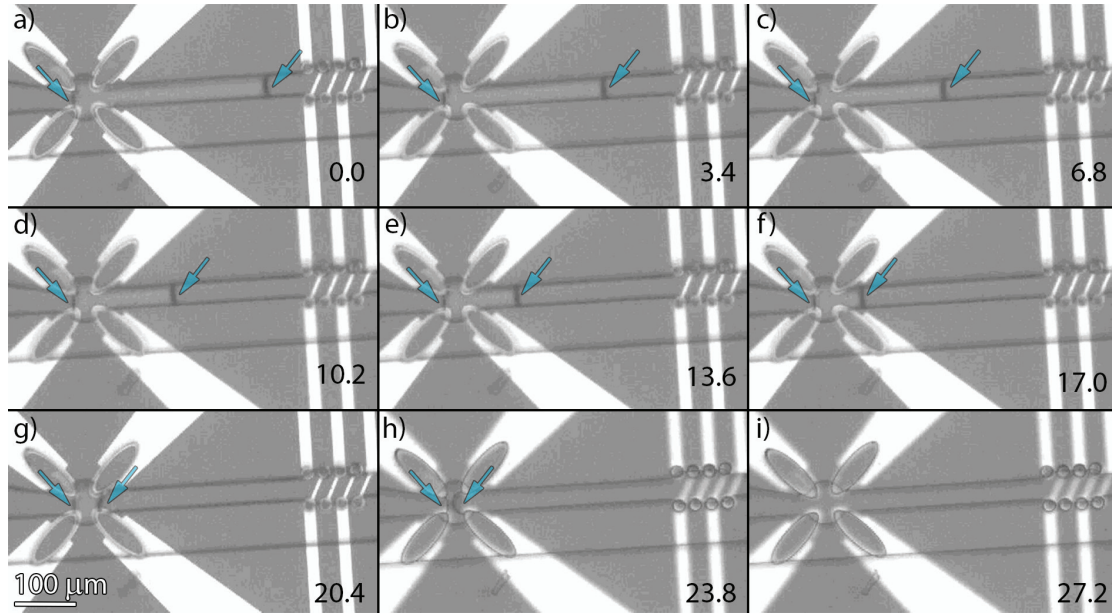
Figure 3.16 – An image sequence of bubble extraction through the intermediate PDMS layer. The images show the electrode quadrupole on the left of the images and the main microfluidic channel with a trapped air bubble in the central part. The liquid-air interfaces are indicated by the arrows. A pressure of 200 mbar is applied on the in- and outlet of the chip to expel the air bubble through the intermediate PDMS layer.

Deflection of liposomes into the ROT channel

Liposomes are of special interest, as they are cell-like particles that can be fully engineered. Therefore, vesicles were used to verify the basic ROT theory and the accuracy of fitting models [194, 74]. Lipid vesicles are perfect tools for electrokinetic experiments, because they can be thoroughly engineered and it is not only possible to adjust the outside medium, but even lipid composition as well as their interior. Experiments on such vesicles are of great interest, as ROT provides high sensitivity for membrane parameters, especially membrane capacitance [62].

For this reason, we used giant unilamellar vesicles (GUVs) for electrokinetic experiments, that were prepared from a mixture of DOPC and cholesterol (70:30) by electro-formation in an iso-osmotic sucrose solution ($270\,mM$). In addition a fluorescent dye (DiI, Invitrogen) was added at a concentration of 1% to visualize the vesicles. Prior to the experiment, the solution was diluted at a ratio of 1:20 into PBS (1x). The vesicles had a low internal and a high external conductivity in order to experience nDEP over a wide frequency range and we used a signal with an amplitude of $3\,Vp-p$ and a frequency of $10\,kHz$ to deflect the vesicles that were injected into the chips with a pressure of $2\,mbar$. These experiments showed that the vesicles were carried by the flow stream and tried to escape through the pillars into the side channel, however, the DEP barriers were strong enough to retain them and focus them into the rotation channel (Fig. 3.6). Furthermore, we could observe the vesicles to slow down with the entry into the main rotation channel, as we would expect from the decrease in flow throughput in
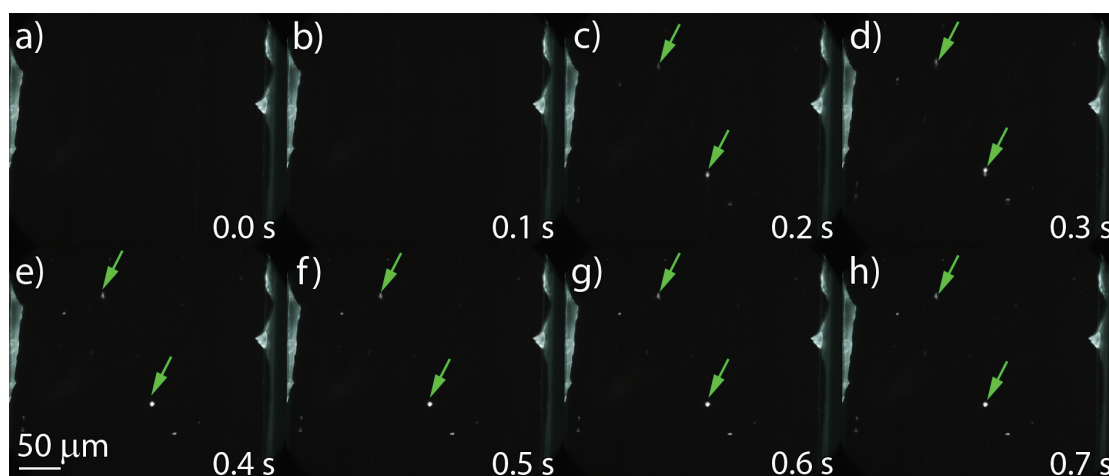
Figure 3.17 – An image sequence showing fast flow stop at high injection rates. The image sequence shows a part of the channel with the channel sidewalls indicated in blue. The cells were injected at a flow speed that was too high to detect the cells when they were injected (a, b). However, when we switched from injection to flow stop, the cells (indicated by arrows) oscillated for a short time (c, d) and reach a stable position (e, f).

this channel. However, one of the major problems with the vesicles is their almost perfect round shape that impair the observation of their rotation.

Electrorotation of vesicles with lipid rafts

In order to facilitate the observation of lipid rotation, one idea was to use lipid mixtures that undergo lipid phase separation, where it is possible to stain for each phase separately and for this reason grant higher contrast for the study of rotation. A lipid mixture based on sphingomyelin, DOPC, and cholesterol (50/27/23) was used to form giant unilamellar vesicles (GUVs) by electroformation in sucrose medium. The temperature of lipid vesicles formation was raised to 65° in order to guarantee good lipid mixing in the initial vesicles. And the rafts formed after cooling the mixture below the miscibility transition temperature Finally, the GUVs were diluted in 1x PBS for ROT experiments. The GUVs were then placed on electrorotation chips and were rotated at a frequency of 100 kHz. The lipid phase separation enabled partial staining of the GUV in order to facilitate the extraction of the rotation speed (Fig. 3.20). For this reason, the combination of ROT and raft-like GUVs can enable new possibilities to study protein-lipid bilayer interactions, study protein accumulation and pore formation processes likewise.

Positioning and trapping cells

Another important function to test was the cell positioning and trapping inside the electrode quadrupole. For this purpose, we used M17 neuroblastoma cells, as these cells provide a
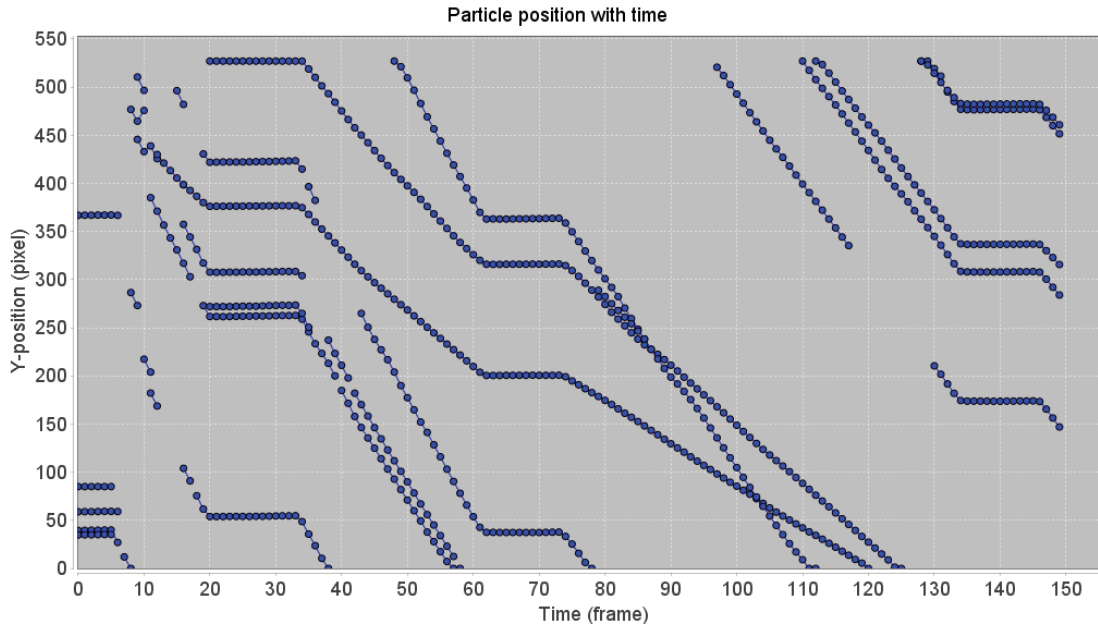
Figure 3.18 – Tracking results of individual cells inside the microfluidic channel. Although the cells move at different speeds, they all stop together and keep a stable position until the medium is injected again.

good homogeneity in size over a cell population. The cells were cultured and prepared as explained earlier and were diluted in a sucrose medium (300 mM) with a conductivity adjusted to 50 mS/m (PBS 1x). The cells were then injected as in the previous experiment and DEP forces were used to deflect them into the main ROT channel. The cells were injected at a pressure of 2 $mbar$, and we used the flow control with the flow multiplexer to position the cells (Fig. 3.21.a). Once the cells were inside the quadrupole, we stopped the flow and turned on the DEP signals to trap and center them by nDEP (Fig. 3.21.b).

Finally, the signals were switched from the DEP-trapping (180°-phase shifted) to electrorotation mode (90°-phase shifted) to rotate the cell (Fig. 3.22).

3.4 Conclusion

This chapter focused on integrating the 3D electrodes into microfluidic channels and the integration of the chips into the full system. One of the main challenges was to build a setup that was compatible with high NA lenses, which provide excellent image quality and high efficiency for light-gathering. However, such lenses only work at short distances and are bulky, which demands peculiar specification for the chips. We have developed a special microfabrication process that is compatible with high NA lenses. The process is based on the PDMS-mediated bonding of a thin glass coverslip on top of the channel and the realization of the microfluidic accesses on the backside of the chips.
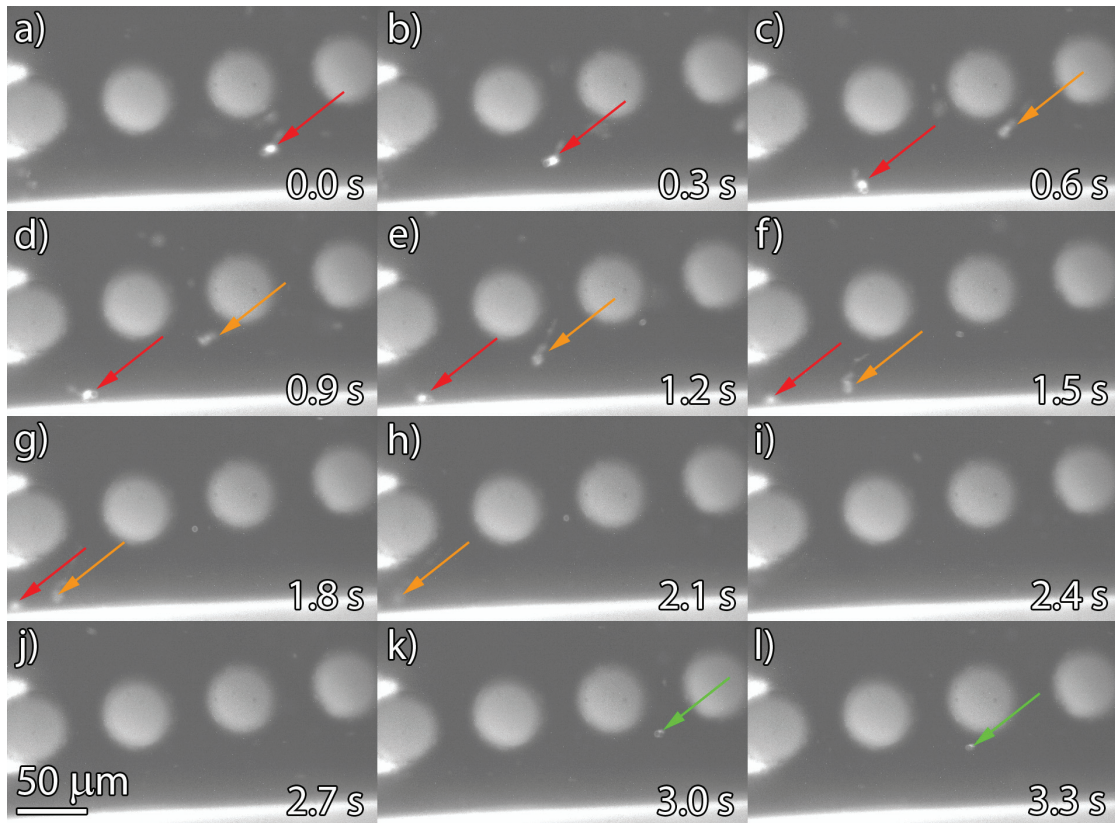
Figure 3.19 – The image sequence shows different vesicles (indicated by arrows) that are deflected into the rotation channel. The GUVs were engineered to undergo nDEP, so that they will be repelled from the DEP barriers that are formed in the middle of the 3D electrodes (solid white circles). Each vesicle was indicated with an arrow of a different color.

This chapter already discussed the microfluidic control, introducing a system that is able to achieve fast flow stop. These flow stop abilities were characterized in different experiments and we showed that it is possible to achieve fast flow stop even at high flow speeds. In other experiments that were performed at lower flow speed, we were able to track individual cells and we could show that, although the cells travel inside the channel at different speeds, they stop all together and keep a stable position, even over longer times.

In addition, we built an interface that allows to control and coordinate the different parts of the setup. The interface enables to set up and coordinate all the tools, and automatically and quickly acquire a full cell-rotation spectrum. Some additional tools were developed as well that helped with the conversion and analysis of the acquired data. First, a program was built for automatic conversion of the original experimental data to standard .tif files. Second, another program was built to automatically detect cell rotation by making use of pattern matching algorithms. Finally, a third program allowed to correct and sort data and calculate the speed of rotation, in order to plot the Clausius-Mossotti factor. We showed that the pattern matching algorithms allowed for fast and accurate extraction of the rotation speed and only
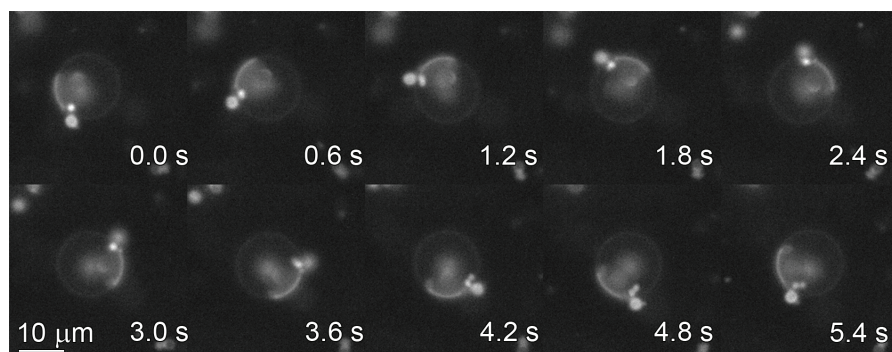
Figure 3.20 – Rotation of a GUV with a lipid raft at 100 kHz. The GUVs were formed by electroformation with a lipid mixture of DOPC, sphyngomyelin and Cholesterol. The vesicles were then partially stained with DiI, that only staines one type of lipid phase order. The lipids contain a sucrose medium inside and are diluted in PBS at a high ratio. The imaging was performed over several seconds and the sequence shows that the partial staining of the vesicle facilitates the extraction of the rotation speed of the vesicle.
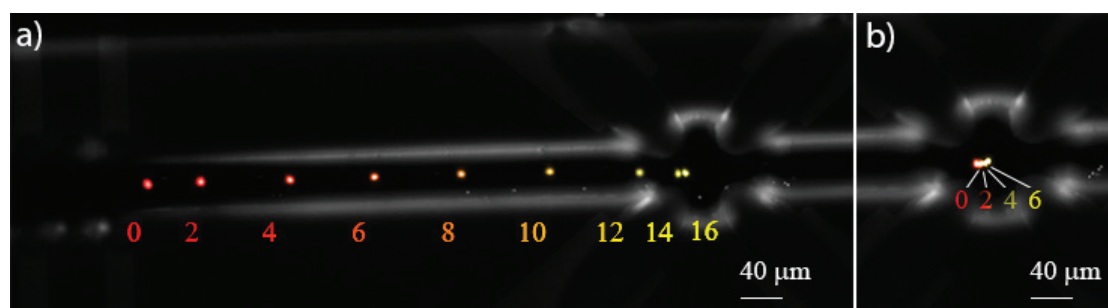
Figure 3.21 – Cell positioning in the small quadrupole by microfluidic sample handling (a) and DEP trapping (b). a) The cells are injected into the channel and brought into the quadrupole by fluidic injection. The images at different time points are superposed and the time in seconds is indicated for each position. b) The flow is stopped, and the cell is centered by nDEP with a signal at a frequency of $10 kHz$.

few seconds were enough to acquire enough images for accurate detection of the cell rotation speed. The requirements for such short sequences speed up the acquisition of a full ROT spectrum. We were able record a full spectrum with 30 frequencies in less than $3min$. While these three minutes are rather quick for ROT measurements, they are still quite long for single cell acquisitions. Although it might be possible to further increase the acquisition speed, by acquiring less images or frequency points, there are further limitations. First, almost half of the time of the acquisition was used to adjust the signal generator, which could be substituted by ad hoc electronics. However, pushing ROT measurements for single cells below the mark of around 1 min. might be challenging. Nevertheless, the throughput of such a system can be further increased, e.g. by multiplexing and we will introduce in the next chapter a fabrication process to achieve high density 3D arrays.

Finally, we presented experiments performed on the full system, in which we showed how to
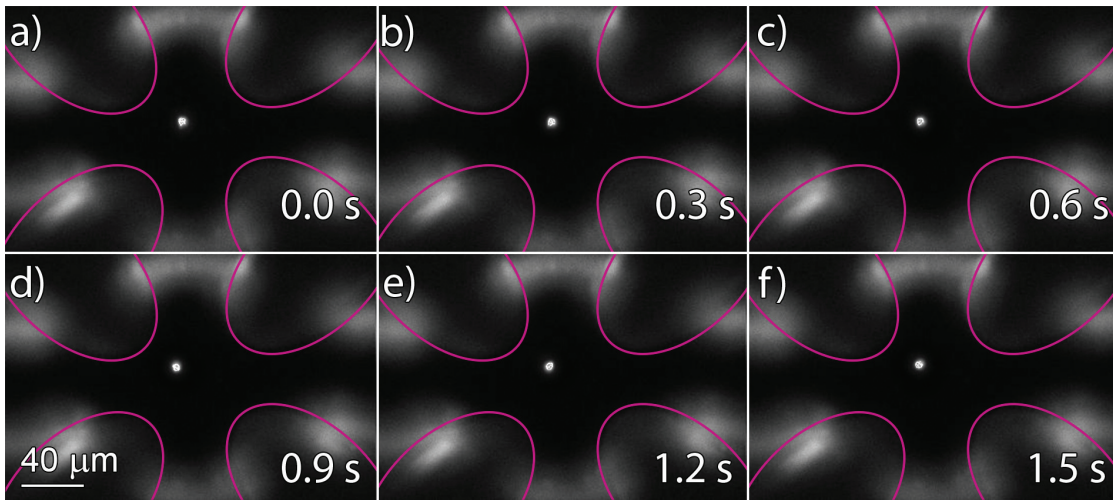
Figure 3.22 – An image sequence of an M17 cell that is rotated inside a quadrupole of 3D electrodes. The cell is suspended in a 10 mS/m iso-osmotic DEP buffer and four electrical signals at a frequency of 100 kHz, with a 90° phase shift are applied to the four electrodes (indicated by the purple outlines), resulting in clockwise (anti-field) rotation of the cell.

deflect ant trap single cells in the quadrupole. Although the parameters and strategies for these experiments were slightly modified from the initial simulation parameters, the experiments confirmed the basic working principle that we established at the beginning of the chapter with the simulations.

"They always say time changes things, but you actually have to change them yourself."

<div align="right">—Andy Warhol</div>

4

Summary and future work

This thesis reports on the development of a new setup based on 3D electrodes for fast characterization of single cells by electrorotation. For this purpose, we first developed new fabrication processes for the integration of 3D electrodes into microfluidic channels. We integrated such chips into a setup that allows the automatic extraction of a full electrorotation spectrum in less than 3 minutes. In what follows, we will give a summary of the main contributions of this thesis and indicate future developments of the platform.

4.1 Summary

4.1.1 3D electrode fabrication

Conventional microfabrication processes generally address the implementation of planar features since few non standardized fabrication methods allow the creation of 3D electrode structures which are largely limited in terms of conductivity, aspect ratio and density. Therefore, we developed new processes that are based on the homogeneous coating of insulating scaffolds with metals. In the first process we used passivated silicon pillars and demonstrated the viability of this approach to obtain highly conductive vertical features . However, the subtractive nature of the fabrication process led to design constraints and to relatively high costs and complexity due to the multiple process steps. For this reason, we developed an alternative fabrication process based on the metal coating of SU-8 structures. The additive nature of this process makes it possible to first pattern the planar metal lines, prior to patterning the 3D topography. Therefore, high resolution in the patterning can be achieved by the use of

a standard lift-off process. Different tests on such electrodes confirmed the presence, the proper connection, and the exposure of the metal layers. In addition, the additive nature of the process enables the use of substrates other than silicon, such as glass or even CMOS chips.

4.1.2 Microfluidic integration

For the integration of the 3D electrodes, we designed a new fabrication process that allowed the integration of the 3D electrodes into the microfluidic channels. The process is based on a second SU-8 layer that yields to matching heights between the channels and the 3D electrodes. The SU-8 allows the integration of the 3D electrodes into the channel sidewalls, as well as the realization of free-standing 3D electrodes inside the channels. Furthermore, the process was developed to be compatible with high NA lenses. For this purpose, we used thin glass cover-slips to seal the microfluidic channels and realized the microfluidic accesses on the backside of the wafers.

4.1.3 Microfluidic and electrokinetic particle positioning

The use of microfluidic sample handling enables fast and accurate particle positioning, for automatic sample exchange and prevents contamination or evaporation by granting a high control over the sample. Furthermore, a microfluidic platform based on a pressure driven system was developed, not only to reverse the flow direction, but also to stop the flow completely with high accuracy. The microfluidic chips were designed to combine microfluidic injections and dielectrophoretic forces to deflect, position and trap the particles. This combination allows single cells positioning at the center of the quadrupole by microfluidic injections and trapping of the cells by DEP forces. Finally, the electrical signals can be switched for particle analysis by electrorotation.

4.1.4 Automated extraction of electrorotation spectra

The development of a custom Labview interface not only enabled synchronization of all the setup components, but also made it possible to achieve automatic acquisition of full electrorotation spectra. The program automatically calculates frequency distributions and applies the single frequencies to the electrorotation chip, while recording the video of the rotating cell. A further program was developed for particle tracking and extraction of the rotation through pattern matching algorithms. The combination of high resolution images with such algorithms significantly enhanced the extraction of the cell's rotation speed from several minutes to only few seconds. Consequently, such fast detection enabled the acquisition of a full rotation spectrum with 30 frequencies in less than 3 minutes.
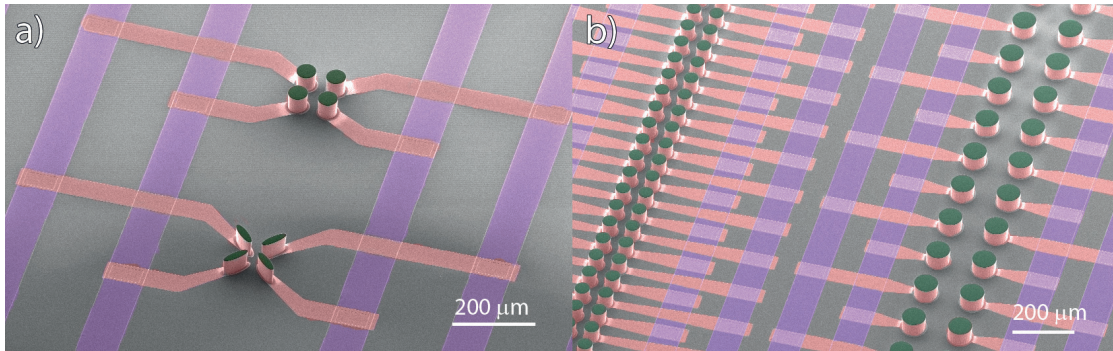
Figure 4.1 – SEM images of different array structures with multilevel metal connections. (a) Multiple electrode quadrupoles that can be energized through only 4 electrical connections. (b) SEM image of a high density 3D electrode array, where neighboring quadrupoles share their electrodes.

4.2 Future work

In this last section, we present the outlooks of the current thesis work and some experiments that we performed for future development of the system and its applications. We first demonstrate the achievement of high density arrays of 3D electrodes for assay multiplexing and in a second part, we cover interesting applications of electrorotation for future experiments.

4.2.1 Multilevel connection lines to achieve high connection densities

We showed that the full rotation system was able to acquire a full electrorotation spectrum in less than three minutes. Although it might be possible to increase the speed of acquisition with faster and more accurate algorithms, as described in [141], and with faster signal generators, we estimate that 1 minute time will be the lower limit attainable. We would like to point out that the employement of arrays of 3D electrodes would represent an advantage for other applications, such as flow cytometry [195, 144, 100] and dielectrophoresis [196, 197].

The additive nature of the SU-8 based microfabrication process was already discussed in Chapter 3. So far we described the use of a single connection layer, nevertheless, in order to increase the connection density and complexity of the chips we also explored the use of multiple metal connection layers. To this end, the main challenges were proper insulation of the bottom metal lines, in order to prevent short-circuits between the two metal layers, and the realization of connection vias. The process started with the patterning of a triple metal layer (Ti/Pt/Ti) by lift-off patterning. An SiO_2 layer was then sputtered on top of the layer and vias for the metal connection between two layers were structured by dry etching. A second metal layer (Ti/Pt/Ti) was then deposited on the wafer by sputter coating and structured by dry etching. The sputter coating assures proper connection between the two layers. Finally, the 3D structures can be fabricated on top of the multi-level connections as inscribed in the previous chapters. A picture of the outcome of the above-described process is shown in Fig. 4.1.
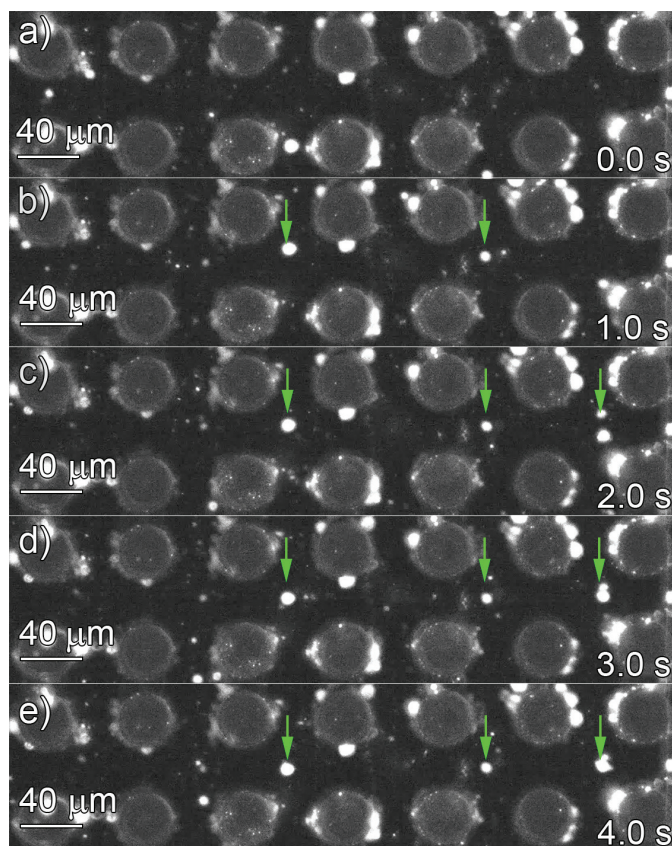
Figure 4.2 – A sequence of 5 images showing cells that are trapped inside an array of 3D electrodes. The cells are suspended in DEP buffer to undergo nDEP and are trapped at 10 kHz. The cells were injected with a syringe pump with the flow direction from bottom to top. It can be seen that although some cells stick to the pillars and got stuck there, there are different cells that are trapped in the center of the electrodes (indicated by green arrows).

Such arrays were employed in trapping experiments, where M17 cells were suspended in an iso-osmotic sucrose solution with a conductivity adjusted to $10\,mS/m$ (PBS 1x). The cells were injected into the microfluidic channels and were trapped by nDEP at a frequency of $10\,kHz$ (Fig. 4.2).

4.2.2   Electrorotation applications

There are many potential applications of the setup we developed during this PhD thesis, including the extraction of electrical parameters by ROT for drug screening, deciphering of disease-related cell biology , oxidative stress, molecular interaction with cells and even cytotoxicity. This latter application represented one of our main interests to test the ROT setup. In particular, we focused on the toxicity assessment of nanoparticles and their cellular uptake.
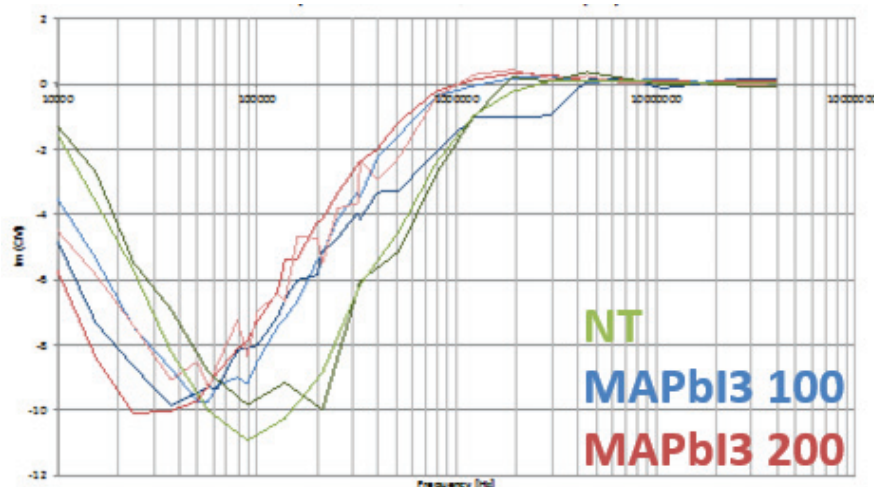
Figure 4.3 – Electrorotation results of different cells exposed to different doses of MAPbI3. The cells are assessed 3 days after exposure and show a dose dependent shift in peak frequency.

Nanoparticle toxicity assessed by electrorotation

The motivation to carry cytotoxicity experiments on our device comes from the ultrafast development of an engineered nanomaterial for photovoltaic applications. This material is a perovskite called Methylammonium Lead Iodide (or $CH_3NH_3PbI_3$. Hereafter MAPbI3) and has shown a very promising progress in light harvesting in solar panel prototypes. However, large-area solar cells installed on many buildings in the near future may contain a toxic material without understanding their toxic effects. So far, only one study reported the toxicity of these particles in vitro [198] and showed an apoptosis-like cell death in neuronal cells upon MAPbI3 exposure. However, the cellular uptake of these particles is still not yet fully understood. ROT experiments can be used to study the cellular uptake of nanoparticles [199] while providing insights about their toxicity [200, 201, 202, 203].

For this reason, we tested M17 neuroblastoma cells that were suspended in an iso-osmotic sucrose solution (270 mM) with a conductivity adjusted to 10 mS/m. Our study compared the exposure of M17 cells to different concentrations of MAPbI3 and showed a dose-dependent shift in the peak rotation frequency of the cells (Fig. 4.3). Nevertheless, the use of nDEP to direct the cells into the main rotation channel might affect the selection of the cells, as the perforated membrane of dead cells prevents strong membrane polarization. For this reason, rotation experiments with array chips might give more accurate insights. Another human cell line (A549 lung cells) was studied by the same group, and did not exhibit cell death. Instead, other subcellular damages were induced. Consequently, ROT experiments could be performed on this cell line with the same photovoltaic compound.

A

Parameters for Comsol simulation

A.1 Comsol simulation of electric fields

The simulation of the electric field distribution as well as the ROT torque moment and the DEP forces were performed using Comsol Multiphysics. The simulation were carried out on a 3D model, using the electric currents module in combination with a time domain solver. We chose to use a time dependent solver and set it up to calculate one full period of the signal frequency, so that it was possible to average the ROT torque and the DEP forces over one full period of the electric signal. The parameters and setting used for the simulation are given in Table A.1.

Table A.1 – The table gives an overview of the model parameters and settings used for the simulation of the electric field distribution created by 3-D and planar electrodes

Interface	Node	Property	Setting
Global Definitions	Parameters	V	$5\,V$
Materials	Medium	Electric conductivity	$100\mu S/m$
		relative permittivity	77
	Platinum	Electrical conductivity	$8.9 \cdot 10^6\,S/m$
Electric currents	Current conservation [1]		

Continued on next page

Continued on next page

Table A.1 – continued from previous page

Interface	Node	Property	Setting
		Electric insultaion[2]	
		Initial Values	$0\,V$
		Terminal 1[3]	V0*exp(i*pi*0)
		Terminal 2[3]	V0*exp(i*pi*90)
		Terminal 3[3]	V0*exp(i*pi*180)
		Terminal 4[3]	V0*exp(i*pi*270)
Mesh		sequence type	Physics-controlled mesh
		Element size	Extremely fine
Study	Parametric Sweep	V0	range(0,0.1,5)[4]
	Frequency Domain[5]	Solve for	Electric currents
		Frequencies	$10\,kHz$
		Initial Values of variables solved for	Initial expression
		Values of variables not solved for	Initial expression
	Time dependent[6]	Solve for	Electric currents
		Time unit	s
		Times	range(0, 1.0e-5/8,1.0e-5)[7]
		Initial Values of variables solved for	Initial expression
		Values of variables not solved for	Initial expression
Results	2D Plot	ROT x	abs(ec.Ez)*abs(ec.Ey)*sin(arg(ec.Ez)-arg(ec.Ey))[8]
		ROT y	abs(ec.Ez)*abs(ec.Ex)*sin(arg(ec.Ex)-arg(ec.Ez))[8]
		ROT z	abs(ec.Ex)*abs(ec.Ey)*sin(arg(ec.Ey)-arg(ec.Ex))[8]
		DEP x	timeavg(0,1e-5,d(ec.Ex^2,x))[8,9]
		DEP y	timeavg(0,1e-5,d(ec.Ey^2,y))[8,9]
		DEP z	timeavg(0,1e-5,d(ec.Ez^2,z))[8,9]

Continued on next page

Table A.1 – continued from previous page

Interface	Node	Property	Setting

[1] The domain was set to current conservation with the material properties taken from the medium

[2] All boundaries except the ones of the electrodes were set as insulators

[3] The electrode surfaces were selected according to their connection with the four pads

[4] Voltage range between 0 and 5 Volts with steps of 0.1 V, the range varied in some cases

[5] A frequency domain solver was used for the electric field and the ROT simulations

[6] DEP forces were calculated using a time dependent solver

[7] The DEP forces were simulated for 8 time points of one signal Period

[8] Equation used to plot the different components of the ROT torque and the DEP forces, for the visualization the different equations were mixed

[9] The DEP forces were averaged over one full signal period

A.2 Comsol simulation of microfluidic chips

Here we describe the simulation of the full microfluidic chips and note the different parameters that were used for the simulation. The simulations were performed on a 3D model using Comsol Multiphysics software and we used three different modules to solve the model. We started by calculating the flow speed inside the microfluidic device by solving a laminar flow module with a stationary solver, then the electric fields were calculated by solving an electric currents module with a frequency domain solver and finally, we used a particle tracing module that was solved with a time dependent module to calculate the particle trajectories. The three modules were linked together and the particle tracing module made use of the solutions from the two other modules to calculate the fluidic drag and the DEP forces.

Table A.2 – The table gives an overview of the modules, parameters and settings used for the simulation of the microfluidic chips and the DEP forces used for the particle focusing and trapping

Interface	Node	Property	Setting
Global Definitions	Parameters	V_ DEP	$3\,V$
		ch_ width	$110\,\mu m$
		V_ catch	$5\,V$
		R	$5\,\mu m$
Materials	Medium	Dynamic viscosity	$1.33\,mPa\cdot s$
		Electric conductivity	$100\mu S/m$
		Density	$1038 kg/m^3$
		relative permittivity	77
	Platinum	Electrical conductivity	$8.9\cdot 10^6 S/m$

Continued on next page

Table A.2 – continued from previous page

Interface	Node	Property	Setting
Electric currents	Current conservation [1]		
		Electric insulation[2]	
		Initial Values	$0\,V$
		Electric Potential 1[3]	V_ DEP
		Electric Potential 2[3]	-V_ DEP
		Electric Potential 3[3]	V_ Catch
		Electric Potential 4[3]	-V_ Catch
Laminar Flow	Fluid Properties		From medium
	Wall	Boundary condition	No slip[4]
	Initial values		zero
	Inlet	Boundary condition	Pressure, no viscous stress
		Pressure	$300\,Pa$
	Outlet	Boundary condition	Pressure, no viscous stress
		Pressure	$0\,Pa$
Particle Tracing for Fluid Flow	Wall[4]	Wall condition	Bounce
	Particle Properties	particle density	$1080\,kg/m^3$
		Particle diameter	$2\cdot R$
	Dielectrophoretic Force	Specify force using	Electric field
		Electric field	electric current module
		Complex particle relative permittivity	5
		Complex fluid relative permittivity	80
	Drag force	Drag law	Stokes
		Velocity field	spf/fp1[5]
		Dynamic viscosity	spf/fp1[5]
	Inlet	Initial position	Density
		Number of particles	20
		Velocity field	spf/fp1[5]
	Outlet	Wall condition	Freeze
	Gravity force	Gravity vector z[6]	-g_ const
		Density	spf/fp1[5]

Table A.2 – continued from previous page

Interface	Node	Property	Setting
Mesh		sequence type	Physics-controlled mesh
		Element size	Extremely coarse[7]
Study	Stationary	Solve for	Laminar Flow
		Initial Values of variables solved for	Initial expression
		Values of variables not solved for	Initial expression
	Frequency Domain	Solve for	Electric currents
		Frequencies	$10\,kHz$
		Initial Values of variables solved for	Study 1, Stationary
		Values of variables not solved for	Study 1, Stationary
	Time Dependent solver	Solve for	Particle tracing for Fluid Flow
		Time unit	s
		Times	range(0,0.005,1)[8]
		Initial Values of variables solved for	Study 2, Frequency Domain
		Values of variables not solved for	Study 2, Frequency Domain

[1] The domain was set to current conservation with the material properties taken from the medium

[2] All boundaries except the ones of the electrodes were set as insulators

[3] The electrode surfaces were selected according to their connection with the four pads

[4] All boundaries except in and outlets

[5] Linked to lamminar flow module

[6] x and y are 0

[7] A coarse mesh was required to match the calculation power

[8] Simulation of 1 second with 200 interval points

B

Microfabrication process parameters

In this chapter we summarize the different process steps and parameters for all the processes developed during this thesis. First we describe the parameters for the different processes concerning the fabrication of the 3D structures. Then we give a summary of the parameters used for the fabrication of the microfluidic channels and finally, we summarize the different options discussed in this thesis for the etching of the microfluidic accesses and the chip outlines.

B.1 Process flow for metal coated silicon structures

The first process presented in this thesis is the fabrication of metal electrodes based on the homogenous coating of silicon pillars with metal films. The different steps and the equipment used, as well as the corresponding parameters are given below.

Table B.1 – The different steps and process parameters for the fabricaiton of metal-coated silicon structures

Step		Machine	Program	Parameters
Photolithography	Spin Coating	Rite Track[1]	Az92xx	$4\,\mu m$
	Exposure	MA/BA 6	HC, CP	$270\,mJ/cm^2$
	Development	Rite Track[1]	Dev_Az92xx	$4\,\mu m$

<div align="right">Continued on next page</div>

Table B.1 – continued from previous page

Step		Machine	Program	Parameters
Dry etching	Oxyde Etch	Alcatel 601E [2]	SiO2	$1\,\mu m$
	Silicon etch	Alcatel 601E[2]	Si_ ambiant_ 2	$50\,\mu m$
	Restist stripping	Remover Bench Z2	Remover	2x5 min
Passivation	CVD	Centrotherm	$2\,\mu m$ wet oxide	
Metal deposition	Sputtering	DP 650[3]	Ti_ Pt_ unif	$50'' + 300''$
	Evaporation	Lab600	Ti	$20\,nm$
Patterning	Plasma descum	Tepla Z2 [4]	High	30 sec.
	Spray coating	EVG 150 Z6	spray	3 layers
	Exposure	MA/BA 6	HC, CP	$780\,mJ/cm^2$
	Development	EVG 150	spray dev	3 layers
Metal etch	Dry etching	STS [5]	Platinum	8 min
	Resist strip	Remover Bench	Remover 1165	2x5 min.
	Cleaning	Piranha Bench	Piranha	2x5 min.

[1] EVG zone 6   [2] Alcatel AMS 200 zone 2   [3] Spider zone 4   [4] Tepla Z11   [5] Veeco IBE zone 11

B.2   Process flow for metal coated SU-8 structures with connection lines patterned by dry film resist

Table B.2 – The different steps and process parameters for the fabricaiton of metal-coated SU-8 structures and patterning of the metal lines by photolithography with a dry film resist.

Step		Machine	Program	Parameters
Photolithography	Spin Coating	Rite Track[1]	Az90xx	$4\,\mu m$
	Oxyde Etch	Alcatel 601E [2]	SiO2	$1\,\mu m$
	Silicon etch	Alcatel 601E[2]	Si_ ambiant_ 2	$50\,\mu m$
	Restist stripping	Remover Bench Z2	Remover	2x5 min
Metal deposition	Sputtering	DP 650[3]	Ti_ Pt_ unif	$50'' + 300''$
Dry film	Lamination	Laminator Z1	Dupont MX 5050	Temp 95°C, speed 1
	Exposure	MJB 4	Hard Contact	$120\,mJ/cm^2$
	Development	Wet Bench Z13	MRD 4000/75 IC	2 min
Metal etching	dry etching	Veeco IBE Z11	Medium	3 min

Table B.2 – continued from previous page			
Step	Machine	Program	Parameters
dryfilm strip-ping	Wetbench Z13	NaOH 2M	20 min

[1] EVG zone 6   [2] Alcatel AMS 200 zone 2   [3] Spider zone 4

B.3 Process flow for metal coated SU-8 structures with connection lines patterned by lift-off

Table B.3 – The different steps and process parameters for the fabricaiton of metal-coated SU-8 structures that are connected by metal lines patterned in a lift-off process.

Step		Machine	Program	Parameters
Lift-off	Spin Coating	EVG 150[1]	Az1215 on LOR	$0.48\mu m$
	Exposure	MA/BA 6[2]	HC, CP	$42 mJ/cm^2$
	Development	EVG 150[1]	Dev_LOR	$0\mu m48$
	Descum	Tepla GiGAbatch[2]	High	30 sec
	Evaporation	Lab 600	Ti//Pt//Ti	$20\,nm/200\,nm/20\,nm$
	Lift-off	Remover Bench Z1	Remover 1165	overnight
SU-8 scaffolds	Spin coating	Sawatec coater z13 [3]	Gersteltec GM 1070	1600 rpm
	Soft-Bake	Sawatec Hot-plate z13[4]		$130°C 5 min.$
	Exposure	MJB 4	HC, CP	$380 mJ/cm^2$
	Post Exposure Bake	Sawatec Hot-plate z13[4]		$90°C 40 min.$
	Development	Wetbench z13		PGMEA $2x1.5 min$
	Hard bake	Sawatec hot-plate z13		$135°C, 2h$
Metal deposition	Plasma activa-tion	Tepla 300[5]	Prog 2	30 sec
	Sputtering	DP 650[6]	Ti_ Pt_ unif	$50\,sec + 300\,sec$
Metal etching	Ion Beam Etch-ing	Veeco IBE z11	Medium	$3\,min\,40\,sec$[7]

[1] ACS zone 1   [2] MA/BA 6 Gen 3 zone 1   [3] Sawatec coater zone 1   [4] Sawatec hotplate zone 1
[5] Tepla GiGAbatch zone 2   [6] Spider zone 4   [7] Monitored by SIMS

B.4 Process flow to realize microfluidic channels

Table B.4 – The process parameters to realize the microfluidic channels in SU-8.

Step		Machine	Program	Parameters
SU-8 scaffolds	Spin coating	Sawatec coater z13 [1]	Gersteltec GM 1070	1600 rpm
	Soft-Bake	Sawatec Hot-plate z13[2]		$130°C\,5min.$
	Exposure	MJB 4	HC, CP	$340\,mJ/cm^2$
	Post Exposure Bake	Sawatec Hot-plate z13[2]		$90°C\,40min.$
	Development	Wetbench z13		PGMEA $2x1.5min$

[1] Sawatec coater zone 1

[2] Sawatec hotplate zone 1

B.5 Processes for etching of Microfluidic accesses

In this last section, we give the parameters and the tools that were used for the different steps of the optimization, but we will only consider the steps that were concerned, without repeating the full process parameters.

B.5.1 Dry film resist

For the dry film process, we first fabricated the 3D electrodes with the connections and the microfluidic channels, as described above and then applied the dry film on top of the structures.

Table B.5 – The different steps and process parameters for the etching through the silicon wafer with a dry film resist mask.

Step		Machine	Program	Parameters
Device Fabrication	...	...	...	...
Dry film	Lamination	Laminator Z1	Dupont MX 5050	Temp 95°C, speed 1
	Exposure	MJB 4	Hard Contact	$120\,mJ/cm^2$

Table B.5 – continued from previous page

Step		Machine	Program	Parameters
	Development	Wet Bench Z13	MRD 4000/75 IC	2 min
Dry etching	SiO_2 etching	Alcatel 601E	SiO_2	4 min
	Si etching	Alcatel 601E	Si_ambiant_2	40 min
BS grinding	grinding	Disco DAG 810		$300\,\mu m$ thickness
	dryfilm strip-ping	Wetbench Z13	NaOH 2M	20 min

B.5.2 Etch at the beginning

For the fabrication of the vias by etching at the beginning, we started right away by patterning the access holes into the silicon substrate. We did not try this with the chip outlines, as the outlines would be even more critical for the SU-8 step, as they will lead to a higher flow resistance for the photoresist during the spin coating and thus even higher surface topography would result. For this reason, we used dicing at the end of the process to separate the chips.

Table B.6 – The process parameters for the fabrication option where the silicon accesses at the beginning of the process.

Step		Machine	Program	Parameters
Photolithography	Spin Coating	Rite Track	Az92xx	$4\,\mu m$
	Exposure	MA/BA 6	HC, CP	$270\,mJ/cm^2$
	Development	Rite Track	Dev_Az92xx	$4\,\mu m$
Dry etching	SiO_2 etching	Alcatel 601E	SiO_2	4 min
	Si etching	Alcatel 601E	Si_ambiant_2	40 min
	Resist strip	Remover Bench z2	Remover 1165	2x5 min.
Device Fabrication	...	...	...	...
BS grinding	grinding	Disco DAG 810		$300\,\mu m$ thickness
Dicing	Spin coating[1]	Rite Track	Az92xx	$4\,\mu m$
	Dicing	Disco DAD321	Nickel blade	$30\,krpm, 5\,mm/s$

[1] For device protection during dicing

B.5.3 Shadow mask

For the shadow mask process, we first had to fabricate the mask. This was done starting with a silicon test wafer, with a $2\,\mu m$ wet oxide layer on top. The fabrication process was similar to the first steps of the previous option, however, then we ground the wafer and sputtered a protective Al layer on top.

Table B.7 – The different process steps with their parameters for the option based on the etching of the through silicon accesses by shadow mask

Step		Machine	Program	Parameters
Photolithography	Spin Coating	Rite Track	Az92xx	$4\,\mu m$
	Exposure	MA/BA 6	HC, CP	$270\,mJ/cm^2$
	Development	Rite Track	Dev_Az92xx	$4\,\mu m$
Dry etching	SiO_2 etching	Alcatel 601E	SiO_2	4 min
	Si etching	Alcatel 601E	Si_ambiant_2	40 min
	Resist strip	Remover Bench z2	Remover 1165	2x5 min.
BS grinding	grinding	Disco DAG 810		$300\,\mu m$ thickness
	Resist removal	Remover Bench z2	Remover 1165	2x 5 min.
	Oxide etch	HF bench z2	BHF	$30\,min$
Metal sputtering		Spider	Al	$2\,\mu m$

Once we had the masks, we used to align and stick them to the wafer by a special wax (Quick stick 135). In order to do so, we then first applied the wax on the wafer, by heating the wafer to $110°C$ and pressing some spots of wax on top. Then the wafer was cooled down, so the wax hardened and would not stick right away. This allowed to align the shadow mask with the wafer and once good alignment was achieved, we heated the sandwich of mask and wafer to $110°$ to melt the wax and stick to the two wafers and once it cooled down it will fix them together. The etching was then performed by etching the SiO_2 and the Si with the same receipts as the once mentioned above.

B.5.4 Hard mask

Finally, we present the last fabrication option, which also worked the best, based on the application of a hard mask that is removed after the etching. We chose to use sputter coated aluminum, as it is easy to apply and it has a high resistance to the Bosch process. In this way, the damage to the mask can be reduced and only a thin aluminum layer is sufficient for

the etching of several hundreds of μm. In addition, aluminum has the advantage that it can be easily dissolved in NaOH, while all the other materials on the chip are inert to even long treatment with NaOH. The process parameters are given in the table below.

Table B.8 – The different fabrication steps and their parameters for the etching through the full wafer by application of a hard mask

Step		Machine	Program	Parameters
Device Fabrication	...	...	...	...
Hard mask deposition	Al sputtering	Spider	Al	$500\,nm$
Photolithography	Spin coating	Rite Track	AZ92xx	$4\,\mu m$
	Exposure	MA/BA 6	HC, CP	$600\,mJ/cm^2$[1]
	Development	Rite Track	Dev_Az92xx	$4\,\mu m$
Pattern transfer	Al etch	Metal wetbench z2	ANP	$2min$
Dry etching	SiO_2 etching	Alcatel 601E	SiO_2	4 min
	Si etching	Alcatel 601E	Si_ambiant_2	40 min
	Resist strip	Remover Bench z2	Remover 1165	2x5 min.
BS grinding	grinding	Disco DAG 810		$300\,\mu m$ thickness
cleaning	Resist removal	Remover Bench z2	Remover 1165	2x 5 min.
	Al etching	Laboratory	NaOH 1M	20 min.

[1] The resist was overexposed to compensate for the changes in height due to the high surface topography

Bibliography

[1] A. Manz, N. Graber, and H.M. Widmer. Miniaturized total chemical analysis systems: A novel concept for chemical sensing. *Sensors and Actuators B: Chemical*, 1(1-6):244–248, jan 1990.

[2] David C. Duffy, J. Cooper McDonald, Olivier J. A. Schueller, and George M. Whitesides. Rapid Prototyping of Microfluidic Systems in Poly(dimethylsiloxane). *Analytical Chemistry*, 70(23):4974–4984, dec 1998.

[3] Leonard A Herzenberg, David Parks, Bita Sahaf, Omar Perez, Mario Roederer, and Leonore A Herzenberg. The history and future of the fluorescence activated cell sorter and flow cytometry: a view from Stanford. *Clinical chemistry*, 48(10):1819–27, oct 2002.

[4] B Schmitz, A Radbruch, T Kümmel, C Wickenhauser, H Korb, M L Hansmann, J Thiele, and R Fischer. Magnetic activated cell sorting (MACS)–a new immunomagnetic method for megakaryocytic cell isolation: comparison of different separation techniques. *European journal of haematology*, 52(5):267–75, may 1994.

[5] Wallace H. Coulter. high speed automated blood cell counter and cell analyzer. In *The National Electronics Conference*, Chicago, 1956.

[6] O. A. Saleh and L. L. Sohn. Quantitative sensing of nanoscale colloids using a microchip Coulter counter. *Review of Scientific Instruments*, 72(12):4449, 2001.

[7] Tao Sun and Hywel Morgan. Single-cell microfluidic impedance cytometry: a review. *Microfluidics and Nanofluidics*, 8(4):423–443, apr 2010.

[8] Yoichi Katsumoto, Yoshihito Hayashi, Ikuya Oshige, Shinji Omori, Noriyuki Kishii, Akio Yasuda, and Koji Asami. Dielectric Cytometry with Three-Dimensional Cellular Modeling. *Biophysical Journal*, 95(6):3043–3047, 2008.

[9] G. Benazzi, D. Holmes, T. Sun, M.C. Mowlem, and H. Morgan. Discrimination and analysis of phytoplankton using a microfluidic cytometer. *IET Nanobiotechnology*, 1(6):94, 2007.

[10] G. Schade-Kampmann, A. Huwiler, M. Hebeisen, T. Hessler, and M. Di Berardino. On-chip non-invasive and label-free cell discrimination by impedance spectroscopy. *Cell Proliferation*, 41(5):830–840, oct 2008.

Bibliography

[11] Claudia Küttel, Elisabete Nascimento, Nicolas Demierre, Tiago Silva, Thomas Braschler, Philippe Renaud, and Abel G. Oliva. Label-free detection of Babesia bovis infected red blood cells using impedance spectroscopy on a microfabricated flow cytometer. 2007.

[12] Karen C. Cheung, Marco Di Berardino, Grit Schade-Kampmann, Monika Hebeisen, Arkadiusz Pierzchalski, Jozsef Bocsi, Anja Mittag, and Attila Tárnok. Microfluidic impedance-based flow cytometry. *Cytometry Part A*, 77A(7):648–666, may 2010.

[13] Elena Bianchi, Enrica Rollo, Samuel Kilchenmann, Francesco M Bellati, Enrico Accastelli, and Carlotta Guiducci. Detecting particles flowing through interdigitated 3D microelectrodes. *Conference proceedings : ... Annual International Conference of the IEEE Engineering in Medicine and Biology Society. IEEE Engineering in Medicine and Biology Society. Conference*, 2012:5002–5, jan 2012.

[14] S. Gawad, L. Schild, and Ph. Renaud. Micromachined impedance spectroscopy flow cytometer for cell analysis and particle sizing. *Lab on a Chip*, 1(1):76, 2001.

[15] Karen Cheung, Shady Gawad, and Philippe Renaud. Impedance spectroscopy flow cytometry: On-chip label-free cell differentiation. *Cytometry Part A*, 65A(2):124–132, jun 2005.

[16] Ling-Sheng Jang and Min-How Wang. Microfluidic device for cell capture and impedance measurement. *Biomedical Microdevices*, 9(5):737–743, aug 2007.

[17] Daniele Malleo, J. Tanner Nevill, Luke P. Lee, and Hywel Morgan. Continuous differential impedance spectroscopy of single cells. *Microfluid Nanofluid*, 9(2-3):191–198, aug 2010.

[18] Kung-Chieh Lan and Ling-Sheng Jang. Integration of single-cell trapping and impedance measurement utilizing microwell electrodes. *Biosensors and Bioelectronics*, 26(5):2025–2031, 2011.

[19] Arum Han and A. Bruno Frazier. Ion channel characterization using single cell impedance spectroscopy. *Lab on a Chip*, 6(11):1412, 2006.

[20] Y. Zhao, X.T. Zhao, D.Y. Chen, Y.N. Luo, M. Jiang, C. Wei, R. Long, W.T. Yue, J.B. Wang, and J. Chen. Tumor cell characterization and classification based on cellular specific membrane capacitance and cytoplasm conductivity. *Biosensors and Bioelectronics*, 57:245–253, 2014.

[21] Christian M. Kurz, Heiko Büth, Adam Sossalla, Vincent Vermeersch, Veska Toncheva, Peter Dubruel, Etienne Schacht, and Hagen Thielecke. Chip-based impedance measurement on single cells for monitoring sub-toxic effects on cell membranes. *Biosensors and Bioelectronics*, 26(8):3405–3412, 2011.

[22] Younghak Cho, Hyun Soo Kim, A.B. Frazier, Z.G. Chen, Dong Moon Shin, and A. Han. Whole-Cell Impedance Analysis for Highly and Poorly Metastatic Cancer Cells. *Journal of Microelectromechanical Systems*, 18(4):808–817, aug 2009.

[23] Song-Bin Huang, Yang Zhao, Deyong Chen, Hsin-Chieh Lee, Yana Luo, Tzu-Keng Chiu, Junbo Wang, Jian Chen, and Min-Hsien Wu. A clogging-free microfluidic platform with an incorporated pneumatically driven membrane-based active valve enabling specific membrane capacitance and cytoplasm conductivity characterization of single cells. *Sensors and Actuators B: Chemical*, 190:928–936, 2014.

[24] Pratikkumar Shah, Xuena Zhu, Chunying Chen, Ye Hu, and Chen-Zhong Li. Lab-on-chip device for single cell trapping and analysis. *Biomedical Microdevices*, 16(1):35–41, feb 2014.

[25] Sungbo Cho and Hagen Thielecke. Micro hole-based cell chip with impedance spectroscopy. *Biosensors and Bioelectronics*, 22(8):1764–1768, 2007.

[26] Barbara Sorce, Carlos Escobedo, Yusuke Toyoda, Martin P. Stewart, Cedric J. Cattin, Richard Newton, Indranil Banerjee, Alexander Stettler, Botond Roska, Suzanne Eaton, Anthony A. Hyman, Andreas Hierlemann, and Daniel J. Müller. Mitotic cells contract actomyosin cortex and generate pressure to round against or escape epithelial confinement. *Nature Communications*, 6:8872, nov 2015.

[27] Muhammad Mansor and Mohd Ahmad. Single Cell Electrical Characterization Techniques. *International Journal of Molecular Sciences*, 16(6):12686–12712, jun 2015.

[28] Mandy LY Sin, Kathleen E Mach, Pak Kin Wong, and Joseph C Liao. Advances and challenges in biosensor-based diagnosis of infectious diseases. *Expert Review of Molecular Diagnostics*, 14(2):225–244, mar 2014.

[29] O. P. Hamill, A. Marty, E. Neher, B. Sakmann, and F. J. Sigworth. Improved patch-clamp techniques for high-resolution current recording from cells and cell-free membrane patches. *Pflügers Archiv - European Journal of Physiology*, 391(2):85–100, aug 1981.

[30] David Ogden and Peter Stanfield. Patch clamp techniques for single channel and whole-cell recording. In *Microelectrode Techniques*, pages 53–78. 1994.

[31] M. Karmažínová and L. Lacinová. Measurement of cellular excitability by whole cell patch clamp technique, 2010.

[32] Alain Marty and Erwin Neher. *Tight-Seal Whole-Cell Recording*, pages 31–52. Springer US, Boston, MA, 1995.

[33] Louis J. DeFelice. *Electrical Properties of Cells*. Springer US, Boston, MA, 1997.

[34] Wee-Liat Ong, Kum-Cheong Tang, Ajay Agarwal, Ranganathan Nagarajan, Lian-Wee Luo, and Levent Yobas. Microfluidic integration of substantially round glass capillaries for lateral patch clamping on chip. *Lab on a Chip*, 7(10):1357, 2007.

[35] Kum Cheong Tang, Julien Reboud, Yuan Li Kwok, Shu Ling Peng, and Levent Yobas. Lateral patch-clamping in a standard 1536-well microplate format. *Lab on a Chip*, 10(8):1044, 2010.

[36] Gaurav Jain, Nandkishore Muley, P Soni, Jitendra N Singh, and Shyam S Sharma. Patch clamp Technique: Conventional to Automated. *Current Research & Information on Pharmaceuticals Sciences (CRIPS)*, 10(1):9–15, 2009.

[37] Niels J. Willumsen, Morten Bech, Søren-Peter Olesen, Bo Skaaning Jensen, Mads P. G. Korsgaard, and Palle Christophersen. High Throughput Electrophysiology: New Perspectives for Ion Channel Drug Discovery. *Receptors and Channels*, 9(1):3–12, jan 2003.

[38] Margit Asmild, Nicholas Oswald, Karen M. Krzywkowski, Søren Friis, Rasmus B. Jacobsen, Dirk Reuter, Rafael Taboryski, Jonathan Kutchinsky, Ras K. Vestergaard, Rikke L. Schrøder, Claus B. Sørensen, Morten Bech, Mads P G Korsgaard, and Niels J. Willumsen. Upscaling and automation of electrophysiology: Toward high throughput screening in ion channel drug discovery, 2003.

[39] Christian Schmidt, Michael Mayer, and Horst Vogel. A Chip-Based Biosensor for the Functional Analysis of Single Ion Channels. *Angewandte Chemie*, 39(17):3137–3140, sep 2000.

[40] T. Lehnert, M. A. M. Gijs, R. Netzer, and U. Bischoff. Realization of hollow SiO[sub 2] micronozzles for electrical measurements on living cells. *Applied Physics Letters*, 81(26):5063, 2002.

[41] Niels Fertig, Robert H. Blick, and Jan C. Behrends. Whole Cell Patch Clamp Recording Performed on a Planar Glass Chip. *Biophysical Journal*, 82(6):3056–3062, 2002.

[42] Niels Fertig, Michele Klau, Michael George, Robert H. Blick, and Jan C. Behrends. Activity of single ion channel proteins detected with a planar microstructure. *Applied Physics Letters*, 81(25):4865, 2002.

[43] Chang-Yu Chen, Kuan-Ting Liu, De-Shien Jong, and Andrew M. Wo. Hourglass-shaped aperture for cellular electrophysiological study. *Applied Physics Letters*, 91(12):123901, 2007.

[44] J. Seo, C. Ionescu-Zanetti, J. Diamond, R. Lal, and L. P. Lee. Integrated multiple patch-clamp array chip via lateral cell trapping junctions. *Applied Physics Letters*, 84(11):1973, 2004.

[45] Chihchen Chen and Albert Folch. A high-performance elastomeric patch clamp chip. *Lab on a Chip*, 6(10):1338, 2006.

[46] Patthara Kongsuphol, Tushar Bansal, Kum Cheong Tang, and Kok Boon Fang. Electrophysiological characterization of ion channels in beta-cells using silicon based lateral patch clamp device. *Sensors and Actuators B: Chemical*, 173:462–467, 2012.

[47] A. Brüggemann, M. George, M. Klau, M. Beckler, J. Steindl, J.C. Behrends, and N. Fertig. High Quality Ion Channel Analysis on a Chip with the NPC © Technology. *ASSAY and Drug Development Technologies*, 1(5):665–673, oct 2003.

[48] A Stett, C Burkhardt, U Weber, P van Stiphout, and T Knott. CYTOCENTERING: A novel technique enabling automated cell-by-cell patch clamping with the CYTOPATCH™ chip. *Receptors and Channels*, 9(1):59–66, 2003.

[49] O Scheel, H Himmel, G Rascher-Eggstein, and T Knott. Introduction of a modular automated voltage-clamp platform and its correlation with manual human ether-à-go-go related gene voltage-clamp data. *Assay and Drug Development Technologies*, 9(6):600–607, 2011.

[50] L Kiss, P B Bennett, V N Uebele, K S Koblan, S A Kane, B Neagle, and K Schroeder. High throughput ion-channel pharmacology: planar-array-based voltage clamp. *Assay Drug Dev Technol*, 1(1 Pt 2):127–135, 2003.

[51] Kirk Schroeder, Brad Neagle, Derek J Trezise, and Jennings Worley. Ionworks HT: a new high-throughput electrophysiology measurement platform. *Journal of biomolecular screening*, 8(1):50–64, feb 2003.

[52] Alan Finkel, Andrew Wittel, Naibo Yang, Shawn Handran, Jan Hughes, and James Costantin. Population patch clamp improves data consistency and success rates in the measurement of ionic currents. *Journal of biomolecular screening*, 11(5):488–96, aug 2006.

[53] Steve Sorota, Xue-Song Zhang, Michael Margulis, Kristal Tucker, and Tony Priestley. Characterization of a hERG Screen Using the IonWorks HT: Comparison to a hERG Rubidium Efflux Screen. *ASSAY and Drug Development Technologies*, 3(1):47–57, feb 2005.

[54] Huimin Tao, David Santa Ana, António Guia, Mingxian Huang, Joseph Ligutti, George Walker, Khachonesine Sithiphong, Florence Chan, Tao Guoliang, Zoya Zozulya, Steve Saya, Rick Phimmachack, Charles Sie, Julian Yuan, Lei Wu, Jia Xu, and Andrea Ghetti. Automated Tight Seal Electrophysiology for Assessing the Potential hERG Liability of Pharmaceutical Compounds. *ASSAY and Drug Development Technologies*, 2(5):497–506, oct 2004.

[55] Adrienne E Dubin, Nadia Nasser, Jutta Rohrbacher, An N Hermans, Roger Marrannes, Christopher Grantham, Koen Van Rossem, Miroslav Cik, Sandra R Chaplan, David Gallacher, Jia Xu, Antonio Guia, Nicholas G Byrne, and Chris Mathes. Identifying modulators of hERG channel activity using the PatchXpress planar patch clamp. *Journal of biomolecular screening*, 10(2):168–81, mar 2005.

[56] Andrew P. Golden, Nianzhen Li, Qin Chen, Tony Lee, Tanner Nevill, Xueying Cao, Juliette Johnson, Gül Erdemli, Cristian Ionescu-Zanetti, Laszlo Urban, and Mats Holmqvist. IonFlux: A Microfluidic Patch Clamp System Evaluated with Human Ether-à-go-go Related Gene Channel Physiology and Pharmacology. *ASSAY and Drug Development Technologies*, 9(6):608–619, dec 2011.

Bibliography

[57] Levent Yobas. Microsystems for cell-based electrophysiology. *Journal of Micromechanics and Microengineering*, 23(8):083002, aug 2013.

[58] Liqun Wu, Lin-Yue Lanry Yung, and Kian-Meng Lim. Dielectrophoretic capture voltage spectrum for measurement of dielectric properties and separation of cancer cells. *Biomicrofluidics*, 6(1):014113, 2012.

[59] Daynene M. Vykoukal, Peter R. C. Gascoyne, and Jody Vykoukal. Dielectric characterization of complete mononuclear and polymorphonuclear blood cell subpopulations for label-free discrimination. *Integrative Biology*, 1(7):477, 2009.

[60] Lionel M Broche, Fatima H Labeed, and Michael P Hughes. Extraction of dielectric properties of multiple populations from dielectrophoretic collection spectrum data. *Physics in Medicine and Biology*, 50(10):2267–2274, may 2005.

[61] U Lei, Pei-Hou Sun, and Ronald Pethig. Refinement of the theory for extracting cell dielectric properties from dielectrophoresis and electrorotation experiments. *Biomicrofluidics*, 5(4):44109–4410916, dec 2011.

[62] P R C Gascoyne, F F Becker, and X B Wang. Numerical-Analysis of the Influence of Experimental Conditions on the Accuracy of Dielectric Parameters Derived from Electrorotation Measurements. *Bioelectrochemistry and Bioenergetics*, 36(2):115–125, 1995.

[63] D Voyer, M Frenea-Robin, F Buret, and L Nicolas. Improvements in the extraction of cell electric properties from their electrorotation spectrum. *Bioelectrochemistry*, 79(1):25–30, 2010.

[64] Yi Zheng, John Nguyen, Yuan Wei, and Yu Sun. Recent advances in microfluidic techniques for single-cell biophysical characterization. *Lab on a Chip*, 13(13):2464, 2013.

[65] G De Gasperis, XiaoBo B Wang, Jun Yang, Frederick F Becker, and Peter R C Gascoyne. Automated electrorotation: dielectric characterization of living cells by real-time motion estimation. *Measurement Science & Technology*, 9(3):518–529, mar 1998.

[66] Massimo Cristofanilli, Giovanni De Gasperis, Lisha Zhang, Mien-Chie Hung, Peter R. C. Gascoyne, and Gabriel N. Hortobagyi. Automated Electrorotation to Reveal Dielectric Variations Related to HER-2/neu Overexpression in MCF-7 Sublines. *American Association for Cancer Research*, 8(2), 2002.

[67] C. Dalton, A.D. D Goater, J. Drysdale, and R. Pethig. Parasite viability by electrorotation. *Colloids and Surfaces a-Physicochemical and Engineering Aspects*, 195(1-3):263–268, 2001.

[68] M. Lortet. Influence de courants induits sur l'orientation des bactéries vivantes. *Comptes Rendus de L'Académie des Sciences*, 122:892–894, 1896.

[69] A. D. Goater and R. Pethig. Electrorotation and dielectrophoresis. *Parasitology*, 117(7):177–189, 1999.

[70] U Lei and Y J Lo. Review of the theory of generalised dielectrophoresis. *Iet Nanobiotechnology*, 5(3):86–106, 2011.

[71] R Pethig. Application of A.C. electrical fields to the manipulation and characterisation of cells, 1991.

[72] W M Arnold and U Zimmermann. Rotating-Field-Induced Rotation and Measurement of the Membrane Capacitance of Single Mesophyll Cells of A vena sativa. *Zeitschrift für Naturforschung C*, 37(10):908–915, 1982.

[73] Maja Mischel, Arthur Voss, and Herbert A. Pohl. Cellular spin resonance in rotating electric fields. *Journal of Biological Physics*, 10(4):223–226, dec 1982.

[74] Ka Lok Chan, Peter R.C Gascoyne, Frederick F Becker, and Ronald Pethig. Electrorotation of liposomes: verification of dielectric multi-shell model for cells. *Biochimica et Biophysica Acta (BBA) - Lipids and Lipid Metabolism*, 1349(2):182–196, 1997.

[75] Senichi Masuda, Masao Washizu, and Masahiro Iwadare. Separation of Small Particles Suspended in Liquid by Nonuniform Traveling Field. *IEEE Transactions on Industry Applications*, IA-23(3):474–480, may 1987.

[76] T.B. Jones and Masao Washizu. Multipolar dielectrophoretic and electrorotation theory. *Journal of Electrostatics*, 37(1):121–134, 1996.

[77] Peter R. C. Gascoyne and Jody Vykoukal. Particle separation by dielectrophoresis. *Electrophoresis*, 23(13):1973, jul 2002.

[78] Ronald Pethig. Dielectrophoresis: An assessment of its potential to aid the research and practice of drug discovery and delivery. *Advanced Drug Delivery Reviews*, 65(11):1589–1599, 2013.

[79] A D Goater, J P H Burt, and R Pethig. A combined travelling wave dielectrophoresis and electrorotation device: applied to the concentration and viability determination of Cryptosporidium. *Journal of Physics D-Applied Physics*, 30(18):L65–L69, 1997.

[80] Richard V. E. Lovelace, Darryl G. Stout, and Peter L. Steponkus. Protoplast rotation in a rotating electric field: The influence of cold acclimation. *The Journal of Membrane Biology*, 82(2):157–166, jun 1984.

[81] Gunter Fuhr, Roland Glaser, and Rolf Hagedorn. ROTATION OF DIELECTRICS IN A ROTATING ELECTRIC HIGH-FREQUENCY FIELD Model Experiments and Theoretical Explanation of the Rotation Effect of Living Cells. 49(February):395–402, 1986.

[82] A. Chiabrera, M. Grattarola, and R. Viviani. Interaction between electromagnetic fields and cells: Microelectrophoretic effect on ligands and surface receptors. *Bioelectromagnetics*, 5(2):173–191, 1984.

Bibliography

[83] X J Wang, F F Becker, and P R C Gascoyne. The fractal dimension of cell membrane correlates with its capacitance: A new fractal single-shell model. *Chaos*, 20(4), 2010.

[84] Tadaaki Kakutani, Shibatani Shigeo, and Sugai Makoto. Electrorotation of non-spherical cells : theory for ellipsoidal cells with an arbitrary number of shells. 31:131–145, 1993.

[85] W. M. Arnold. Dielectrophoretic Cell Separation: Some Hints and Kinks. *Proc. ESA Annual Meeting on Electrostatics 2010*, 2010.

[86] Ulrich Zimmermann and Neil A. Garry. *Electromanipulation of Cells*. CRC Press, 1996.

[87] W.M. Arnold. Positioning and levitation media for the separation of biological cells. *Conference Record of the 1999 IEEE Industry Applications Conference. Thirty-Forth IAS Annual Meeting (Cat. No.99CH36370)*, 4:2470–2477, 1999.

[88] Norman E. Good, G. Douglas Winget, Wilhelmina Winter, Thomas N. Connolly, Seikichi Izawa, and Raizada M. M. Singh. Hydrogen Ion Buffers for Biological Research *. *Biochemistry*, 5(2):467–477, feb 1966.

[89] Jay M. Baltz. Media Composition: Salts and Osmolality. In *Embryo Culture*, pages 61–80. Humana Press, Totowa, NJ, 2012.

[90] U Zimmermann. Electrical breakdown, electropermeabilization and electrofusion. *Reviews of Physiology Biochemistry and Pharmacology*, 105:176–256, 1986.

[91] Michael Kirschbaum, Christian R. Guernth-Marschner, Solène Cherré, Albora de Pablo Peña, Magnus S. Jaeger, Richard a. Kroczek, Thomas Schnelle, Torsten Mueller, and Claus Duschl. Highly controlled electrofusion of individually selected cells in dielectrophoretic field cages. *Lab on a Chip*, 12(3):443, 2012.

[92] F F Becker, X B Wang, Y Huang, R Pethig, J Vykoukal, and P R C Gascoyne. The removal of human leukaemia cells from blood using interdigitated microelectrodes. *Journal of Physics D: Applied Physics*, 27(12):2659–2662, dec 1994.

[93] Gerard H. Markx, Mark S. Talary, and Ronald Pethig. Separation of viable and non-viable yeast using dielectrophoresis. *Journal of Biotechnology*, 32(1):29–37, 1994.

[94] M Stephens, M S Talary, R Pethig, A K Burnett, and K I Mills. The dielectrophoresis enrichment of CD34+ cells from peripheral blood stem cell harvests. *Bone Marrow Transplantation*, 18(4):777–782, 1996.

[95] S Archer, H Morgan, and F J Rixon. Electrorotation studies of baby hamster kidney fibroblasts infected with herpes simplex virus type 1. *Biophysical Journal*, 76(5):2833–2842, 1999.

[96] Jente Lu, Chesca A. Barrios, Amanda R. Dickson, Jamison L. Nourse, Abraham P. Lee, and Lisa A. Flanagan. Advancing practical usage of microtechnology: a study of the functional consequences of dielectrophoresis on neural stem cells. *Integrative Biology*, 4(10):1223, 2012.

[97] Lisa A. Flanagan, Jente Lu, Lisen Wang, Steve A. Marchenko, Noo Li Jeon, Abraham P. Lee, and Edwin S. Monuki. Unique Dielectric Properties Distinguish Stem Cells and Their Differentiated Progeny. *Stem Cells*, 26(3):656–665, mar 2008.

[98] Fatima H. Labeed, Jente Lu, Hayley J. Mulhall, Steve A. Marchenko, Kai F. Hoettges, Laura C. Estrada, Abraham P. Lee, Michael P. Hughes, and Lisa A. Flanagan. Biophysical Characteristics Reveal Neural Stem Cell Differentiation Potential. *PLoS ONE*, 6(9):e25458, sep 2011.

[99] Melinda G Simon, Ying Li, Janahan Arulmoli, Lisa P McDonnell, Adnan Akil, Jamison L Nourse, Abraham P Lee, and Lisa A Flanagan. Increasing label-free stem cell sorting capacity to reach transplantation-scale throughput. *Biomicrofluidics*, 8(6):064106, nov 2014.

[100] Joel Voldman. Dielectrophoretic Traps for Cell Manipulation. In *BioMEMS and Biomedical Nanotechnology*, pages 159–186. Springer US, Boston, MA, 2006.

[101] Günter Fuhr, Henning Glasser, Torsten Müller, and Thomas Schnelle. Cell manipulation and cultivation under a.c. electric field influence in highly conductive culture media. *Biochimica et Biophysica Acta (BBA) - General Subjects*, 1201(3):353–360, 1994.

[102] Aristides Docoslis, Nicolas Kalogerakis, and Leo A. Behie. Dielectrophoretic forces can be safely used to retain viable cells in perfusion cultures of animal cells. *Cytotechnology*, 30(1/3):133–142, 1999.

[103] H. Glasser and G. Fuhr. Cultivation of cells under strong ac-electric field—differentiation between heating and trans-membrane potential effects. *Bioelectrochemistry and Bioenergetics*, 47(2):301–310, 1998.

[104] Xujing Wang, Jun Yang, and Peter R.C. Gascoyne. Role of peroxide in AC electrical field exposure effects on Friend murine erythroleukemia cells during dielectrophoretic manipulations. *Biochimica et Biophysica Acta (BBA) - General Subjects*, 1426(1):53–68, 1999.

[105] L. Altomare, M. Borgatti, G. Medoro, N. Manaresi, M. Tartagni, R. Guerrieri, and R. Gambari. Levitation and movement of human tumor cells using a printed circuit board device based on software-controlled dielectrophoresis. *Biotechnology and Bioengineering*, 82(4):474–479, may 2003.

[106] Ralph Holzel. Simple Wide-Band Sine Wave Quadrature Oscillator. *IEEE Transactions on Instrumentation and Measurement*, 42(3):1992–1994, 1993.

[107] R Holzel. Electric field calculation for electrorotation electrodes. *Journal of Physics D: Applied Physics*, 26(12):2112–2116, dec 1993.

[108] K Maswiwat, M Holtappels, and J Gimsa. On the field distribution in electrorotation chambers - Influence of electrode shape. *Electrochimica Acta*, 51(24):5215–5220, 2006.

Bibliography

[109] Kanokkan Maswiwat, Moritz Holtappels, and Jan Gimsa. Optimizing the Electrode Shape for Four-electrode Electrorotation Chips. *ScienceAsia*, 33:61–67, 2007.

[110] Michael Pycraft Hughes. Computer-aided analysis of conditions for optimizing practical electrorotation. *Physics in Medicine and Biology*, 43(12):3639–3648, dec 1998.

[111] C Dalton, A D Goater, and H V Smith. Fertilization state of Ascaris suum determined by electrorotation. *Journal of Helminthology*, 80(1):25–31, 2006.

[112] G Fuhr, W M Arnold, R Hagedorn, T Muller, W Benecke, B Wagner, and U Zimmermann. Levitation, Holding, and Rotation of Cells within Traps Made by High-Frequency Fields. *Biochimica Et Biophysica Acta*, 1108(2):215–223, 1992.

[113] Thomas Schnelle, Rolf Hagedorn, Günter Fuhr, Stefan Fiedler, and Torsten Müller. Three-dimensional electric field traps for manipulation of cells — calculation and experimental verification. *Biochimica et Biophysica Acta (BBA) - General Subjects*, 1157(3):127–140, 1993.

[114] C Reichle, T Muller, T Schnelle, and G Fuhr. Electro-rotation in octopole micro cages. *Journal of Physics D-Applied Physics*, 32(16):2128–2135, 1999.

[115] T Schnelle, T Muller, C Reichle, and G Fuhr. Combined dielectrophoretic field cages and laser tweezers for electrorotation. *Applied Physics B-Lasers and Optics*, 70(2):267–274, 2000.

[116] R Georgiewa, E Donath, J Gimsa, U Lowe, and R Glaser. Ac-Field-Induced Kcl Leakage from Human Red-Cells at Low Ionic Strengths - Implications for Electrorotation Measurements. *Bioelectrochemistry and Bioenergetics*, 22(3):255–270, 1989.

[117] G. Bahrieh, H. Ceylan Koydemir, M. Erdem, E. Ozgur, U. Gunduz, and H. Kulah. Dielectric characterization of Imatinib resistant K562 leukemia cells through electrorotation with 3-D electrodes. *2013 IEEE SENSORS*, pages 1–4, nov 2013.

[118] Nicolas Demierre, Thomas Braschler, Pontus Linderholm, Urban Seger, Harald van Lintel, and Philippe Renaud. Characterization and optimization of liquid electrodes for lateral dielectrophoresis. *Lab Chip*, 7(3):355–365, 2007.

[119] J Gimsa, P Marszalek, U Loewe, and T Y Tsong. Dielectrophoresis and Electrorotation of Neurospora Slime and Murine Myeloma Cells. *Biophysical Journal*, 60(4):749–760, 1991.

[120] M Egger, E Donath, P I Kuzmin, and V P Pastushenko. Electrorotation of Dumbbell Shaped Particles - Theory and Experiment. *Bioelectrochemistry and Bioenergetics*, 26(3):383–393, 1991.

[121] S Shibatani, K Minami, M Senda, and T Kakutani. Electrorotation of Vacuoles Isolated from Barley Mesophyll-Cells. *Bioelectrochemistry and Bioenergetics*, 29(3):327–335, 1993.

[122] X F Zhou, G H Markx, R Pethig, and I M Eastwood. Differentiation of Viable and Nonviable Bacterial Biofilms Using Electrorotation. *Biochimica Et Biophysica Acta-General Subjects*, 1245(1):85–93, 1995.

[123] Y Huang, X B Wang, F F Becker, and P R C Gascoyne. Membrane changes associated with the temperature-sensitive P85(gag-mos)-dependent transformation of rat kidney cells as determined by dielectrophoresis and electrorotation. *Biochimica Et Biophysica Acta-Biomembranes*, 1282(1):76–84, 1996.

[124] R Holzel. Electrorotation of single yeast cells at frequencies between 100 Hz and 1.6 GHz. *Biophysical Journal*, 73(2):1103–1109, 1997.

[125] B Neu, R Georgieva, H Baumler, V N Shilov, E Knippel, and E Donath. Low-frequency dispersion of surface conducting particles as measured by means of electrorotation. *Colloids and Surfaces a-Physicochemical and Engineering Aspects*, 140(1-3):325–332, 1998.

[126] G R Fuhr and C Reichle. Living cells in opto-electrical cages characterisation manipulation and force measurements. *Micro Total Analysis Systems 2000, Proceedings*, pages 261–264, 2000.

[127] R Georgieva, S Moya, S Leporatti, B Neu, H Baumler, C Reichle, E Donath, and H Mohwald. Conductance and capacitance of polyelectrolyte and lipid-polyelectrolyte composite capsules as measured by electrorotation. *Langmuir*, 16(17):7075–7081, 2000.

[128] Michael Kriegmaier, Martin Zimmermann, Klaus Wolf, Ulrich Zimmermann, and Vladimir L Sukhorukov. Dielectric spectroscopy of Schizosaccharomyces pombe using electrorotation and electroorientation. *Biochimica et Biophysica Acta (BBA) - General Subjects*, 1568(2):135–146, 2001.

[129] G Abou-Ali, K V I S Kaler, R Paul, N K Bjorklund, and R Gordon. Electrorotation of axolotl embryos. *Bioelectromagnetics*, 23(3):214–223, 2002.

[130] O R Reuss, M Kurschner, S Dilsky, M Horbaschek, W A Schenk, U Zimmermann, and V L Sukhorukov. Interaction of fluorinated lipophilic ions with the plasma membrane of mammalian cells studied by electrorotation and dielectrophoresis. *Journal of Electrostatics*, 56(4):419–434, 2002.

[131] C Dalton, A D Goater, R Pethig, and H V Smith. Viability of Giardia intestinalis cysts and viability and sporulation state of Cyclospora cayetanensis oocysts determined by electrorotation. *Applied and Environmental Microbiology*, 67(2):586–590, 2001.

[132] C Huang, Y Wu, L Wang, and J Yu. Negative dielectrophoretic force assisted determination differences between autotrophic and heterotrophic algal cells using electrorotation chip. *2006 1st IEEE International Conference on Nano/Micro Engineered and Molecular Systems, Vols 1-3*, pages 310–315, 2006.

Bibliography

[133] K Ino, A Ishida, K Y Inoue, M Suzuki, M Koide, T Yasukawa, H Shikua, and T Matsue. Electrorotation chip consisting of three-dimensional interdigitated array electrodes. *Sensors and Actuators B-Chemical*, 153(2):468–473, 2011.

[134] Ali Rohani, Walter Varhue, Yi-Hsuan Su, and Nathan S Swami. Electrical tweezer for highly parallelized electrorotation measurements over a wide frequency bandwidth. *Electrophoresis*, 35(12-13):1795–802, jul 2014.

[135] C Reichle, T Schnelle, T Muller, T Leya, and G Fuhr. A new microsystem for automated electrorotation measurements using laser tweezers. *Biochimica Et Biophysica Acta-Bioenergetics*, 1459(1):218–229, 2000.

[136] D Zimmermann, A Zhou, M Kiesel, K Feldbauer, U Terpitz, W Haase, T Schneider-Hohendorf, E Bamberg, and V L Sukhorukov. Effects on capacitance by overexpression of membrane proteins. *Biochemical and Biophysical Research Communications*, 369(4):1022–1026, 2008.

[137] Christoph Reichle, Katrin Sparbier, Torsten Müller, Thomas Schnelle, Peter Walden, and Günter Fuhr. Combined laser tweezers and dielectric field cage for the analysis of receptor-ligand interactions on single cells. *ELECTROPHORESIS*, 22(2):272–282, jan 2001.

[138] Song-I Han, Young-Don Joo, and Ki-Ho Han. An electrorotation technique for measuring the dielectric properties of cells with simultaneous use of negative quadrupolar dielectrophoresis and electrorotation. *The Analyst*, 138(5):1529–37, mar 2013.

[139] A. Budde, G. Grümmer, and E. Knippel. Electrorotation of Cells and Particles: An Automated Instrumentation. *Instrumentation Science & Technology*, 27(1):59–66, jan 1999.

[140] Yang Qihua, Li Hao, Liu Ganghai, and Liu Yanling. Cell Electrorotation Motion Parameters Detection Based on Image Processing. In *2009 WRI World Congress on Computer Science and Information Engineering*, volume 6, pages 549–553. IEEE, mar 2009.

[141] M Schaeper, R Schmidt, R Kostbade, N Damaschke, and J Gimsa. Optical high-resolution analysis of rotational movement: testing circular spatial filter velocimetry (CSFV) with rotating biological cells. *Journal of Physics D: Applied Physics*, 49(26):265402, jul 2016.

[142] M P Hughes, X B Wang, F F Becker, P R C Gascoyne, and R Pethig. Computer-aided analyses of electric fields used in electrorotation studies. *Journal of Physics D: Applied Physics*, 27(7):1564–1570, jul 1994.

[143] Herbert A. (Herbert Ackland) Pohl. *Dielectrophoresis : the behavior of neutral matter in nonuniform electric fields*. Cambridge University Press, Cambridge, New York, Melbourne, 1978.

[144] J. Voldman, M. Toner, M.L. Gray, and M.A. Schmidt. Design and analysis of extruded quadrupolar dielectrophoretic traps. *Journal of Electrostatics*, 57(1):69–90, 2003.

[145] Thomas B. Jones. *Electromechanics of Particles*. Cambridge University Press, 1995.

[146] Gerard H Markx, Ronald Pethig, and Juliette Rousselet. The dielectrophoretic levitation of latex beads, with reference to field-flow fractionation. *Journal of Physics D: Applied Physics*, 30(17):2470–2477, sep 1997.

[147] Lisen Wang, Lisa A Flanagan, Edwin Monuki, Noo Li Jeon, and Abraham P Lee. Dielectrophoresis switching with vertical sidewall electrodes for microfluidic flow cytometry. *Lab on a chip*, 7(9):1114–20, sep 2007.

[148] Jian Xu, Dong Wu, Yasutaka Hanada, Chi Chen, Sizhu Wu, Ya Cheng, Koji Sugioka, and Katsumi Midorikawa. Electrofluidics fabricated by space-selective metallization in glass microfluidic structures using femtosecond laser direct writing. *Lab on a chip*, 13(23):4608–16, dec 2013.

[149] Jian Xu, Dong Wu, Joanna Y. Ip, Katsumi Midorikawa, and Koji Sugioka. Vertical sidewall electrodes monolithically integrated into 3D glass microfluidic chips using water-assisted femtosecond-laser fabrication for in situ control of electrotaxis. *RSC Adv.*, 5(31):24072–24080, mar 2015.

[150] M. Becker, D. Lütke Notarp, J. Vogel, E. Kieselstein, J.-P. Sommer, K. Brämer, V. Großer, W. Benecke, and B. Michel. Application of electroplating in MEMS-micromachining exemplified by a microrelay. *Microsystem Technologies*, 7(4):196–202, nov 2001.

[151] C. Wang, G. Jia, L.H. Taherabadi, and M.J. Madou. A novel method for the fabrication of high-aspect ratio C-MEMS structures. *Journal of Microelectromechanical Systems*, 14(2):348–358, apr 2005.

[152] Olivier J. A. Schueller, Scott T. Brittain, and George M. Whitesides. Fabrication of glassy carbon microstructures by pyrolysis of microfabricated polymeric precursors. *Advanced Materials*, 9(6):477–480, jun 1997.

[153] Rodrigo Martinez-Duarte, Philippe Renaud, and Marc J Madou. A novel approach to dielectrophoresis using carbon electrodes. *Electrophoresis*, 32(17):2385–92, sep 2011.

[154] Benjamin Y. Park, Lili Taherabadi, Chunlei Wang, Jim Zoval, and Marc J. Madou. Electrical Properties and Shrinkage of Carbonized Photoresist Films and the Implications for Carbon Microelectromechanical Systems Devices in Conductive Media. *Journal of The Electrochemical Society*, 152(12):J136, 2005.

[155] Benjamin Mustin and Boris Stoeber. Low cost integration of 3D-electrode structures into microfluidic devices by replica molding. *Lab on a Chip*, 12(22):4702, 2012.

[156] X. Z. Niu, S. L. Peng, L. Y. Liu, W. J. Wen, and P. Sheng. Characterizing and Patterning of PDMS-Based Conducting Composites. *Advanced Materials*, 19(18):2682–2686, sep 2007.

Bibliography

[157] S. Jiguet, A. Bertsch, H. Hofmann, and P. Renaud. Conductive SU8-silver composite photopolymer. In *17th IEEE International Conference on Micro Electro Mechanical Systems. Maastricht MEMS 2004 Technical Digest*, pages 125–128. IEEE, 2004.

[158] Hailin Cong and Tingrui Pan. Photopatternable Conductive PDMS Materials for Micro-fabrication. *Advanced Functional Materials*, 18(13):1912–1921, jul 2008.

[159] Jae-Woo Choi, Samuel Rosset, Muhamed Niklaus, James R Adleman, Herbert Shea, and Demetri Psaltis. 3-dimensional electrode patterning within a microfluidic channel using metal ion implantation. *Lab on a chip*, 10(6):783–8, mar 2010.

[160] Rodrigo Martinez-Duarte. Microfabrication technologies in dielectrophoresis applications–a review. *Electrophoresis*, 33(21):3110–32, nov 2012.

[161] Samuel C. Kilchenmann, Enrica Rollo, Elena Bianchi, and Carlotta Guiducci. Metal-coated silicon micropillars for freestanding 3D-electrode arrays in microchannels. *Sensors and Actuators B: Chemical*, 185(null):713–719, aug 2013.

[162] Samuel C. Kilchenmann, Enrica Rollo, Pietro Maoddi, and Carlotta Guiducci. Metal-Coated SU-8 Structures for High-Density 3-D Microelectrode Arrays. *Journal of Micro-electromechanical Systems*, Accepted:1–7, 2016.

[163] H Jansen, M de Boer, R Legtenberg, and M Elwenspoek. The black silicon method: a universal method for determining the parameter setting of a fluorine-based reactive ion etcher in deep silicon trench etching with profile control. *Journal of Micromechanics and Microengineering*, 5(2):115–120, jun 1995.

[164] A Del Campo, C Greiner, A del Campo, and C Greiner. SU-8: a photoresist for high-aspect-ratio and 3D submicron lithography. *Journal of Micromechanics and Microengineering*, 17(6):R81–R95, jun 2007.

[165] John D Williams and Wanjun Wang. Study on the postbaking process and the effects on UV lithography of high aspect ratio SU-8 microstructures. *Journal of Micro/Nanolithography, MEMS and MOEMS*, 3(4):563–568, 2004.

[166] Mauro Ferrari. *BioMEMS and biomedical nanotechnology.* Springer, 2006.

[167] Richard L. Barber, Muralidhar K. Ghantasala, Ralu Divan, Derrick C. Mancini, and Erol C. Harvey. Study of stress and adhesion strength in SU-8 resist layers on silicon substrate with different seed layers. *Journal of Micro/Nanolithography, MEMS, and MOEMS*, 6(3):033006, jul 2007.

[168] Buddhadev Paul Chaudhri, Frederik Ceyssens, Piet De Moor, Chris Van Hoof, and Robert Puers. A high aspect ratio SU-8 fabrication technique for hollow microneedles for transdermal drug delivery and blood extraction. *Journal of Micromechanics and Microengineering*, 20:064006, 2010.

116

[169] Paul M. Dentinger, Karen L. Krafcik, Kelby L. Simison, Richard P. Janek, and John Hachman. High aspect ratio patterning with a proximity ultraviolet source. *Microelectronic Engineering*, 61-62:1001–1007, 2002.

[170] H. Lorenz, M. Despont, P. Vettiger, and P. Renaud. Fabrication of photoplastic high-aspect ratio microparts and micromolds using SU-8 UV resist. *Microsystem Technologies*, 4:143–146, 1998.

[171] J J Keane and R F Zopf. Dry film resists, 1984.

[172] Marc J. Madou. *Fundamentals of microfabrication and nanotechnology*. CRC Press, 2012.

[173] Pradeep Dixit and Jianmin Miao. Aspect-Ratio-Dependent Copper Electrodeposition Technique for Very High Aspect-Ratio Through-Hole Plating. *Journal of The Electrochemical Society*, 153(6):G552, 2006.

[174] Mansoureh Norouzi Rad and Nima Shokri. Nonlinear effects of salt concentrations on evaporation from porous media. *Geophysical Research Letters*, 39(4):n/a–n/a, feb 2012.

[175] Michael P Hughes, Steffen Archer, and Hywel Morgan. Mapping the electrorotational torque in planar microelectrodes. *Journal of Physics D: Applied Physics*, 32(13):1548–1552, jul 1999.

[176] Yufei Ren, Shun-Ho Huang, Sébastien Mosser, Marc Heuschkel, Arnaud Bertsch, Patrick Fraering, Jia-Jin Chen, and Philippe Renaud. A Simple and Reliable PDMS and SU-8 Irreversible Bonding Method and Its Application on a Microfluidic-MEA Device for Neuroscience Research. *Micromachines*, 6(12):1923–1934, dec 2015.

[177] S G Serra, A Schneider, K Malecki, S E Huq, and W Brenner. A simple bonding process of SU-8 to glass to seal a microfluidic device. 2007.

[178] C. Kourouklis, T. Kohlmeier, and H.H. Gatzen. The application of chemical–mechanical polishing for planarizing a SU-8/permalloy combination used in MEMS devices. *Sensors and Actuators A: Physical*, 106(1-3):263–266, sep 2003.

[179] Brian D. Iverson and Suresh V. Garimella. Recent advances in microscale pumping technologies: a review and evaluation. *Microfluidics and Nanofluidics*, 5(2):145–174, aug 2008.

[180] Chang Kyu Byun, Kameel Abi-Samra, Yoon-Kyoung Cho, and Shuichi Takayama. Pumps for microfluidic cell culture. *ELECTROPHORESIS*, 35(2-3):245–257, feb 2014.

[181] Daniel Mark, Stefan Haeberle, Günter Roth, Felix von Stetten, and Roland Zengerle. Microfluidic lab-on-a-chip platforms: requirements, characteristics and applications. *Chemical Society Reviews*, 39(3):1153, 2010.

Bibliography

[182] Axel Günther and Klavs F. Jensen. Multiphase microfluidics: from flow characteristics to chemical and materials synthesis. *Lab Chip*, 6(12):1487–1503, 2006.

[183] Dhananjay Dendukuri, Shelley S. Gu, Daniel C. Pregibon, T. Alan Hatton, and Patrick S. Doyle. Stop-flow lithography in a microfluidic device. *Lab on a Chip*, 7(7):818, 2007.

[184] M A Unger, H P Chou, T Thorsen, A Scherer, and S R Quake. Monolithic microfabricated valves and pumps by multilayer soft lithography. *Science (New York, N.Y.)*, 288(5463):113–6, apr 2000.

[185] Kwang W. Oh, Kangsun Lee, Byungwook Ahn, and Edward P. Furlani. Design of pressure-driven microfluidic networks using electric circuit analogy. *Lab Chip*, 12(3):515–545, 2012.

[186] Robert Gorkin, Jiwoon Park, Jonathan Siegrist, Mary Amasia, Beom Seok Lee, Jong-Myeon Park, Jintae Kim, Hanshin Kim, Marc Madou, and Yoon-Kyoung Cho. Centrifugal microfluidics for biomedical applications. *Lab on a Chip*, 10(14):1758, 2010.

[187] Chia-Fu Chou, Jonas O. Tegenfeldt, Olgica Bakajin, Shirley S. Chan, Edward C. Cox, Nicholas Darnton, Thomas Duke, and Robert H. Austin. Electrodeless Dielectrophoresis of Single- and Double-Stranded DNA. *Biophysical Journal*, 83(4):2170–2179, 2002.

[188] Blanca H. Lapizco-Encinas, Blake A. Simmons, Eric B. Cummings, and Yolanda Fintschenko. Dielectrophoretic Concentration and Separation of Live and Dead Bacteria in an Array of Insulators. *Analytical Chemistry*, 76(6):1571–1579, mar 2004.

[189] Martin Zimmermann, Heinz Schmid, Patrick Hunziker, and Emmanuel Delamarche. Capillary pumps for autonomous capillary systems. *Lab Chip*, 7(1):119–125, 2007.

[190] Wouter van der Wijngaart. Capillary pumps with constant flow rate. *Microfluidics and Nanofluidics*, 16(5):829–837, feb 2014.

[191] Arman Javadi, Mehdi Habibi, Fereshte Samadi Taheri, Sébastien Moulinet, and Daniel Bonn. Effect of wetting on capillary pumping in microchannels. *Scientific Reports*, 3:977–1026, mar 2013.

[192] Henrik Bruus. Chapter 1. Governing Equations in Microfluidics. In *Microscale Acoustofluidics*, pages 1–28. Royal Society of Chemistry, Cambridge, 2015.

[193] A. Lamberti, S. L. Marasso, and M. Cocuzza. PDMS membranes with tunable gas permeability for microfluidic applications. *RSC Adv.*, 4(106):61415–61419, nov 2014.

[194] D Wicher and J Gundel. Electrorotation of Multilamellar and Oligolamellar Liposomes. *Bioelectrochemistry and Bioenergetics*, 21(3):279–288, 1989.

[195] Joel Voldman, Martha L Gray, Mehmet Toner, and Martin A Schmidt. A Microfabrication-Based Dynamic Array Cytometer. *anal. Ch*, 74:2984–2990, 2002.

[196] Monsur Islam, Rucha Natu, Maria Fernanda Larraga-Martinez, and Rodrigo Martinez-Duarte. Enrichment of diluted cell populations from large sample volumes using 3D carbon-electrode dielectrophoresis. *Biomicrofluidics*, 10(3):033107, may 2016.

[197] Rodrigo Martinez-Duarte, Fernanda Camacho-Alanis, Philippe Renaud, and Alexandra Ros. Dielectrophoresis of lambda-DNA using 3D carbon electrodes. *ELECTROPHORESIS*, 34(7):1113–1122, apr 2013.

[198] Iness R. Benmessaoud, Anne-Laure Mahul-Mellier, Endre Horváth, Bohumil Maco, Massimo Spina, Hilal A. Lashuel, and Làszló Forró. Health hazards of methylammonium lead iodide based perovskites: cytotoxicity studies. *Toxicol. Res.*, 5(2):407–419, 2016.

[199] Cheng-Hsin Chuang, You-Ming Hsu, and Chen-Che Yeh. The effects of nanoparticles uptaken by cells on electrorotation. *ELECTROPHORESIS*, 30(9):1449–1456, may 2009.

[200] Xiao-Feng Zhou, Gerard H. Markx, and Ronald Pethig. Effect of biocide concentration on electrorotation spectra of yeast cells. *Biochimica et Biophysica Acta (BBA) - Biomembranes*, 1281(1):60–64, 1996.

[201] W. Pauli, S. Berger, M. Köhler, and A. Gies. Detecting membrane impairment caused by xenobiotics. *Environmental Toxicology & Water Quality*, 8(2):173–189, may 1993.

[202] W. Michael Arnold, Ulrich Zimmermann, Wilfried Pauli, Martin Benzing, Christoph Niehns, and Jan Ahlers. The comparative influence of substituted phenols (especially chlorophenols) on yast cells assayed by elecro-rotation and other methods. *Biochimica et Biophysica Acta (BBA) - Biomembranes*, 942(1):83–95, 1988.

[203] W. Michael Arnold, Ulrich Zimmermann, Wolfgang Heiden, and Jan Ahlers. The influence of tetraphenylborates (hydrophobic anions) on yeast cell electro-rotation. *Biochimica et Biophysica Acta (BBA) - Biomembranes*, 942(1):96–106, 1988.

Samuel Kilchenmann

Life is one big experiment - stay curious

About

I'm a young open minded scientist, looking for an academic position in biomedical engineering. I have a strong background in microfabrication and systems engineering for biomedical applications. I'm a curious and creative person that likes to tackle challenges and to work in an international team.

Contact

T: +41 (0)79 541 28 04

samuel.kilchenmann@gmail.com

www.linkedin.com/in/samkilch

www.github.com/SamKilch

www.researchgate.net/profile/Samuel_Kilchenmann

Av. de Beaulieu 39
Lausanne, Vaud, Switzerland

Experience

PhD in Biomedical engineering   2011–2016
Laboratory of Life Sciences Electronics, EPFL, Switzerland

During my PhD, I developed an electrorotation system based on 3D electrodes to trap and analyze single cells. My main contributions were in the development of a new microfabrication process for 3D electrodes and in the development of an automated system for fast and accurate extraction of the dielectric spectrum of a single cell.

Internship   2010–2011
Laboratory of Life Sciences Electronics, EPFL, Switzerland

The goal of this internship was to develop a MEMS based disposable interface to perform bioanalytics on a CMOS chip. My main contributions were in the trouble shooting of the cleanroom process and the development of an SPR assay to study protein-membrane interactions.

Master's Thesis   2010–2010
Biomems Research group, UC Irvine, USA

I did my master's thesis on 3D carbon electrodes for dielectrophoretic experiments on a centrifugal microfluidic platform. My main contribution was in the optimization of the fabrication process of the C-MEMS structures, to achieve high aspect ratio and high density of the carbon electrodes

Education

Master in Micro- and Nanosystems with additional   2008–2010
minor in biomedical engineering
EPFL, Switzerland

Bachelor in Microtechnique   2004-2008
EPFL, Switzerland

Key skills

Microfabrication   **Automation**   **Data analysis**

Teamwork   **Scientific writing** **Cell biology**

Languages

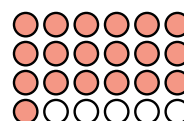**German (Native/C2)**
English (Fluent/C2)
French (Fluent/C2)
Italian (Beginner/A1)

121

Awards & Grants

NSF Travel grant
I received an NSF travel grant to attend the Dielectrophoresis conference held in 2016 at MIT, Boston.
Best rapid fire oral presentation
Annual meeting of the american electrophoreis society 2014, Atlanta, USA

Microfabrication skills

Photolithography (positive, negative and dry film resists)
Mask writting and fabrication, Thin films (sputtering, evaporation, CVD, ALD)
Wet etching (Piranha, HF, BHF, ANP, chrome etch)
Dry etching (Bosch, SiO_2, Metal, Ion Beam)
Charachterization (SEM, profilometry, electrical probing)

Biology skills

Surface Plasmon Resonance, Lipids and vesicles, Cell culturing, Fluorescence microscopy

Software skills

Labview, Solidworks, Comsol Multiphysics, Origin, R, Photoshop, Illustrator, InDesign, Latex, C/C++

Main Publications

Metal-Coated SU-8 structures for High-Density 3-D Microelectrode Arrays   2016
Journal of Microelectromechanical Systems

Metal-coated silicon micropillars for freestanding 3D-electrode arrays in microchannels   2013
Sensors and Actuators, B: Chemical

Main conference presentations

A fully automated 3-D electrode based electrorotation setup for fast and accurate spectrum acquisition   2016
MicroTAS 2016, Dublin, IRL

3D electrodes for simultaneous DEP trapping and particle rotation   2016
Dielectrophoresis 2016, MIT, USA

Individually addressable 3D microelectrodes for on-chip bioanalytics   2014
Micro and Nanoengineering 2014, EPFL, CHE

Volunteering

Summer school: Healthcare diagnostics in 2025   2016

I was involved in the organization of a summer school for PhD students, with the focus on future trends in healthcare diagnostics. My main contributions were in fund raising and the organization of international key opinion leaders as speakers.

The Brain Forum Start-up competition   2016
The Brain Forum Innovation corner   2015

I volunteered for the organization of a start-up event held during the BrainForum. The event was targeted at european start-ups in the field of neurosciences. My main contribution was in the organization of a jury and panel, consisting of Investors, business Angels, VCs and start-up coaches.

Hobbies

Youth and Sports - snowboard teaching
In winter I join school classes for winter camps to teach the kids how to snowboard

Sports
I balance my work life with different sports, including hockey, bouldering, bodyweight training and yoga.

Photography
I like to go around and explore the world through my lenses.